Application of Dynamic Mesh Method in CFD to Engineering Designs of Needle-Free Liquid Jet Injector and Diaphragm-less Shock Tube

Haruka Nakayama

A Thesis
in
The Department
of
Mechanical and Industrial Engineering

Presented in Partial Fulfillment of the Requirements
For the Degree of Master of Applied Science (Mechanical Engineering) at

Concordia University
Montreal, Quebec, Canada

August 2013

CONCORDIA UNIVERSITY
School of Graduate Studies

This is to certify that the thesis prepared

By: Haruka Nakayama

Entitled: Application of Dynamic Mesh Method in CFD to Engineering Designs of Needle-Free Liquid Jet Injector and Diaphragm-less Shock Tube

and submitted in partial fulfillment of the requirements for the degree of

Master of Applied Science (Mechanical Engineering)

complies with the regulations of the University and meets the accepted standards with respect to originality and quality.

Signed by the final examining committee:

I. Contreras Chair

A. Dolatabadi Examiner

N. Bouguila Examiner

H.D. Ng Supervisor

Approved by _____
Chair of Department or Graduate Program Director

_____
Dean of Faculty

Date August 26, 2013

Abstract

Application of Dynamic Mesh Method in CFD to Engineering Designs of Needle-Free Liquid Jet Injector and Diaphragm-less Shock Tube

Haruka Nakayama

Many engineering devices have dynamic components and hence, their computational models are no longer fixed in space and time. In these cases, dynamic mesh method is often applied to analyze their motion or unsteady fluid dynamics around/inside them. This study deals with the engineering application of CFD particularly using dynamic mesh methods to simulate firstly the compressible transient flow in a needle-less liquid jet injector for biomedical application and secondly, the performance of a diaphragm-less shock tube design for investigation of high-speed compressible gas dynamics. The CFD software OpenFOAM® is used as the main research tool to carry out this study.

For the first application, the dynamic behavior of the liquid jet is approximated using multi-phase compressible immiscible fluids LES solver together with the Volume-of-Fluid (VOF) method for the interface capturing. The liquid retained in the injector chamber is impacted by the moving grid boundary to mimic the injector piston driven by the driver air pressure; and the high speed liquid jet is emitted to atmosphere region though a nozzle. Numerical results are validated and discussed by comparing with experimental measurements. Performance plots as a function of various injector parameters are constructed and explained.

The second application concerns with the diaphragm-less shock tube design which consists of an outer tube contained with high pressure and an inner one with low pressure. A particular design of diaphragm-less shock tube utilizes a rapid opening sleeve to mimic the rupture of a diaphragm which is traditionally used to separate the two pressure region. Applying CFD with dynamic mesh to the sleeve motion contributes to the analysis of the process of shock wave generation in this device and the shock tube parameters such as opening time of the sleeve for reliable performance.

It is proven in this work that the numerical CFD models with dynamic mesh can accurately predict the performance of both engineering devices and provide a useful tool to analyze which parameters most significantly impact the performances.

Acknowledgements

I would like to express my gratitude to Dr. Hoi Dick Ng for the valuable comments, advice and suggestions through my study. I am extremely grateful for the constant encouragement and support from him.

I am also grateful to have a laboratory colleague, Rocco Portaro who has assisted me with my research by offering his experimental data to validate CFD results.

Furthermore, I would like to thank my wife, Yoko who has always been there with tenacious for me to provide sincere encouragement to my many challenges in Canada as well as for proofreading admission/immigration document I wrote. I would also like to thank my parents for believing in me and being supportive with warm heart.

Table of Contents

List of Figures

List of Tables

Nomenclature

Symbols

A_p	Piston surface area [m^2]
B	Bulk modulus of fluid in injection chamber [N/m^2]
C_v	Volumetric heat capacity [J/m^3-K]
c	Control volume
D	Inner diameter of O-ring seal [m]
F_D	Driver force by the gas pressure inside the driver part (1D)
F_f	Frictional force between the inner surface of the piston and O-rings [N]
F_{fluid}	Force of fluid exerted on O-ring [N]
F_{sv}	Surface tension [N]
f	Face
h	Height of clearance gap used for O-ring [m]
k	Sub-grid scale turbulent energy [J]
L_o	Initial length of the cylinder for needle-free injectors [m]
m	Mass of air [kg]
m_p	Mass of the piston for needle-free injectors [kg]
n	Time step (attached on the right shoulder of a symbol)
$\boldsymbol{n}$	Outward unit normal vector
p	Pressure [Pa]
p_a	Atmospheric pressure [Pa]
p_d	Driver pressure [Pa]
$p_{o\text{-}ring}$	Complete pressure distribution on O-ring [Pa]
P, Q	Computational point
R	Gas constant for air [J/kg-K]
$R_{x,y,z}$	Position vector or mesh vertex [m]
S	Surface or surface area [m^2]
S_ϕ	Volume source/sink of ϕ
T	Temperature [K]
t	Time [s]

$\mathbf{U}$ Fluid velocity [m/s]

$\mathbf{U_b}$ Boundary mesh (grid) velocity [m/s]

$\mathbf{U_m}$ Internal mesh (grid) velocity [m/s]

V Volume [m^3]

V_D Volume of the driver chamber for needle-free injectors [m^3]

x_p Piston position (1D) [m]

Greek Symbols

α A face (or surface) angle [deg]

α_1 Volume fraction of water

γ Specific heat ratio of air

δ Diffusion coefficient for mesh field

ε Turbulent dissipation

κ Compression force by O-rings [N]

κ Curvature of the liquid surface $\kappa = \nabla \cdot \hat{n}$

μ Dynamic viscosity [Pa · s]

ν Kinematic viscosity [m^2/s]

ρ Density [kg/m^3]

σ Surface tension [N/m^2]

τ Stress tensor [N]

ϕ Tensorial property

ψ Compresibility [s^2/m^2]

Ω Computational domain

Dimensionless Parameters

Pr Prandtl number

Re Reynolds number

Chapter 1

Introduction

1.1. General overview

Fluid dynamics is one of the primary engineering sciences used to design a wide variety of vehicles, machines, and other practical devices. In the past, fluid dynamic analysis was fairly simple, using either empirical formulas from engineering handbooks or other simplified mathematical analysis such as linearized or asymptotic theory. With the advance in scientific computing and the expoential growth of computer power in the past decades, the application of Computational Fluid Dynamics (CFD) is becoming more practicable and less expensive, making it a useful tool in engineering design to provide innovative solutions to fluid flow problems (Tu et al. 2008). The trend of engineering design is increasingly shifting toward more-complex, powerful CFD techniques for multi-physics phenomena (Elder et al., 2003).

In a nut shell, the purpose of Computational Fluid Dynamics is to use computers to approximate solutions of conservation equations governing fluid mechanics or in other words, to provide useful approximations of the real solution in many hitherto intractable fluid flow phenomena. In engineering applications, CFD can be used to clarify operational issues by providing insight of fluid behaviour and physical processes. CFD also assists in the development of new designs by allowing the analysis of fluid flow

problems in detail, faster and earlier in the design cycle and hence, reducing the cost and lowering the risks involved in the design process which traditionally relies on building experimental test-rig or prototype. An illustrative example is the design of an aircraft which in the past was mainly based on approximate theories of fluid flow, on engineering data sheets and relied heavily on vast amount of wind tunnel testing. For example in the new design of Boeing 787, most of the aircraft components and performances were designed and tested in the conceptual/preliminary stage using CFD (presented in Fig. 1.1) and that reduces significantly the number of costly wind tunnel validations and flight tests (Johnson et al., 2005; Desai, 2003). The increased use of CFD early in the design stage of any engineering device becomes evident and this trend is only likely to grow more pronounced in the future as comptuers become increasingly cheaper and more powerful. For instance, Fig. 1.2 shows the number of publications regarding CFD- based Optimization (Thévenin & Janiga, 2008). It should be noted that "Optimization" means not only the best (design) but also "better" and "improvement". According to the Fig. 1.2, the number of papers related to design by using CFD in 2006 is 12 ~ 13 times larger than in 1999 as a reference year.

Figure 1.1. CFD contributions to Boeing 787 (AIAA Pacific Northwest Section http://pnwaiaa.org)

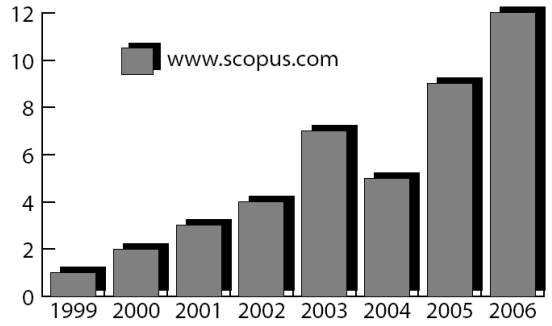

Figure 1.2. Number of Publications regarding CFD/Optimization based on the search tool Scopus. The year 1999 was retained as reference year and given to a value of 1 (Thévenin & Janiga, 2008).

1.2. Dynamic mesh

As engineering application of CFD becomes popular, engineers and researchers in industries demand to simulate their machines and devices in more realistic situations. In the early application of CFD, their machines and devices are modeled in a simplified way since computational resources are limited in each company. For example, aircraft consists of only body and main wing, and air flow around it is often assumed to be inviscid. However, as computational hardware performance is constantly and increasing improving, not only full CAD modeling and compressible Navier-Stokes simulation but also dynamic (unsteady) simulation can be realized nowadays (Tinoco et al., 2005; Cebeci et al., 2005).

Although, much progress has been made in CFD over the past years toward the development of a reliable tool for practical engineering designs, some issues and challenges remain to be addressed. In most engineering designs such as aircraft, often the device of interest has dynamic components and its performance analysis requires fully-coupled simulations to describe the influence of the moving shape on the flow (Batina, 1991; Salas, 2006). At first level of complexity, their computational models are no longer

fixed in the space and time. It is essential, therefore, to consider computational techniques that include the motion of these components and can successfully approximate the unsteady flow field encountered on these moving parts. For this purpose, dynamic mesh method was developed.

Dynamic mesh method requires special treatments and techniques to simulate dynamic motion precisely and efficiently. For instance, when dynamic mesh method is incorporated into flow solver, an additional geometric constraint called “Space Conservation Law (SCL)” should be introduced to ensure numerical stability. This is not required in our real world but in the computational world discretized by mesh or grid, since artificial mass may be generated by (moving) mesh convection and affects the accuracy and efficiency of flow simulation. SCL was considered in late 1970s and many researchers proposed methods to incorporate it into discretized governing equations, i.e., mass conservation and momentum equation, in 1980s. For a thorough review, see Zhang et al. (1992) and Lai & Przewaks (1994).

In addition, after establishing procedures for handling SCL, another issue is how to move mesh efficienty and precisely for applying dynamic mesh method to many types of flow problems (Jasak & Tukovic, 2007). Generally, coding of boundary motion and those of internal-point motion are distinguished from each other. This is because while the feature of physical/mechanical motion can be defined on boundary points, most CFD programs require specifying the position of every vertex in each time-step. The movement of internal points should accommodate boundary motion with keeping the whole mesh quality and validity. To handle this problem, there are many mesh-manipulation approaches. For instance, "mesh (re) generation" technique, like smoothing

is used. However, in practical way, this is quite limited since it becomes difficult to prescribe solution-dependent motion or perform mesh motion on dynamically adapting meshes. In real engineering world, one of the most conventional methods is deforming (or moving) mesh approach. In this method, internal points interact with each other and determine their own positions at each time-step. The movement of vertices follows simple algebraic rules such as constant displacement (constant mesh speed), applying algebraic formula (e.g., spring analogy) or solving motion equations; Laplace equation. Another useful approach is mesh-topology changing. Mesh topology, connectivity and resolution need to be updated or the mesh needs to be locally regenerated during calculation. In some cases, deforming mesh method is combined with topological changes, where the number or points, faces or cells in the mesh or its connectivity change as well as the mesh points move during the simulation. Each approach to the dynamic mesh problem has in fact its own advantages and drawbacks. Thus, the user trying to simulatte dynamic motion of an engineering device in CFD should choose an appropriate dynamic mesh method as well as sutable flow solver. Different concepts and issues on dynmaic mesh problem will be disccused in more detail in Chapter 2.

1.3. CFD software packages

As discussed in the previous section, researchers, students and engineers have to learn, to select and some times, to develop numerical methods before using CFD as a research or an engineering tool. Thus, in the early age of CFD, it took much time for them to develop their own computer program and configure it for their own specific topics and purposes. With the progress of computational technology, commercial CFD

software emerged after 1980s. Especially, the software packages are demanded in industries. This is because it can be used as a design tool without programming and debugging which are time-consuming. For example, ANSYS®, CFX®, Fluent® and STAR-CD® from ANSYS Inc. are famous among many types of industries (Boysan et al., 2009). Though users need neither to debug nor to modify it by themselves, each licensee has to pay contract fees to software developers to introduce and use it.

As "Open-source" principle is expanding, source codes for part of software become freely available. Among these types of software packages in CFD field, OpenFOAM® (Open Source Field Operation and Manipulation) is the most popular in academic organizations and industries (OpenCFD, 2013). It has been discussed and modified through the internet communication and used in many peer-reviewed papers. OpenFOAM was first released in 2004 and is regularly updated, and expanded by the community. It can be installed on a personal computer or set up on a network of computers taking advantage of parallel processing. In OpenFOAM, libraries written in C++ are used to create applications. Applications consist of solvers or/and utilities. Solvers are designed to solve a specific physical problem in continuum mechanics and utilities are used to perform tasks that involve data manipulation. OpenFOAM has many libraries, solvers and utilities as default. The noble implementation of mesh motion equation and topology change is also developed by Jasak & Tukovic (2010) in this free software package. The open source nature of OpenFOAM also means that any users can write their own solvers, although enough understanding of the physics and underlying method for specific problems are required. Their custom solvers and utilities are available to others through a broad community.

Even though CFD is becoming a part of design and development stages in industries and a powerful research tool in academia, it should be noted that CFD remains "approximation" with the physical quantities such as velocity, pressure and temperature defined only in the discretized time and space. Despite the fact that many commerical or open-source CFD codes are available, proper validation and numerical assessments are still required to gain confidence in the solutions and simulate the real physics of the problem (Tu et al. 2008). Note that in most cases, physical models are required to simulate complex flows such as turbulence, chemical reaction and multi-phase flows. In addition to the governing models, suitable numerical methods (e.g., discretization, grid resolution, code algorithm, etc.) should also be selected carefully so as to approximate the solution of the model and simulate real flows on a computer. The numerical solutions needed to be properly validated against experimental data. Otherwise, the solutions become unphysical even if they have beautiful visualized results, particularly the CFD alogrithm is becoming increasingly sophicated.

1.4. Objective and thesis organization

In this research thesis, the purpose is to apply and assess CFD, particularly the dynamic mesh techniques to generate precise flow prediction and to simulate performance of two engineering devices, namely the needle-free jet injector and a diaphragm-less shock tube, which both have fluid dynamics resulted from a moving boundary. All the simulations were done using the OpenFOAM software packages and this work contributes to this open-source code by providing validation of the algorithm available in this CFD code.

Since the main challenge of this CFD work deals with moving grids, Chapter 2 first provides an overview on the dynamic mesh methods in CFD. The most widely used techniques and their limitations are described and its implementation in the open soruce software OpenFOAM is discussed.

Chapter 3 applies the numerical methods to study the fluid mechanics in a air-powered needle-free injection device. This is the first attempt to combine several CFD techniques to simulate the liquid jet generated from the impact of a moving plunger and emerged from the needlefree injector and the reults are compared to those obtained. A number of interesting features revealed from CFD are discussed including the high speed jet characteristics and its properties during the needl-free liquid injection. The content of this chapter was published at the 21st Annual Conference of the CFD Society of Canada, Sherbrooke, Quebec, May 6-9, 2013; the extended work is currently under review for publication in Engineering Applications of Computational Fluid Mechanics.

Using the CFD tools with dynamic mesh method, Chapter 4 presents a performance analysis of a diaphragm-less shock tube driver design where shock wave is generated by a system of high/low pressure regions and the movement of an inner wall to replace the traditional use of thin Mylar diaphragm to separate the pressure sections. The results obtained from the CFD illustrates the important roles played by the different shock tube parameters such as the opening time, driver pressure ratio. The numerical results were compared with experimental measurement and published at the Proceeding of the 29th International Symposium on Shock Waves, in Madison, WI, July 14-19, 2013.

Finally, Chapter 5 provided an overall conclusion and future directions of this research work.

Chapter 2

Dynamic Mesh Method

2.1. General overview

In many engineering CFD applications, the computational domain changes with time due to the movement of boundaries. The movement is determined either by external effects (e.g., a piston driven by external pressure) or by calculation as a part of the solution such as free-surface flow. Dynamic mesh method can handle these problems and be essential especially for practical engineering uses. For example, turbo-machinery, pumps and internal combustion engines are typical products. These dynamic motions can be modeled as simple methods such as linear deformation of the boundaries, solid body motion and algebraic-expressions surface. However, in complex cases, we have to handle time-varying geometry, solution dependent motion and mesh deformation obtained by solving a mesh motion equation (Weller et al. 1988).

In this study, Finite Volume Method (FVM) is selected as discretization method and in the following sections, two types of dynamic mesh methods in finite volume formulation are discussed in detail.

2.2. Deforming/moving mesh

Figure 2.1 shows the mesh deformation schematically (Jasak & Tukovic, 2010). There are computational domain represented as Ω, its inner surface S_1 and outer surface S_2 at a given time, t. They compose valid computational mesh. After a time interval dt, Ω changes its shape into a new configuration Ω' by the movement of S_1, in other words, displacement between S_1 and S_1'. A mapping between Ω and Ω' is sought such that the mesh on Ω forms a valid mesh on Ω' with minimizing distortion of control volumes. As a result of this motion, inner point P moved to P'.

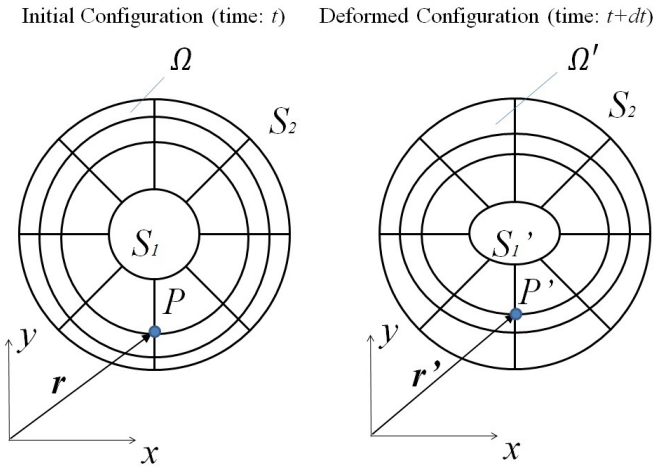

Figure 2.1. Schematic showing the mesh deformation

2.3. Moving mesh discretization on finite volume method

Moving mesh on FVM is formulated by applying the integral form of the governing equation over an arbitrary moving volume V bounded by a closed surface S. For a tensorial property ϕ

$$\frac{d}{dt}\int_V \rho\phi dV + \oint_S \rho\,\mathbf{n}\cdot\left(\mathbf{U}-\mathbf{U}_b\right)\phi dS - \oint_S \rho\gamma_\phi\,\mathbf{n}\cdot\nabla\phi dS = \int_V S_\phi dV \qquad (2.1)$$

where ρ is the density, **n** is the outward unit normal vector on the boundary surface, **U** is the fluid velocity, $\mathbf{U}_b$ is the boundary mesh velocity, γ_ϕ is the diffusion coefficient and S_ϕ is the volume source/sink of ϕ (Jasak & Tukovic, 2010).

As the volume V is not fixed in space any more, its motion is characterized by the motion of its bounding surface S with the grid (or mesh) velocity $\mathbf{U}_b$. Comparing with a static mesh, the second-order FV discretization of Eq. (2.1) shows only two differences:

- The temporal derivative introduces the rate of change of the cell volume
- The mesh motion flux accounts for the grid convection.

Figure 2.2 is a sample of finite volume cell (control volume) in which Eq. (2.1) is evaluated. The unstructured FVM splits the computational domain into a finite number of polyhedral cells bounded by complex polygons which do not overlap and completely cover the domain. The temporal dimension is split into a finite number of time steps and the equations are solved in a time-marching manner. As shown in Fig. 2.2, the sample cell around the computational point P located in its centroid, a face f, its area S_f and unit normal vector $\mathbf{n}_f$ with the neighboring computational point Q.

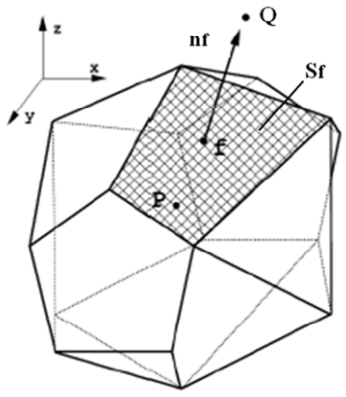

Figure 2.2. Control volume (cell) on FVM

2.4. Space Conservation Law (SCL)

Solving Navier-Stokes equations has no new problems when the location of grid is known as a function of time. The convective fluxes are calculated by using the relative velocity components on the cell faces. However, conservation of mass is not always satisfied if the grid velocity is used to calculate the mass flux (Demirdzic & Peric, 1988; Ferziger & Peric, 2004). For simple example, the mass-conservation equation is considered with implicit Euler time integration. The following assumptions are assumed:

- Control volume (CV) is rectangular whose area $\Delta S = \Delta x \Delta y$
- Fluid is incompressible; ρ is constant
- Fluid velocity is constant; $\mathbf{U} = (u, v)$ is neither a function of time nor space
- Boundary grid (or mesh) velocity $\mathbf{U_b} = (u_b, v_b)$ is a function of space but not of time

Figure 2.3 shows the relative sizes of the CV at the old and new time. The size of the control volume is grows with time (Ferziger & Peric, 2004).

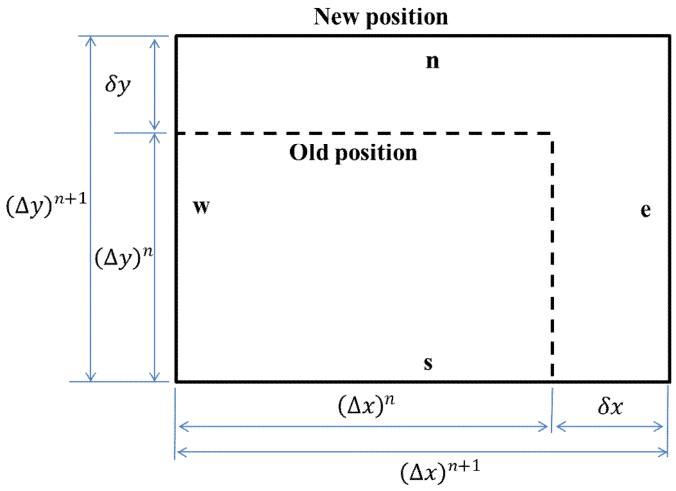

Figure 2.3. A rectangular control volume whose size increases with time

The discretized continuity equation for the CV with the implicit Euler scheme is given by

$$\frac{\rho\left\{(\Delta S)^{n+1}-(\Delta S)^{n}\right\}}{\Delta t}+\rho\left\{(u-u_b)_e-(u-u_b)_w\right\}^{n+1}(\Delta y)^{n+1} + \rho\left\{(v-v_b)_n-(v-v_b)_S\right\}^{n+1}(\Delta x)^{n+1}=0 \tag{2.2}$$

The contribution of fluid velocity is in the above equation cancels out and the difference in grid velocities remains:

$$\frac{\rho\left\{(\Delta S)^{n+1}-(\Delta S)^{n}\right\}}{\Delta t}-\rho\left\{(u_b)_e-(u_b)_w\right\}(\Delta y)^{n+1}-\rho\left\{(v_b)_n-(v_b)_S\right\}(\Delta x)^{n+1}=0 \tag{2.3}$$

The difference in grid velocities at the opposite CV sides can be expressed as

$$(u_b)_e-(u_b)_w=\frac{\delta x}{\Delta t} \tag{2.4}$$

$$(v_b)_n-(v_b)_s=\frac{\delta y}{\Delta t} \tag{2.5}$$

Area of the CV is also expressed as:

$$(\Delta s)^{n+1}=(\Delta x\Delta y)^{n+1} \tag{2.6}$$

$$(\Delta s)^{n}=\left\{(\Delta x)^{n+1}-\delta x\right\}\left\{(\Delta y)^{n+1}-\delta y\right\} \tag{2.7}$$

Substituting Eqs. (2.4) ~ (2.7) into the Left Hand Side (LHS) of the Eq. (2.3) we have:

$$\mathbf{LHS}=\frac{\rho}{\Delta t}\left[(\Delta x\Delta y)^{n+1}-\left\{(\Delta x)^{n+1}-\delta x\right\}\left\{(\Delta y)^{n+1}-\delta y\right\}\right]-\frac{\rho}{\Delta t}\left\{\delta x(\Delta y)^{n+1}+\delta y(\Delta x)^{n+1}\right\}$$

$$\therefore \mathbf{LHS}=-\frac{\rho}{\Delta t}\delta x\delta y\neq 0 \tag{2.8}$$

Thus, one find that the discretized mass conservation is not satisfied. There is a mass sink as follows:

$$\delta\dot{m}=-\frac{\rho}{\Delta t}\delta x\delta y=-\rho\left\{(u_b)_e-(u_b)_w\right\}\left\{(v_b)_n-(v_b)_s\right\}\Delta t \tag{2.9}$$

The same error is calculated with the explicit Euler scheme but the sign is opposite (mass source). Even through this error is a first-order discretization error in time step with constant grid velocities, "artificial mass source/sink" may accumulate with time and cause serious problems. The error is eliminated if only one set of grid lines moves or if the grid velocities are equal at opposite CV sides. When one uses higher schemes such as the Crank-Nicolson and three-time-level implicit scheme, the continuity equation can be satisfied. However, in more general cases like fluid and/or grid velocities are not constant with respect to time and space, these schemes can also generate artificial mass sources/sinks.

Mass conservation can be obtained by applying Space Conservation Law (SCL). This is thought of as the continuity equation in the limit of zero fluid velocity:

$$\frac{d}{dt}\int_V dV - \oint_S \mathbf{n}\cdot\mathbf{U}_b\, dS = 0 \tag{2.10}$$

Equation (2.10) expresses the conservation of space when the CV changes its shape and/or position with time. Applying the midpoint rule and central-difference schemes to the above equation yields:

$$\frac{V_p^{new} - V_p^{old}}{\Delta t} - \sum_f \left(n_f \cdot \mathbf{U}_b\right) S_f = 0 \tag{2.11}$$

The difference between the new and the old CV can be obtained by summation of volumes δV swept by the CV faces during the time step, which is shown in Fig. 2.4 (Ferziger & Peric, 2004).

$$\frac{V_p^{new} - V_p^{old}}{\Delta t} = \frac{V_p^{n+1} - V_p^{n}}{\Delta t} = \frac{\sum_f \delta V_f}{\Delta t} \tag{2.12}$$

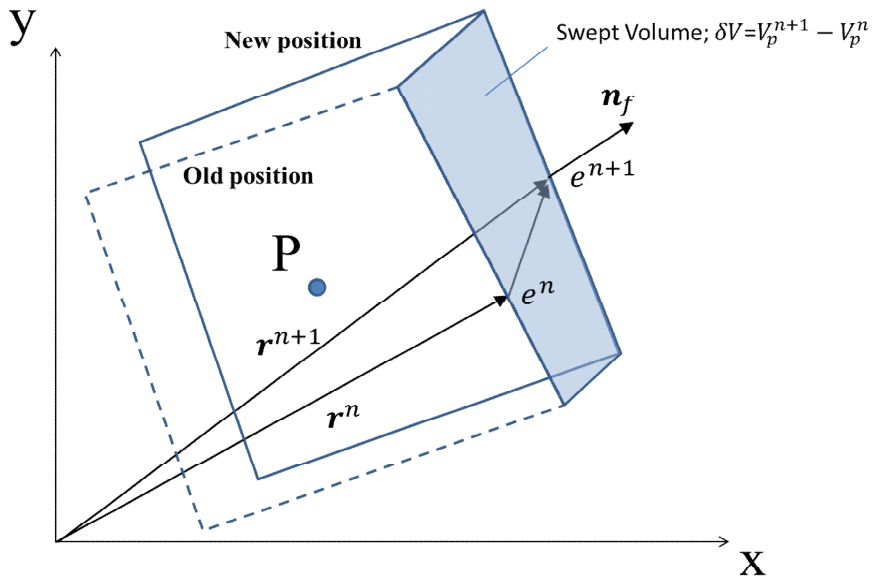

Figure 2.4. A typical CV at two time steps and the swept volume by a cell face

By comparing these two equations, the swept volume by a cell face is:

$$\dot{V}_f = \left(n_f \cdot \mathbf{U}_b\right)_f S_f = \frac{\delta V_f}{\Delta t} \tag{2.13}$$

The grid movement affects only mass fluxes. If the positions of the CVs during all time steps are known, the grid velocity $\mathbf{U}_b$ can be calculated. This is expressed at the cell face center:

$$\mathbf{U}_b \cong \frac{r_f^{n+1} - r_f^n}{\Delta t} \tag{2.14}$$

When the mesh moves in only one direction, the above approach causes no problems. However, if the mesh moves in more than one direction, it is difficult to satisfy mass conservation using the expressions as equation; artificial mass sources/sinks may be made. These errors can be avoided by computing the volumes which is defined by the

cell face positions at each time step. The mass flux through a cell face, f can be calculated by:

$$\dot{m}_f = \int_{S_f} \rho \mathbf{n} \cdot (\mathbf{U} - \mathbf{U}_b) dS \cong \rho_f (\mathbf{U} \cdot \mathbf{n})_f S_f - \rho_f \dot{V}_f \tag{2.15}$$

Thus, for the implicit Euler scheme, the discretized continuity equation is given by:

$$\frac{(\rho \Delta V)^{n+1} - (\rho \Delta V)^n}{\Delta t} + \sum_f \dot{m}_f = 0 \tag{2.16}$$

The unsteady term should be treated as satisfying the space conservation law. In addition, the treatment is different between incompressible and compressible flow.

For incompressible flow

The contribution of the mesh movement to the mass fluxes has to cancel the unsteady term. This leads the mass conservation equation to:

$$\int_{S_f} \rho \mathbf{n} \cdot \mathbf{U} dS = 0 \tag{2.17}$$

If the volume change and mass fluxes are calculated as above, the conservation is ensured. Therefore, the mesh movement does not have any influence on the pressure-correction equation.

For compressible flow

A special care is required since density is not constant any longer. So, density has to be determined to satisfy both space and mass conservation equations. The problem is that the mass conservation equation has the cell-center density, ρ in the unsteady term and cell-face density, ρ_f in the mass fluxes. If the density changes rapidly in both space and

time, it is very difficult to evaluate it. Especially, small time step should be applied when one wants to use the following approximation for the density varying drastically:

$$\rho_f^* = \frac{1}{2}\left(\rho_f^n + \rho_f^{n+1}\right) \tag{2.18}$$

Finally, topological changing is considered. When the number of CVs and their connectivity change, we need the old solution (values at previous time step) to approximate volume integrals over the new CV. If midpoint rule is used for this calculation, the old solution is interpolated to the locations of the new CV-centers. One possible procedure is indicated below:

- Compute gradient vectors at the center of each old CV
- Find the nearest center of an old CV for each new CV-center
- Interpolate the old value at the new CV-center linearly;

$$\phi_{C^{new}}^{old} = \phi_{C^{old}}^{old} + (grad\phi)_{C^{old}}^{old}\left(r_{C^{new}} - r_{C^{old}}\right) \tag{2.19}$$

However, a fine grid should be used to obtain better results when one uses the above approximation. Other higher interpolation like quadratic and cubic ones would be better candidates if the mesh is coarse locally or globally.

Finally, it is noted that OpenFOAM used in this study introduces flux correction and non-orthogonal correction into discretized governing equations to satisfy SCL (Jasak & Tukovic, 2008).

2.5. Mesh motion equation

The next step is how to determine the positions of internal vertices following the boundary motion at each time step. In the present work, a mesh motion equation is

applied. In the equation boundary motion acts as a boundary condition and determines the position of both boundary vertices and internal ones. The motion is characterized by the spacing between nodes, which are changed by stretching and squeezing. This mesh motion equation has mainly four types (Kassiotis, 2008):

- Spring analogy
- Linear plus torsional spring analogy
- Laplace equation with constant and variable diffusivity
- Linear pseudo-solid equation for small deformations

These can be used in the cases where the resolution is not changing too much during the mesh motion; i.e., relatively small changes in mesh occur, so that cell density changes do not affect the results during the computations.

2.6. Topological changing method

In extreme cases of boundary deformations, mesh quality can be deteriorated dramatically and we cannot obtain a reliable solution by applying only mesh deforming method. Even worse, it takes more time to converge the flow field. In this case, topological changing method is introduced. During simulation, the number of points, faces, cells and (or) mesh connectivity changes. In engineering applications, three types of topological changing methods are particularly important.

Cell layer addition/removal

A set of oriented faces is assigned to add another layer to the current ones or remove one layer from them. Usually, the thickness threshold value is set to do the above operations. Figure 2.5 shows layer addition and removal during the motion of a cone in a

rectangular mesh (Jasak, 2006).When the mean cell thickness exceeds a prescribed value, new cells are added. On the contrary, when the thickness is lower than a prescribed minimum thickness, one (cell) layer is removed. This is often used for linear piston or cylinder movement.

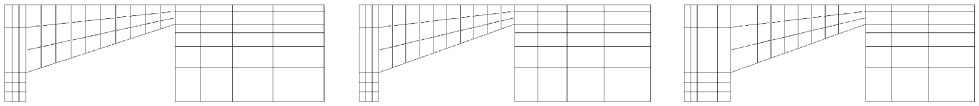

Figure 2.5. A moving cone in a rectangular mesh using cell layers addition/removal (Jasak, 2006)

Sliding interface

Changing the cell connectivity dynamically in the interface between meshes, it enables to keep a high mesh quality in complex geometries like internal combustion engines or mixers. In Figure 2.6, the sliding-interface operation is applied to mixer geometry (Jasak, 2006).

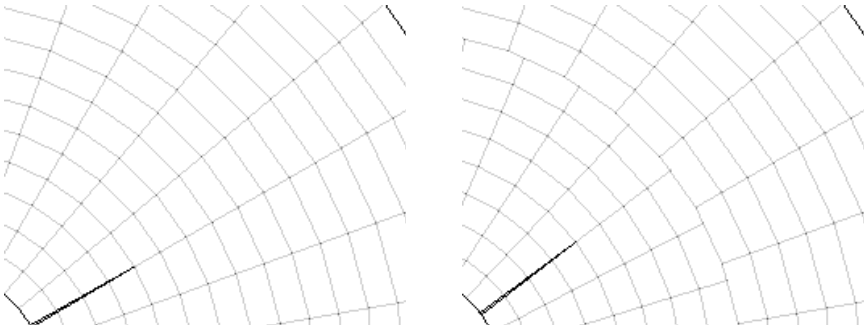

Figure 2.6. Sliding mesh interface applied to the interior part of a mixer mesh (Jasak, 2006)

Attach/detach boundary

This is not directly involved with mesh motion but related to the volume connectivity. In the operation of attach/detach boundary, two new boundary entities are created from a

list of internal faces in order to separate or connect two distinct volumes in the same mesh. In Fig. 2.7, the use of attach-detach boundary is shown when a T junction is attached and detached (Jasak, 2006). This is quite useful in the application of internal combustion engines, such as a valve opening/closing action.

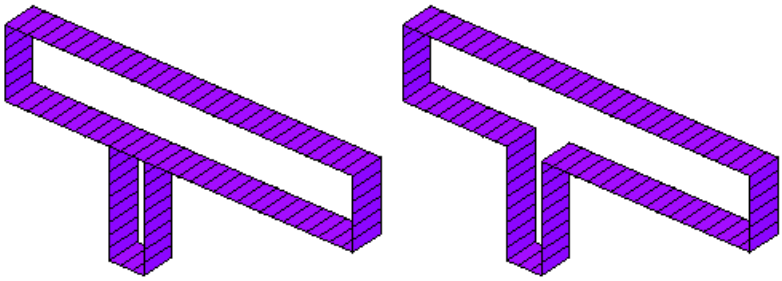

Figure 2.7. Attach-detach boundary applied to a T-shape junction (Jasak, 2006)

When the mesh is not only deforming but also changing its topology in time step by time step, scalar and vector fields are mapped from the old mesh to the new mesh. Furthermore, surface fluxes are recalculated when sliding interfaces are used and new boundary conditions are imposed when boundary are attached. Therefore, it should be noted that topology changing is typically associated with mapping errors, which mean either non-smooth local field values or the loss of global conservation.

2.7. Mesh validity and quality

In this section, mesh definition in FVM is discussed firstly. Creating a valid mesh is the first step of simulating flow field correctly and precisely (of course, valid physical model in other words, appropriate governing equations should be selected). Even if the valid mesh is made and good physical models are chosen, we have to try the same

simulation in the meshes with different mesh density. This is because the solution is influenced by mesh-induced discretization errors. This is referred as to "Mesh dependency" (Jasak, 1996).

2.7.1. Mesh validity

A valid mesh is a pre-requisite for a reliable numerical solution and a critical ingredient of mesh motion. The investigation of mesh validity can be separated into *topological* and *geometrical* tests. The topological tests can be performed without knowing the actual point positions, while the geometrical ones deal with the shape of cells and the boundary (Demirdzic & Peric, 1988; OpenCFD, 2013).

Face based mesh definition

In the *face-addressed* mesh definition, a polyhedral mesh in FVM is defined by the following components:

- A list of points. For every point, its space co-ordinates are given; the point label is implied from its location in the list.
- Every point must be used in at least one face.
- A list of polygonal faces, where a face is defined as an ordered list of point labels. Faces can be separated into internal (between two cells) and boundary faces. Every face must be used by at least one cell.
- A list of cells defined in terms of face labels. Note that the cell shape is unknown and irrelevant for discretization.
- Boundary faces are grouped into patches, according to the boundary condition. A patch is defined as a list of boundary face labels.

Face orientation is determined using the right-hand rule and the face list will first collect all internal faces and then all boundary faces patch by patch in the order of patch definition. Internal faces are ordered to contain all faces from the first cell with the increasing neighbor label, followed by the faces owned by the second cell *etc*. This approach has proven to be robust and easy to handle as it enforces strict and unique face ordering (Demirdzic & Peric, 1988; OpenCFD, 2013).

Topological tests

Topological validity tests consist of the following criteria:

- A point can appear in a face only once
- A face can appear in a cell only once. A face cannot belong to more than two cells. A boundary face can belong to only one patch
- Two cells can share no more than one face
- Collecting all faces from one cell and decomposing faces into edges, every edge must appear in exactly two cell faces
- Collecting all faces from the boundary and decomposing faces into edges, every edge must appear in exactly two boundary faces.

The first four conditions control the validity of the mesh definition while the last two conditions check that all cells and the boundary hull are topological closed. Additionally, mesh ordering rules are checked and enforced. If topological changing method is applied, the above rules are strictly satisfied after changing from the old mesh to the new mesh during simulation.

Geometrical tests

Geometrical tests deal with the positivity of faces areas and cell volumes, as well as convexity and orientation requirements. Geometrical validity criteria can be summarized as follows:

- All faces and cells must be weakly convex
- All cells must be geometrically closed: the sum of the outward-pointing face area vectors for a cell faces must be zero to machine tolerance
- The boundary must be geometrically closed
- For all the internal faces, the dot-product of the face normal vector $\mathbf{n}_f$ and the $\mathbf{d}_\mathbf{f} = \overrightarrow{\mathbf{PQ}}$ in Fig. 2.2 must be positive; this is usually termed the *orthogonality test*:

$$\mathbf{d}_\mathbf{f} \cdot \mathbf{n}_f > 0 \qquad (2.20)$$

We shall assume the existence of a topologically and geometrically valid mesh as a starting point for dynamic mesh. In the moving mesh method, mesh topology remains unaffected and only the point positions change. Thus, preserving the mesh quality only relates to the geometrical tests. Moreover, once the convexes and orthogonality tests are satisfied, an initially valid mesh remains valid if no triangles or tetrahedra are inverted (Demirdzic & Peric, 1988).

2.7.2. Mesh quality

Mesh skewness and non-orthogonality

The famous parameters judging mesh quality in FVM are skewness and non-orthogonality. Figure 2.8 illustrates the definition of skewness and non-orthogonality. The mesh skewness is defined as the ratio between the length of *m* and *d* shown in Fig.

2.8 (a). It is a measure on how much the face center f_c is displaced from the line connecting the two cell centers (PQ). In an ideal cell there is no skewness and the face center is located on this line. A low skewness is desired to ensure that the interpolation from the cell centers to the face center is accurate.

On the other hand, non-orthogonality is defined as the angle α_N between the face normal and the line connecting the two cell centers in Fig. 2.8 (b). Minimizing the truncation error on the diffusion term requires a low non-orthogonality (Bos, 2010).

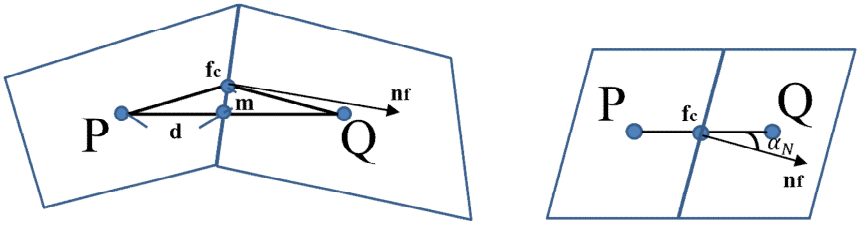

(a) Skewness (b) non-orthogonality

Figure 2.8. Definition of mesh skewness and non-orthogonality

Discretization error

A valid mesh does not always insure the reliable solution since every mesh has an error called discretization error. Therefore, the important thing is how this error can be minimized without increasing computational cost too much. At least the following two things should be considered in addition to generate a valid mesh (Ferziger & Peric, 2004).

Local mesh refinement

In most cases, important physical phenomena happen in a local flow field (for example, boundary layer near walls and interface between two fluids in VOF solver). Therefore, it is a big advantage for users to have some knowledge about the flow physics before making a mesh in order to refine the mesh in the region where important physics appear. This enable for us to obtain a good result without increasing computational costs

such as time, memory and data storage.

Global mesh refinement

After making a solution-adapted mesh, one should examine the effect of changing mesh density as keeping the ratio of between local mesh densities. This refinement should be done systematically and substantially. Systematic refinement means that the mesh topology and relative spatial density of grid vertices should remain comparable on all grid levels. Usually, users prepare 3 types of mesh as coarse, base and fine. The base and fine meshes have mesh density twice and four times as large as coarse one respectively.

It is noted that applying dynamic mesh method should neither deteriorate mesh skewness and non-orthogonality nor change the solution-adaptive mesh distribution. Especially, boundary conditions are taken care in case of using mesh motion solvers in mesh deformation methods.

2.8. Dynamic mesh application in OpenFOAM

In this thesis, the OpenFOAM® CFD software package is used to apply dynamic mesh method (OpenCFD, 2013). OpenFOAM supports both of moving mesh and topological changing methods (Jasak & Tukovic, 2010). These are named *dynamicFvMesh* and *topoChangerFvMesh* of which the second includes topological changes. There are several types of operations in moving mesh and topology changes. Users have to prepare the file whose name is *dynamicMeshDict* for applying dynamic mesh to the simulation. However, if another file, *meshModifiers* exists in the case directory, this file is read firstly. It is useful when the user re-runs the simulation at the

time when he/she interrupted it. Moreover, other input files or data written in *dynamicMeshDict* are required depending on the method selected by the user.

2.8.1. Automatic mesh motion: *DynamicFvMesh*

In OpenFOAM, an automatic mesh motion algorithm has been adopted. A second-order FEM scheme is applied and the user defines how the vertices on the boundary move, using a set of boundary conditions (Demirdzic & Peric, 1988). The boundary motion is built into to code and can be an arbitrary function of the solution. Therefore, nothing is done in advance of the simulation. A Laplace equation is solved on the vertices to calculate the motion of all vertices based on the boundary motion. This equation is solved directly on vertices as doing it on volumes is not satisfactory. There are a number of available Laplacian solvers in OpenFOAM. Their names and descriptions are:

displacementLaplacian

The equations of cell motion are solved based on the Laplacian of the diffusivity and the cell displacement. For applying this solver, one should specify the final displacement of mesh components as well as the mesh displacement of the internal field.

velocityLaplacian

The equations of the Laplacian of the diffusivity and the cell motion velocity are solved. This code deals with the boundary velocities instead of the final motions, so a care has to be taken when determining the dimensions. The user determines the velocity at which each single boundary moving. It is used when an order of magnitude of the maximum displacement is known to be not too big.

LaplaceFaceDecomposition

This is applied when the order of magnitude of the maximum displacement is not known or known to be big. The mesh is rebuilt after a decomposition of all cells and faces and the Laplace smoothing equation is solved by Finite Element Method. It increases the robustness. However, it increases the computational cost compared to the *velocityLaplacian* solver.

SBRStress

This is a displacement model solving the Laplacian of diffusivity and the *cellDisplacement*. It also considers the solid body rotation term in calculations.

In mesh motion solvers, the mesh spacing and quality is controlled by variable *diffusivity*. Changing the diffusivity implies redistribution of the boundary motion through the volume of the mesh. The definition of valid motion from an initially valid mesh implies that no faces or cells are inverted during motion, which helps to preserve mesh validity and quality. In OpenFOAM, users can select diffusivity models from as follows:

Quality based methods

The diffusion field is a function of a cell quantity measure. There are four types and these names are following:

- *uniform*

The mesh manipulation is done uniformly for all moving boundaries by stretching or squeezing with the same ratio for all the cells in each region.

- *directional*

The mesh stretching or squeezing is done proportionally to the direction of the motion. The main idea in this case is that the mesh manipulation is done by considering the slipping boundaries. Two scalar coefficients are required, one defining the mean cell non-orthogonality and the other one to determine the mean cell skewness.

- *motionDirectional*

The mesh manipulation is done by prioritizing the moving body and adjusting the cells in a way that is more appropriate for the moving body. The same coefficients, the mean cell non-orthogonality and the mean cell skewness in the above method have to be specified.

- *inverseDistance*

The user specifies one or more boundaries. The diffusivity of the field is based on the inverse of the distance from that boundary.

Distance based methods

They are used together with the quality based method; *inverseDistance*. The diffusion field will be a function of the inverse of cell centre distance 'l' to the nearest selected boundary.

- *Linear*

The diffusivity field is based linearly on the inverse of the cell center distance to the nearest boundary.

- *Quadratic*

The only difference from the above is a quadratic relation instead of a linear one.

- *Exponential*

In this case the diffusivity of the field is based on the exponential of the inverse of cell-center distance to the selected boundaries.

One should specify the name of appropriate solver and the type of diffusivity model in *dynamicMeshDict*. This way the equations of cell motion will be solved according to the selected solver specifications and with help of mesh diffusivity models.

Stating again, the topology of the mesh remains constant and the only change in geometry, if any, will be done by stretching or squeezing the cells and node positions.

2.8.2. Topological changes: *TopoChangerFvMesh*

Topological changes in OpenFOAM have hierarchy and they are coded in object-oriented way. This enables for us to use the operations much easier than other CFD packages. The hierarchy has three structures.

1st structure: Primitive Mesh Changes

Primitive mesh manipulation consists of addition, modification (changing connectivity) or removal for a single point, a face or a cell in the mesh. The mesh is collapsed or built from empty space by the nine operations combining the above each element (3x3). They are much flexible but impractical and unfriendly to use. Therefore, they are executed in the batch way; the mesh is resolved, rebuilt and checked for its validity.

2nd structure: Mesh Modifiers

The second level of topological changes is called “mesh modifiers”. A mesh modifier bundles a set of primitive operations and has a triggering mechanism for a topological change. As we discussed in the previous section, typical examples are cell layer addition/removal, sliding interface and attach-detach boundary. After setting a topology modifier in a file, the execution is done automatically by the definition or trigger value such as minimum layer thickness in layer addition/removal.

3rd structure: Dynamic Mesh Objects (class)

Mesh modifiers are much more practical than primitive mesh changes. But, in an engineering problem, we apply complex and multi mesh modifications for the simulation. For example, in engine combustion, piston moves (layer addition/removal) along the inner surface of a cylinder (sliding interface) and valves open and close. OpenFOAM presents several types of dynamic mesh objects to simulate typical physical and engineering problems. They are called “class”.

2.8.3 Dynamic mesh implementation in OpenFOAM

This section presents how dynamic mesh works in OpenFOAM. The main focus is on the mechanism of dynamic mesh and visualization of mesh changing. For first example, *velocityLaplacian* is selected as a motion solver to move a sliding sleeve inside diaphragm-less shock tube with constant velocity. Secondly, an original class of *TopoChangerFvMesh* is applied to piston motion for a liquid jet injector. Through two examples, it can be observed how dynamic mesh effects on the mesh quality such as non-orthogonality and skewness.

A sliding sleeve inside diaphragm-less shock tube

The diaphragm-less shock tube facility is discussed and simulated by CFD in Chapter 4. In this section, the dynamic mesh mechanism for its CFD model is featured. To simulate the sliding sleeve motion, *velocityLaplacian* is used to an initial computational mesh indicated in Fig. 2.9. The wall located at left hand side of the boundary is moved with constant velocity, $\mathbf{U}_b$. Setting $\mathbf{U}_b$ as a part of boundary condition, the mesh velocity field, $\mathbf{U}_m$ can be calculated by solving the equation below:

The Laplace operator:

$$\nabla \cdot \left(\delta \nabla \mathbf{U}_\mathbf{m} \right) = 0 \tag{2.21}$$

Here, δ is constant or variable diffusion field to govern mesh motion. Boundary conditions for Eq. (2.21) include slip boundaries, symmetry planes and cyclic boundaries besides moving body boundary. $\mathbf{U}_m$ is used for modifying mesh point positions:

$$r_{new} = r_{old} + U_m dt \tag{2.22}$$

The choice to solve for motion velocity is related to the fact that it changes slower than point position and a better initial guess is available. For stationary meshes the velocity solution equals to zero everywhere and is less polluted by round-off errors than the point position field. For constant-velocity deformation the computational cost of solving the motion equation in terms of velocity becomes trivial comparing with choosing point position as the primitive variable. For better precision, the motion velocity on the boundary is calculated from the current and desired point position and the time-step. This approach avoids the accumulation of round-off errors associated with solving for motion velocity and using point position (Demirdzic & Peric, 1988).

Computational conditions are $\mathbf{U}_b$ **= (-100, 0, 0).** p_4 (driver pressure) = 0.8 MPa, p_1 (driven pressure) = 101,325 kPa and dt = 10^{-9}. For diffusivity field δ directional diffusivity model (discussed in Section 2.8.1) is selected and parametric study indicated in Table 2.1 is performed for coefficients of non-orthogonality and skewness to examine their influences on mesh quality. It is noted that diffusion field is identical if the coefficient ratio of non-orthogonality and skewness is same. The parametric study is applied to two types of geometry models shown in Fig. 2.9. It should be noted that mesh deformation is severe inside the expansion gap suggested in Fig. 2.9.

Case	(1) Non-orthogonality	(2) Skewness	Ratio (2)/(1)
1	1	2	2
2	0.1	2	20
3	0.01	2	200
4	0.001	2	2000
5	0.001	20	20000
6	0.001	200	200000

Table 2.1. Diffusivity coefficients for non-orthogonality and skewness

Figure 2.10 shows time histories of max non-orthogonality and max skewness for 6 cases. It is confirmed that the mesh quality is improved as the coefficient ratio increases for both two geometry models. OpenFOAM judges a bad mesh if the skewness is more than 4 in default setting. In terms of accuracy and convergent, non-orthogonality should be less than (at least) 90 deg since the calculations in Case 1 and 2 become divergent for both geometries. Visualization results in Fig. 2.11 show clear differences in mesh shape especially at the corner of the tube in Case 1 and 6 for 2 geometry models. Thus, an

appropriate selection of diffusivity coefficients is essential and makes the mesh move without high distortion otherwise dynamic simulation diverges due to mesh invalidity.

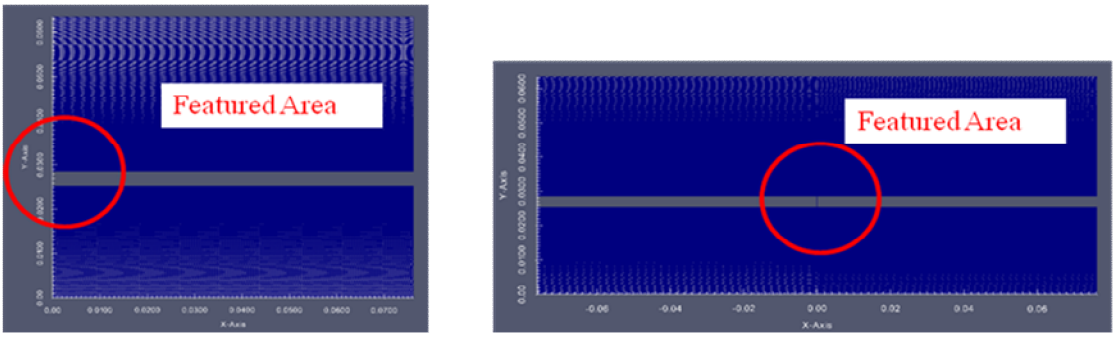

a) Geometry Model 1 **b) Geometry Model 2**

Figure 2.9. Two types of geometry models for the diaphragm-less shock tube

Geometry Model 1

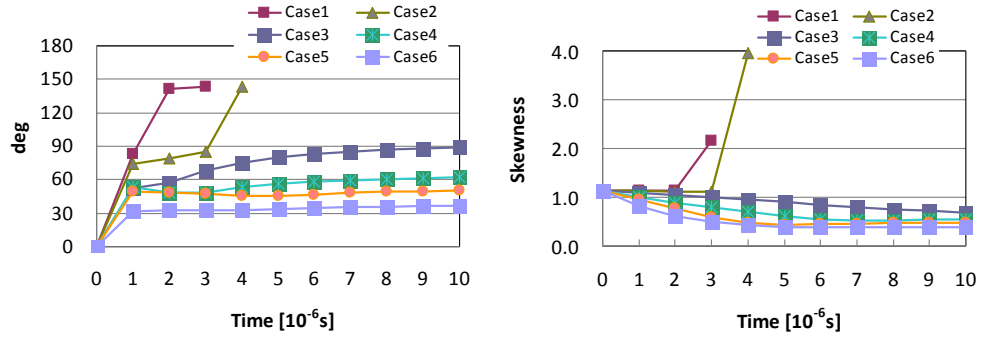

(a) Max Non-orthogonality (b) Max Skewness

Geometry Model 2

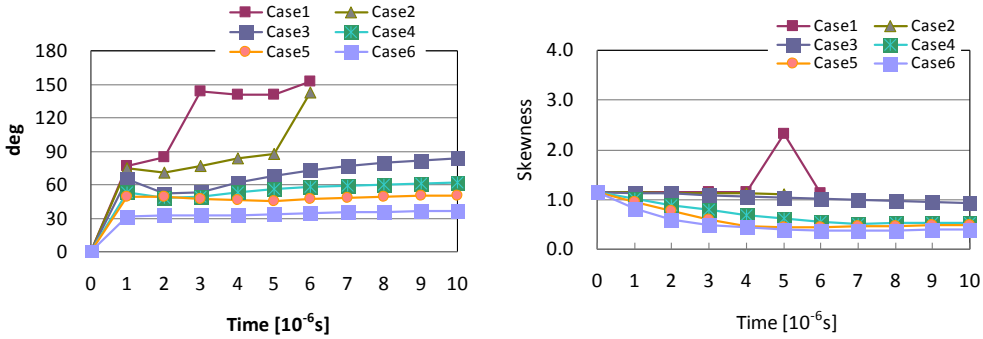

(a) Max Non-orthogonality (b) Max Skewness

Figure 2.10. Time history of mesh qualities for geometry model 1 and 2 of the diaphragm-less shock tube. a) max non-orthogonality; b) max skewness

Geometry Model 1

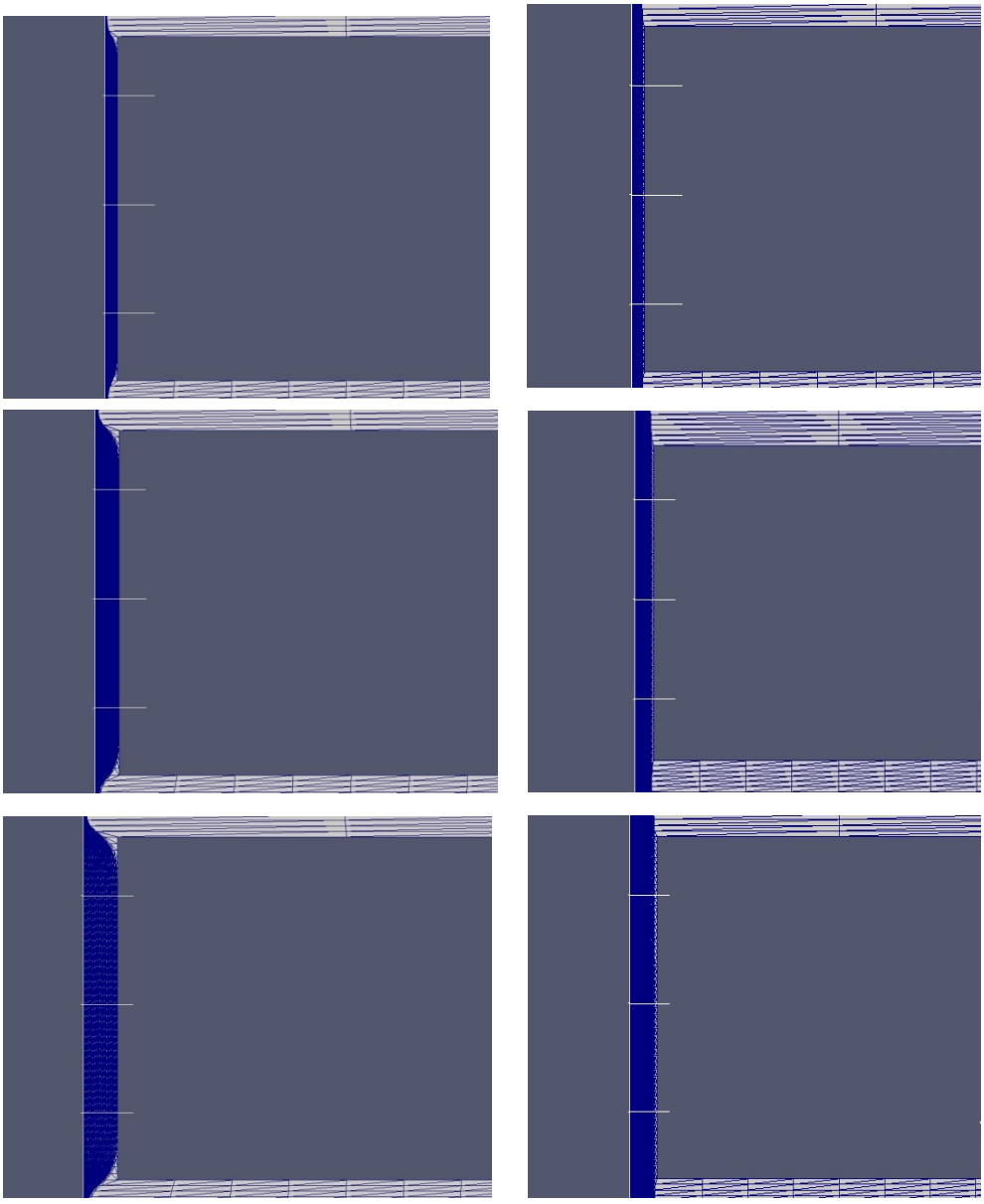

(a) Case 1 (b) Case 6

Figure 2.11. (continued)

Geometry Model 2

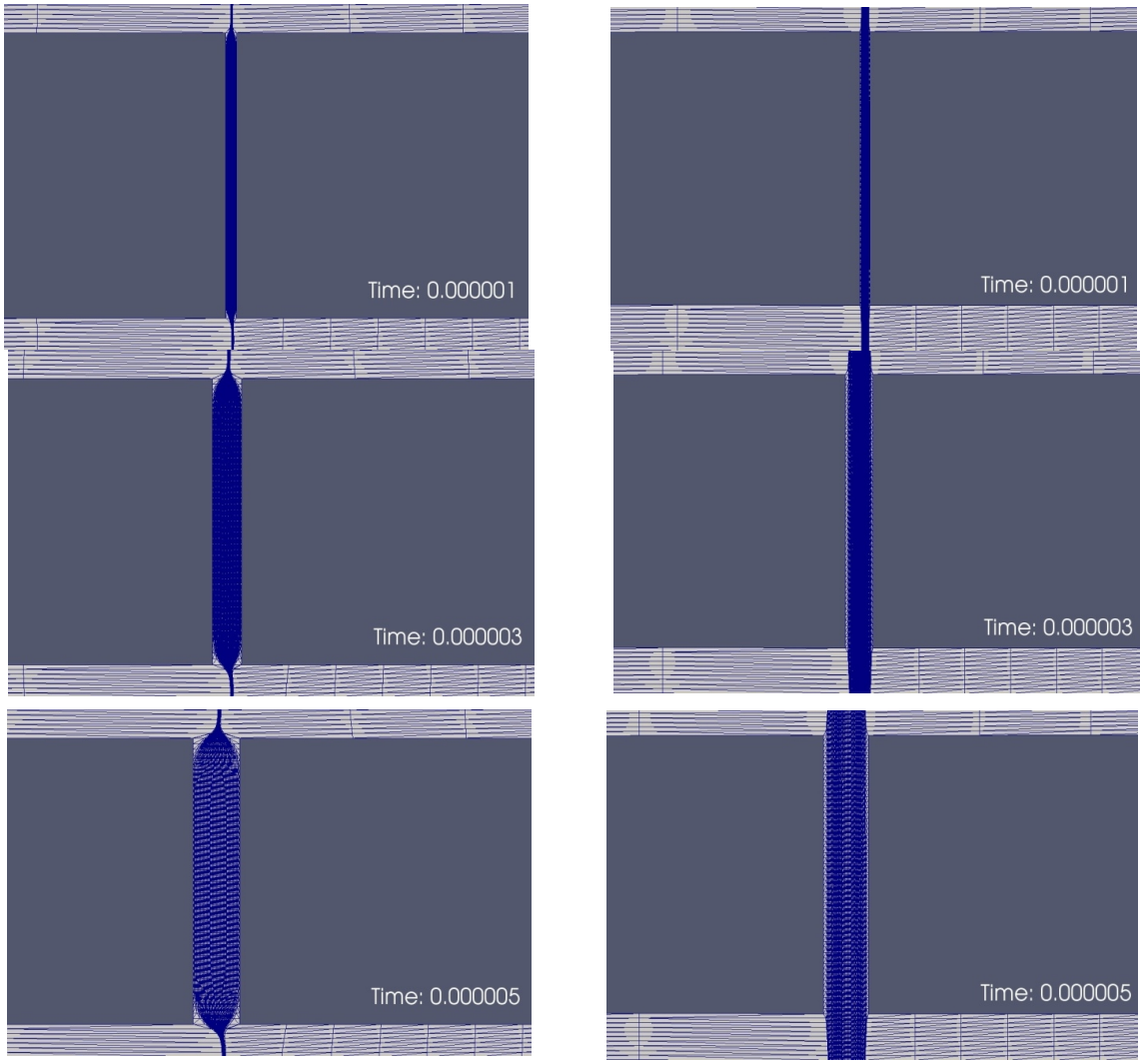

Figure 2.11. Comparison of mesh movement between different diffusivity coefficients for geometry model 1 and 2 of the diaphragm-less shock tube. a) case 1; b) case 2

Piston motion for a liquid jet injector

If there is no an appropriate class to simulate a specific subject in OpenFOAM, an original class can be developed by the user. Here, an original dynamic mesh object, *liquidJetTopoFvMesh* is explained. This class is based on a default class whose name is *movingConeTopoFvMesh* and modified specially to simulate high-speed jet generation from a needle free injector presented in Chapter 3. In this class, as the volume of the cylinder is compressed or expanded by the piston motion, a mesh layer is removed or added. The user has to specify the following parameters in *dynamicMeshDict* /*meshModifiers* before running the simulation.

- *motionVelAmplitude*: magnitude of moving wall (i.e., the piston) velocity
- *rightObstacleEdge*: the position of moving boundary, which is basically function of time during calculation
- *minThickness*/*maxThickness*: threshold values for layer addition/removal operation

High-speed liquid jet emits from a cylinder which consists of a chamber, a piston and an orifice. As the volume of the cylinder is decreasing, the mesh deformation inside cylinder is increasing. This affects the precision of the solution and computational time little by little. Therefore, cell layers are removed layer by layer by the developed class. This gives a better resolution control during the simulation since the minimum and maximum allowable cell layer thicknesses are specified. The mesh motion is firstly performed simply by the original squeezing/stretching approach until either the minimum or the maximum cell layer thicknesses reach a critical (specified) value. In this case, depending on the region and criterion, a new cell layer is added (to the expanding region) or an old

cell layer is removed (from the compressing region) and the new cell sizes are adjusted; these operations are done while the simulations continues, so that the solution will remain continuous, independent of the number or the size of the cell layers.

Here, a simple comparison between layer addition/removal (topology change) and mesh expansion/squeezing (mesh motion solver) is presented. The moving wall velocity is 10 m/s in *x*-direction, cylinder length is 10 mm at t = 0s and the simulation is stopped at t = 0.9 ms. This means the cylinder is compressed by 90% at end time of the simulation. Preset parameters for both methods are as follows:

liquidJetTopoFvMesh: minThickness = 0.15mm, *maxThickness* = 0.4mm

dynamicFvMesh (*velocityLaplacian*)*:* non-orthogonality = 1, skewness = 200 (for δ)

Figure 2.12 indicates that max non-orthogonality is increased almost linearly in motion solver but those in topology change does not change throughout the simulation. Thus, topology change method has advantages in terms of mesh quality comparing with mesh motion solver if the total volume inside computational domain compressed severely, i.e., more than 50%. The reason why the max skewness in both cases remains same is that moving wall moves only in x-direction in this sample case and the most distorted cell located at the interface between the cylinder and the orifice is not affected by only one-direction movement. Figure 2.13 visualizes the compression sequences by motion topology change. One can observe that topology change method has no-mesh movement (deformation) except for the moving boundary. It is noted that in Chapter 3, all simulations are carried out by mesh deformation method since the ratio of compression is enough small not to deteriorate mesh quality and the convergence of calculations.

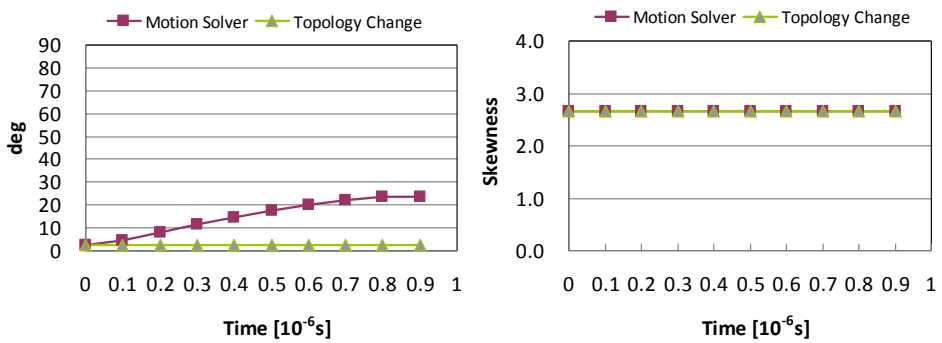

(a) Max Non-orthogonality (b) Max Skewness

Figure 2.12. Time histories of mesh qualities for the cylinder with the moving piston. a) max non-orthogonality; b) max skewness

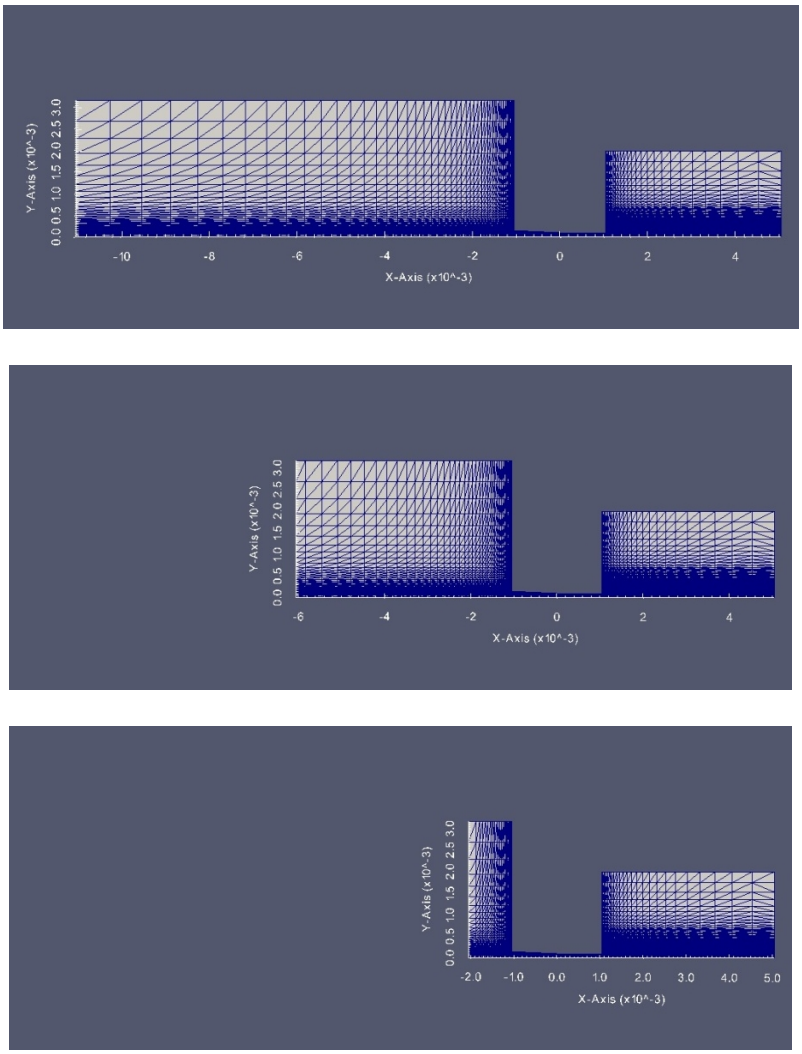

Figure 2.13. Piston motion by topology change method

Chapter 3

CFD Analysis of Needle Free Liquid Jet Injectors

3.1. General overview

A liquid jet injector is a biomedical engineering device for drug delivery, which is typically driven by a force from a power source such as spring or compressed gas. A set of cylinder and piston in the device emits a stream of fluid containing the drug through a nozzle. The fluid exits as a high-speed small diameter liquid jet of sufficient pressure penetrating the skin and delivering the appropriate amount of medication. In this Chapter, CFD simulation is carried out to investigate the fluid mechanics and performance of the needle free injector powered by an air source. A combined numerical approach using moving boundary method as introduced in Chapter 2 and multiphase LES/VOF techniques is used to simulate the fluid dynamics of the jet through the orifice generated by the motion of the plunger.

3.2. Problem description

Drug delivery using conventional hypodermic needles has long remained one of the only means available to healthcare professionals to effectively administer a broad range of medication. Nevertheless, this traditional practice is accompanied by many

disadvantages; vaccination by a needle-syringe is troublesome for many children since it accompanies pain, scare and causes additional stress. In insulin delivery, traditional injections using needle-syringes is often a burden especially for beginners and children. In animal-production industries, there is also a need for improvement in vaccines and their delivery system in terms of cost, safety compliance as well as minimizing animal stress. To address the above issues, needle-free jet injections have long been considered as an alternate technique to effectively deliver medication to the different layers of skin for humans and animals other than traditional drug delivery using hypodermic needles (Mitragotri, 2005, 2006). The liquid jet injector delivers medication by a force generated from a power source which is imparted on a cylinder and forces a column of fluid containing the drug through a nozzle. The liquid exits as a high-speed small diameter liquid jet of sufficient pressure penetrating the skin and delivering the appropriate amount of medication. Typical design of needle-free injectors generally produces jet exit velocities greater than 100 m/s and diameters ranging from 100 to 360 μm with an initial pressure change of 27.5 MPa within 0.5 ms (Mitragotri, 2005; Kendall, 2010). The volume of injection ranges from 0.1 to 1 ml with a skin penetration depth of up to 10 mm. Figure 3.1 illustrates the process of liquid jet injection into a ballistic gel and to air from a custom-built air-powered needle-free injector prototype (Portaro & Ng, 2013).

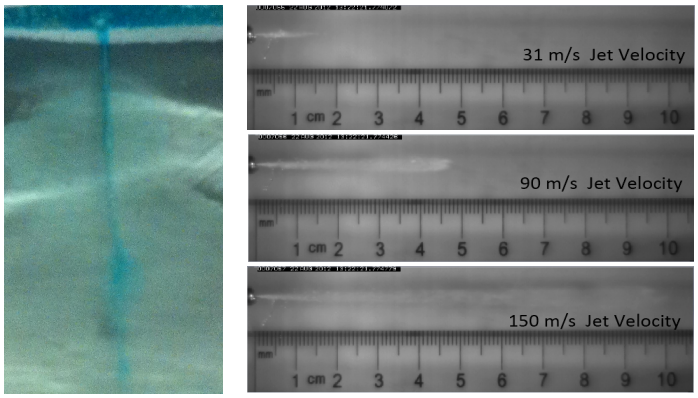

(a) **(b)**

Figure 3.1. Photographs showing a) the jet penetration into a ballistic gel; and b) the liquid jet exiting the injector nozzle (Portaro & Ng, 2013).

In order to alleviate the problems with the early use of liquid jet injectors such as pain, bruising, hematomas, incomplete delivery of medication, excessive penetration and cross contamination (Hingson et al., 1963; Wijsmuller & Snider, 1975; Schneider et al., 1994), much research has been conducted on improving their performance by analyzing the fluid mechanics of jet injection. A number of research papers, notably by Schramm & Mitragotri (2002), Schramm-Baxter & Mitragotri (2004), Schramm-Baxter et al. (2004), etc., performed detailed experiments and reported the dependence of fluid jet penetration into human skin on different injector parameters. Furthermore, the development of simple analytical models to simulate the skin fracture and medicine delivery, as well as to predict the jet pressure and velocity distribution are also emerging and serve to compliment experimental studies (e.g., Baker & Sanders, 1999; Shergold et al. 2006; Chen et al. 2010).

Although there exists a number of different types of needle-free liquid jet injectors that can be classified by their power source such as, spring-loaded devices (Schramm-Baxter & Mitragotri 2004), Lorenz-force actuators (Taberner et al., 2006, 2012; Hemond

et al. 2006) and piezoelectric actuators (Stachowiak et al. 2007), this study focuses on the development and analysis of air-powered liquid jet injectors using Computational Fluid Dynamics (CFD). Studies demonstrate that the majority of commercially available injectors are gas/air powered units (Mohanty et al. 2011), however there is no indication of an engineering model that prescribes the performance characteristics of this particular type of injector. The main goal of this work is therefore to create and validate a numerical CFD model which can accurately capture the fluid dynamic behavior of the high speed jet emanating from an air-powered needle-free injector. This Chapter reports its validity by comparing the numerical results with experimental measurement obtained using a prototype injector with identical geometry. The experimental prototype functions in a very similar fashion and produces jets of similar geometry and velocities as the vast majority of commercially available units. A parametric study using the developed numerical model is also carried out to analyze the influence of various injector parameters such as driver pressure, injection chamber length and volume as well as nozzle sizes, on the jet injection process.

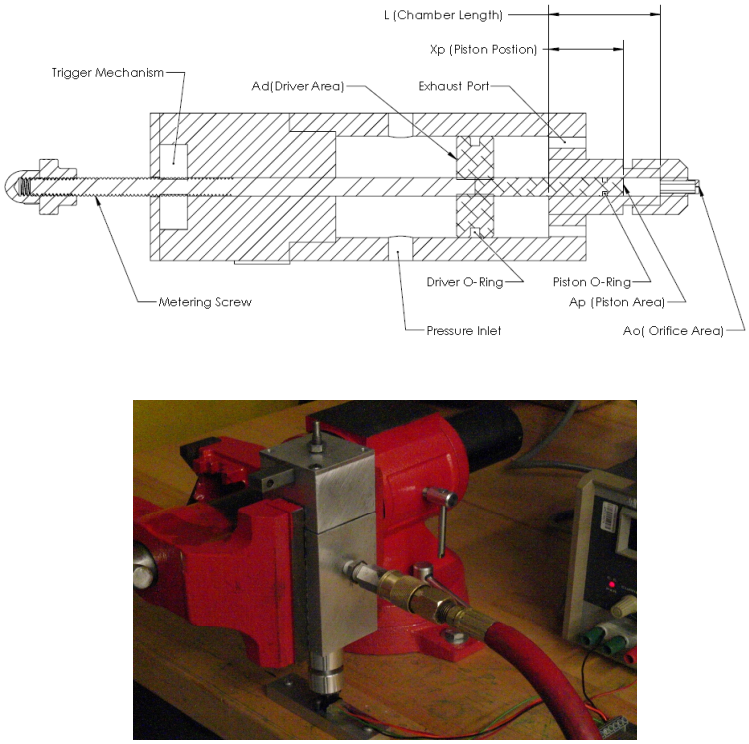

Figure 3.2. A photograph showing the experimental prototype of an air-powered needle-free injector (Portaro & Ng, 2013).

3.3. Numerical model

In this study, CFD is applied to the analysis of needless jet injectors. The research mainly addresses the fluid dynamics of the high speed jet emanating from an air-powered needle-free injector and analyzes the effect of injector parameters on the jet injection process. Numerical simulations of the high-speed liquid jet generation process from the needle-free injector are carried out using the OpenFOAM® CFD software package (OpenCFD, 2013). The geometrical model is equivalent to a custom-built experimental prototype (Portaro & Ng, 2013) as shown in Fig. 3.2, which consists of a driver part containing high-pressure gas, a moving piston with O-rings, a chamber containing the

liquid and an orifice-type nozzle. High-speed jets are emitted into the air through the orifice. Some important dimensions and operating characteristics of the experimental prototype injector are summarized in **Table 3.1**.

Injector Parameters	
Nozzle Diameter	100 μm - 260 μm
Driver Pressure	3 Bar - 10 Bar
Injection Volume	0 ml - 1.2 ml
Piston Diameter	6.35 mm
Driver Diameter	38.1 mm
M_p (Mass of Piston-Driver Assembly)	80 g

Table 3.1. Key dimensions and operating characteristics of the injector

The chamber, the orifice and the atmospheric region are modeled in this simulation study as an axi-symmetric geometry as shown in Fig. 3.3. The piston is modeled as a two-dimensional moving wall located at the left hand boundary. Physical dimensions and average gird size for each domain are summarized in Table 3.2. It is noted that average cell size given in the table is for the base mesh case and the grid is in fact refined near the orifice inlet/exit to capture steep gradient of pressure, velocity and volume fraction of liquid. The structured mesh is generated by a built-in utility in OpenFOAM. The domain boundaries have zero gradient Neumann conditions for the liquid volume fraction, the sub grid scale (SGS) stress, pressure and temperature; and non-slip condition on velocity. Dirichlet condition is applied for the SGS turbulent energy and a fixed total pressure (i.e., 101,325Pa) is imposed on the atmosphere exit boundaries.

Domain Name	Radius (y- coordinate)		Length (x- coordinate)	
	Dimension	Average Cell Size	Dimension	Average Cell Size
Chamber	3.175	0.064	10	0.20
Orifice	0.1	0.01	2.1	0.04
Atmosphere	2	0.033	4	0.16

Table 3.2. Physical dimensions of the computational domain and the base mesh size (unit: mm).

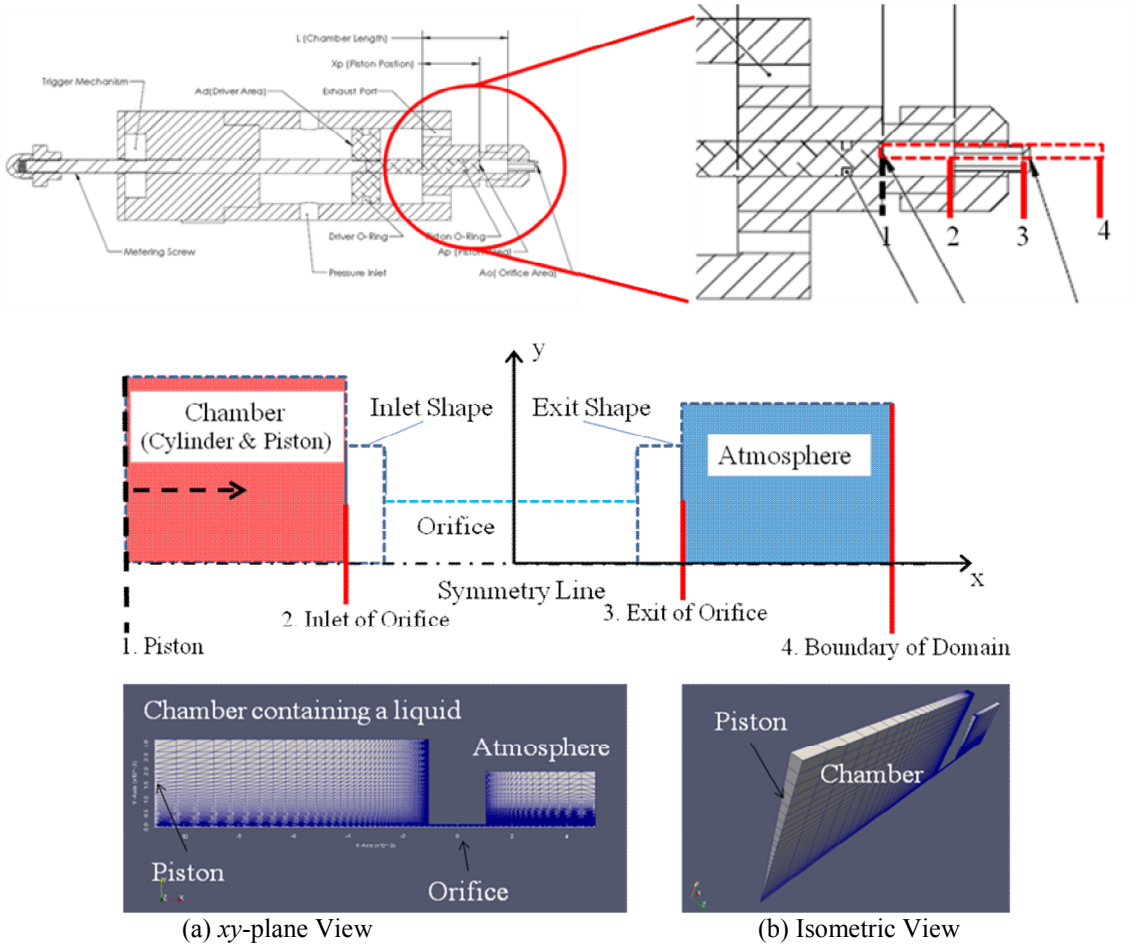

(a) xy-plane View (b) Isometric View

Figure 3.3. The layout of the computational domain

In order to physically model the injection process, the liquid retained in the injector chamber is initially impacted abruptly by the moving grid boundary to mimic the injector piston which is driven by the driver air pressure. Consequently as a result of injector

piston impacting the fluid a high speed liquid jet is emitted to atmospheric region through a nozzle. The moving boundary position/velocity is obtained by solving an ordinary differential equation obtained from a force balance (Newton's 2nd law) at each computational time step. For the numerical modeling of the piston motion, the following assumptions are introduced:

- The piston is a solid body (no-deformation occurs) and its mass is constant;
- The thickness of the piston is neglected (assumed as 2-dimentional object);
- Back leakage of liquid through the gap between the O-ring and the inner surface of the cylinder is neglected;
- Gravitational force is neglected.

During the injection process, the piston is pushed by the high-pressure gas contained in the driver part and impacts the liquid inside the chamber. However, the liquid plays a role as a damper and hence, the backward force by the liquid is generated as the fluid is being compressed. Furthermore, the friction force between O-rings and the inner surface of the cylinder should be taken into consideration during the motion. As a result, the piston motion is determined as summation of the driver force by the gas pressure inside the driver part, the damping force by the fluid inside the chamber and the friction force (Chen et al., 2011; Portaro & Ng, 2013).

$$\frac{d^2 x_p}{dt^2} = \frac{F_D(t)}{m_p} - \frac{A_p p(t)}{m_p} - \frac{F_f(t)}{m_p} \tag{3.1}$$

where F_D and F_f are the driving force and frictional force, and $p(t)$ is the fluid pressure on the piston boundary and A_p and m_p are the piston surface area and mass, respectively. For an air-powered injection system, the driving force F_D which moves the plunger forward is

produced by pressurizing the driver chamber. The pressure within the chamber can be modeled by using the ideal gas law. After the chamber is pressurized to a known pressure, the mass within the chamber can be computed. Once the initial mass of air within the chamber is known, then the pressure within the chamber can be computed as a function of driver displacement, i.e.:

$$p_d = \frac{mRT}{V_D(t)} \tag{3.2}$$

with

$$V_D(t) = \left(L_o + x_p(t)\right)A_D \tag{3.3}$$

As the driving force begins to move the piston forward, there is resistance created by both atmospheric pressures p_a acting on the opposite side of the driver face. This force can be assumed to remain constant throughout the injection process and is simply the product of atmospheric pressure and the driver area. This gives:

$$F_D(t) = A_D\left(\frac{mRT}{V_D(t)} - p_a\right) \tag{3.4}$$

The frictional forces within the mechanism serve to counteract and damp the movement of the driver/piston assembly. The friction is caused by the O-ring seals which make contact and rub against the inner walls of both the driver chamber and the injection chamber. In order to model the O-ring friction it must be broken down into two components, the first consists of the friction force caused by the compression fit of the O-ring into its housing, the second is a result of the thin fluid film which is generated in the clearance gap between the two components that the O-ring must seal. The forces caused by the compression of the O-ring, in the barrel of the injector is also dependent on the

force generated by the pressure of the fluid. Consequently, the two major forces causing O-ring friction must be coupled in order to accurately model friction. Using the concepts from tribology (Chen 2011; Portaro & Ng, 2013), the fluid pressure imposed on the O-ring can be approximated by applying the Reynolds equations.

$$\overline{p}_{O-ring} \approx \frac{1}{2}\frac{6\mu U(t)}{h^2}\frac{d}{2} + p(t) \tag{3.5}$$

As a result of knowing the pressure imposed by the fluid on the O-ring seal the resisting force caused by this pressure is simply the area of exposed O-ring multiplied by the corresponding pressure, i.e.,

$$F_{fluid} = \overline{p}_{O-ring}\pi Dh \tag{3.6}$$

The amount of compression fit κ as a function of load that an O-ring will produce can be found from empirical charts (Darcoid Norcal Seals). In addition to the force caused by the compression of the O-ring into the barrel of the injector, it is also necessary to take into consideration the transfer of forces caused by the fluid pressure on the O-ring. The fluid pressure that acts on the seal also serves to further increase the compression loading. Studies conducted by Guang & Wang (1994) demonstrate that the transfer coefficient between the fluid pressure acting on a seal in relation to the increase of compression force of the O-ring can be estimated at 1. In other words, the pressure contained within the thin film acting on the seal almost entirely serves to increase the amount of compression forces on the sealing surfaces. Knowing that the coefficient of friction between aluminum and nitrile rubber is $\alpha = 0.2$ (Chen et al. 2011; Portaro & Ng, 2013), the resisting force encountered by individual O-ring seals in the injector can be

completely described through Eq. 3.7:

$$F_f(t)_{O-ring} = \left(\alpha \cdot \bar{p}_{O-ring}(t)\pi Db\right) + \left(\bar{p}_{O-ring}(t)\pi Dh\right) + \alpha \cdot \kappa \qquad (3.7)$$

During the computation, the piston position/velocity as a function of time can therefore be obtained by solving the ordinary equation, i.e., Eq. (3.1) together with Eq. (3.2) to Eq. (3.7). The new velocity and position of the piston are determined by integrating the acceleration $\ddot{X}_p(t)$ at the present time step.

$$\dot{X}_p(t) = \dot{X}_p(t - \Delta t) + \ddot{X}_p(t)\Delta t \qquad (3.8)$$

$$X_p(t) = X_p(t - \Delta t) + \dot{X}_p(t)\Delta t \qquad (3.9)$$

These equations govern the equation of motion of the piston and are incorporated into a class in OpenFOAM. Figure 3.4 illustrates the behavior of the piston from sample simulations showing the maximum piston velocity occurring at the very beginning before the frictional forces and fluid forces can damp the motion. Using the piston position/velocity as boundary conditions, a Laplace equation related to the mesh motion as illustrated in Fig. 3.5 is solved to determine new mesh using the dynamic mesh classes in OpenFOAM (see Chapter 2), i.e.,

$$\nabla \cdot \left(\delta \nabla u_m\right) = 0 \qquad (3.10)$$

where δ is constant or variable diffusivity and u_m is mesh motion velocity or mesh point displacement. As a result of introducing these classes, the piston motion is a part of CFD solution in this study.

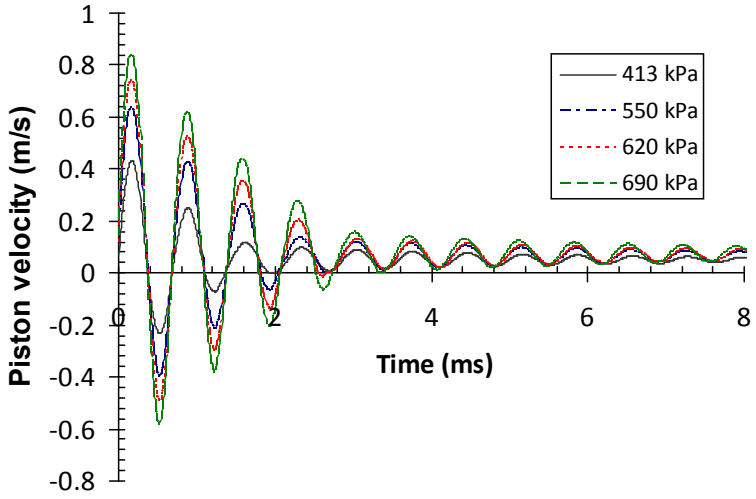

Figure 3.4. Simulation of the driver piston velocity for four different driver pressures

Phase	**Kinematic Viscosity** $\upsilon[m^2/s]$	**Density** ρ [kg/m^3]	**Compressibility** $\psi[s^2/m^2]$	**Volumetric Heat Capacity** $c_v[J/m^3K]$	**Thermal Conductivity** k [W/mK]	**Gas Constant** $[m^2/s^2K]$
Liquid: Water	8.714×10^{-7}	9.97×10^{2}	4.44×10^{-7}	4.18×10^{3}	6.13×10^{-1}	(3×10^{3})
Gas: Air	1.557×10^{-5}	1.19	1.16×10^{-5}	7.21×10^{2}	2.62×10^{-2}	2.87×10^{2}

Table 3.3. Physical Properties for 2 phases at room temperature

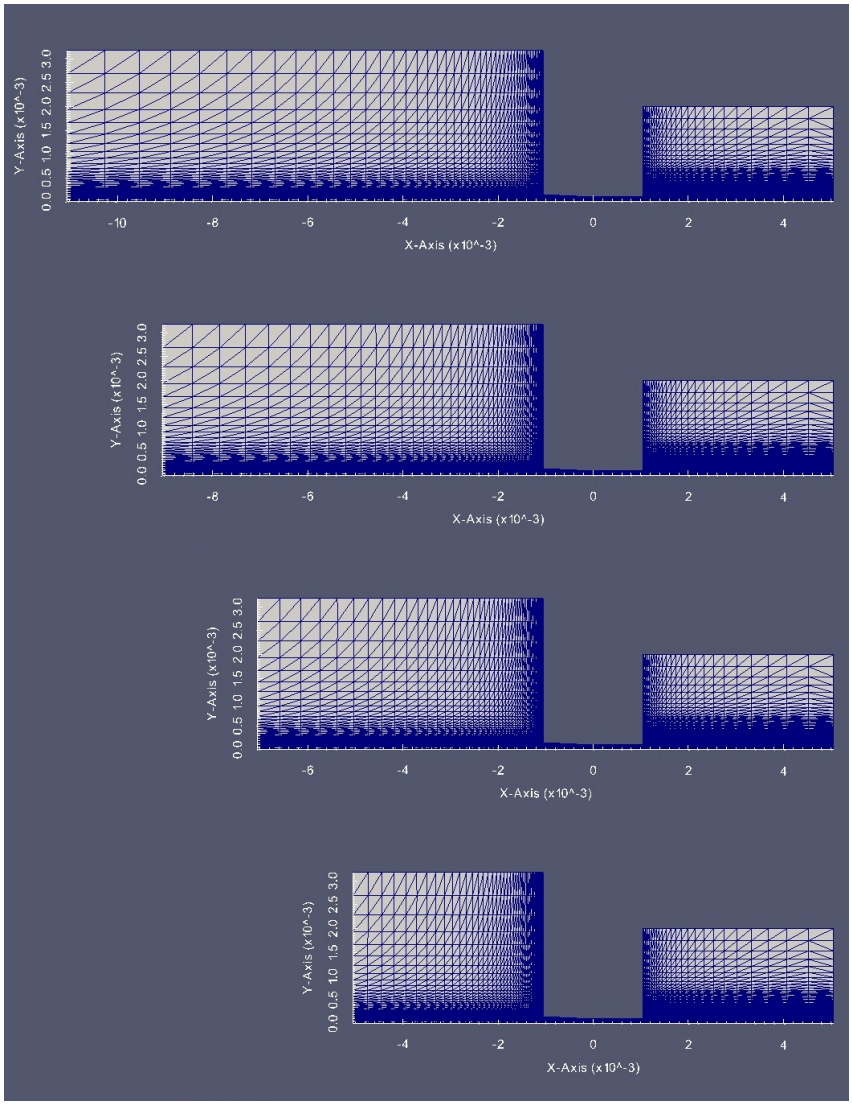

Figure 3.5. An example showing the 1-D piston motion and the dynamic mesh

For the fluid properties, the two fluid phases are initially divided into a liquid phase in the chamber/orifice and a gas phase in the atmosphere region. The physical properties for water and air are listed in Table 3.3 and Surface tension for water is 0.072 [N/m]. The gas density is simply specified by using the ideal gas formula for the air to cope with the compressible flow field. In the chamber/orifice, it is however more complicated to specify the water as a compressible liquid. In this study, variable density is specified with

compressibility, in other words, the bulk of modulus to water. In Eq. (3.11), the variables p and ρ are the liquid pressure and density, respectively. The compressibility ψ and the bulk modulus of elasticity of the liquid B are a function of pressure and temperature. These are updated after solving the energy equation (Eq. 3.12) at each time step. Then, the density is updated in the linearized equation (Eq. 3.13) during the simulation. Subscripts 0 and 1 denote the respective quantity at the initial and current time.

$$\frac{\partial \rho}{\partial p} = \frac{\rho}{B} = \psi \tag{3.11}$$

$$\frac{\partial(\rho T)}{\partial t} + \nabla \cdot (\rho U T) - \nabla \cdot \left(\frac{k}{C_v} \right) \nabla T = \frac{p}{C_v} \nabla \cdot U \tag{3.12}$$

$$\rho_1 \approx \rho_0 + \psi (p_1 - p_0) \tag{3.13}$$

The Volume-of-Fluid (VOF) method is then used to update the position of the interface between two phases by computing the transport equation for the liquid volume fraction as the indicator function to locate the interface.

$$\frac{\partial(\rho \alpha)}{\partial t} + \nabla \cdot (\rho U \alpha) = 0 \tag{3.14}$$

with the liquid-phase volume fraction α,

$$\alpha = \begin{cases} 0 & \textit{for a cell inside the gas} \\ 0 < \alpha < 1 & \textit{for a cell in the transitional region} \\ 1 & \textit{for a cell contained completely the liquid} \end{cases}$$

By determining the volume of fraction α, the local properties of fluid are computed based on the single state of each phase, i.e., the local density ρ and the local viscosity μ of the fluid are interpolated across the interface as follows:

$$\rho = \alpha\rho_l + (1-\alpha)\rho_g$$
$$\mu = \alpha\mu_l + (1-\alpha)\mu_g \tag{3.15}$$

where the subscripts *l* and *g* denote the liquid- and gas-phases, respectively.

The governing equations of the phenomenon consist of the transport equations for conservation of mass and momentum of a two-phase flow system, comprised of two immiscible, compressible Newtonian fluids, including surface tension (OpenCFD, 2013). The single set of conservation equations that simultaneously describe the flow the two-phase mixture are:

$$\frac{\partial\rho}{\partial t} + \nabla\cdot(\rho U) = 0 \tag{3.16}$$

$$\frac{\partial(\rho U)}{\partial t} + \nabla\cdot(\rho UU) = -\nabla p + \nabla\cdot\tau + F_{sv} \tag{3.17}$$

The stress balance of dynamics is realized by introducing a body force F_{sv} in the last term on the right hand of Eq. (3.17). F_{sv} represents the surface tension concentrated at the interface. The localized body force F_{sv} near the interface is calculated from the volume fraction data and is given by

$$F_{sv} = \int_{S(t)} \sigma\kappa' n' \delta(x - x')dS \tag{3.18}$$

where p is the pressure, ρ the density, U the velocity, τ the stress tensor and σ the surface tension coefficient. n represents the unit vector normal to the liquid surface $S(t)$ and $\kappa = \nabla\cdot\hat{n}\left(\hat{n} = \frac{n}{|n|}\right)$ is the curvature of the liquid surface. Eq. (3.18) acts only at the interface between two phases (indicated by the Dirac function, $\delta(x)$) over the entire liquid

surface, $S(t)$. F_{sv} in Eq. (3.17) removes the explicit boundary condition at the interface in the governing equations.

As a turbulence model, Large Eddy Simulation (LES) is applied. To capture dynamic water jet phenomena more precisely, LES model is more appropriate than Reynolds Averaged NS equation (RANS) model. In the unsteady flow solution, the time step size Δt is $10^{-2} \sim 10^{-3}$ μs is selected to obtain stable solutions. The LES-VOF equations are derived from Eq. (3.17) through a localized volume averaging of the phase weighted properties. This is more commonly known as filtering process because it removes the very small scales of motion from direct calculation. This averaging in conjunction with the non-linear convection term in Eq. (3.14) produces an additional quantity into the momentum equation that cannot be directly calculated. The effect of the subgrid scales on the resolved eddies in momentum Eq. (3.17) is presented by the subgrid scale (SGS) stress. It represents the effect of the unresolved small scales of turbulence; it is given by

$$\tau_{SGS} = \overline{UU} - \overline{U}\,\overline{U} \tag{3.19}$$

The SGS stress is approximated through a single subgrid scale model of the eddy viscosity type as:

$$\tau_{SGS} - \frac{2}{3}kI = -\frac{\mu_{SGS}}{\rho}\left(\nabla\overline{U} + \nabla\overline{U^T}\right) \tag{3.20}$$

where k is the subgrid scale turbulent energy and μ_{SGS} is the subgrid scale viscosity, both of which are calculated from the one-equation SGS turbulent energy transport model:

$$\frac{\partial k}{\partial t} + \nabla\cdot\left(k\overline{U}\right) = \nabla\cdot\left[\left(\nu + \nu_{SGS}\right)\nabla k + \tau_{SGS}\cdot\overline{U}\right] - \varepsilon - \frac{1}{2}\tau_{SGS} : \left(\nabla\overline{U} + \nabla\overline{U^T}\right) \tag{3.21}$$

with:

$$\varepsilon = \frac{C_\varepsilon k^{\frac{3}{2}}}{\Delta}$$
$$v_{SGS} = \frac{C_\varepsilon k^{\frac{1}{2}}}{\Delta} \qquad (3.22)$$
$$\Delta = \left(\Delta_x \Delta_y \Delta_z\right)^{\frac{1}{3}}$$

where ε is the SGS turbulent dissipation and Δ is the SGS length scale corresponding to the filter width (in most cases equivalent to the cell size). Δ_x, Δ_y, Δ_z are the grid spacings in the *x*, *y* and *z* directions, respectively. The constants in Eqs. (3.22) are $C_\varepsilon = 1.048$ and $C_k = 0.094$ from statistical considerations. Additional ‘‘subgrid’’ terms are produced by the filtering of the integral in Eq. (3.17) and the convection term in Eq. (3.14). The former represents the subgrid-scale influence of surface tension, known as the capillary force. It becomes more important relative to the resolved surface tension when the surface curvature approaches the grid size. In cases where the influence of surface tension is small compared to that of inertia, the effect of subgrid-scale surface tension also becomes small. The latter term represents deformation of the liquid-gas interface due to subgrid-scale turbulence and is experienced at the grid scale as an added inter-phase diffusion. This effect is in direct opposition to the estimated SGS surface tension force. Numerical effort has been made to preserve the sharpness of the gas-liquid interface. Both these SGS terms, which can be potentially used to construct a new model for closure, have not been developed to date. In high-speed liquid jet simulation, the influence of surface tension is relatively small compared with the effect of inertia at the resolved scales. The relatively fine mesh spacing (which minimizes SGS contributions) and the effect of grid-scale deformation of the liquid-gas interface tend to oppose one another.

3.4 Numerical schemes and algorithm

The Finite volume scheme in OpenFOAM is built on Gaussian integration with linear flux interpolation. To limit numerical artifacts while discretizing some divergence form such as the convective term, bounded second order TVD (Total Variation Diminishing) schemes with either linear limiter or vanleer limiter were chosen (Ferziger & Peric 1999). For multi-phase solvers, the multidimensional universal limiter for explicit solution (MULES) method is applied in OpenFOAM to enchance boundedness of the phase fraction independent of underlying numerical scheme, mesh structure, etc. For other terms such as the first time derivative uses the first order implicit Euler scheme (OpenCFD, 2013).

The solver used in to compute the solutions of the discretizing equations follows the PISO-SIMPLE (PIMPLE) algorithm (Barton, 1998; Ferziger & Peric 1999). The SIMPLE algorithm calculates pressure on a staggered grid from velocity components by applying an iterative procedure coupled with the Navier-Stokes equations. Meanwhile, the PIMPLE algorithm combines the SIMPLE algorithm and pressure implicit with splitting the operators (PISO) algorithm to rectify the second pressure correction and correct both velocities and pressure explicitly. In the unsteady flow solution, the time step size Δt of $1 \times 10^{-8} \sim 5 \times 10^{-9}$ sec is selected to obtain stable solutions. In OpenFOAM, the combination of *compressibleInterFoam* and *oneEgEddy* realizes the above models as multi-phase Navier–Stokes solver and LES model respectively. Figure 3.6 illustrates the flowchart of the numerical procedure to carry out the simulation.

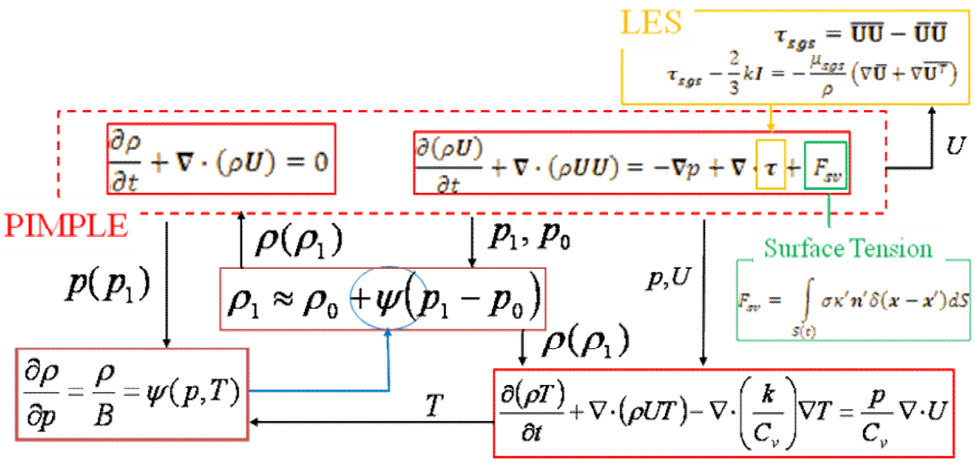

Figure 3.6. Flow chart of solving set of governing equations

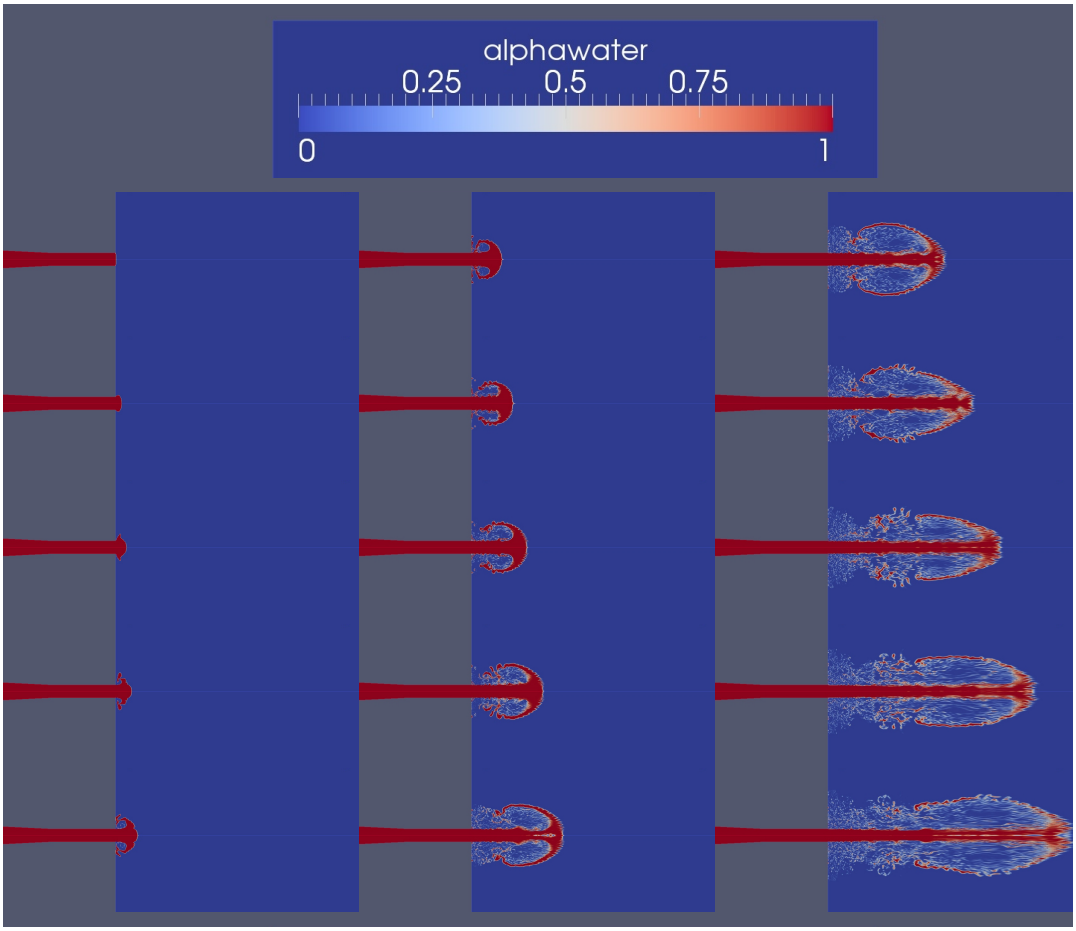

Figure 3.7. CFD results showing the time evolution of the jet emitted from the 200 μm injector nozzle and driven by a 413 kPa driver pressure.

3.5. Results and discussions

The dynamic characteristics of the high-speed liquid jet emitted from the injector nozzle can be illustrated qualitatively first by the phase fraction plots shown in Fig. 3.7. In this figure, the liquid jet structure is computed with a fine mesh (i.e., with the smallest level Δx = 0.01 mm and Δr = 2.5x10^{-4} mm) to reveal detailed features of the liquid jet. These images from CFD provide a clear depiction of jet roll-up during the initial start-up of the injection process. As the jet emerges from the nozzle the re-circulation on the corner causes a blunt shape of the leading front of the jet. The CFD solution also demonstrates that part of the jet starts to atomize generating a spray. In practice, the initial enlargement of the jet front causes pain and bruising. Nevertheless, it is possible to conclude that at initial stages the overall jet divergence is minimal. The diameter of the jet is relatively close to the nozzle diameter during the continuous injection process.

For a quantitative assessment of the numerical model, it is possible to extract some key variables from the simulations and compare with available experimental measurement. Among different injection performance indicators the stagnation pressure is one of the fundamental measurements as it is the key parameter which determines the force at which the liquid jet will penetrate the skin and deliver a successful injection (Chen et al. 2011). To validate the numerical solutions, the computed stagnation jet pressures are compared with experimental results. It is worth noting that experimental stagnation pressures were measured using a force transducer Honeywell (Model FSG15N1A). The stagnation pressure is subsequently computed with the force readings obtained by simply dividing them by the area of the jet, which is assumed to be equivalent to the nozzle size. Comparison is first made for an injector with a 200 micron

nozzle driven at 413 kPa and results are shown exemplarily in Fig. 3.8. In general, the CFD simulation demonstrates a similar behavior as that observed from the experiment. A pressure peak first occurs within the first millisecond and the pressure then oscillates about a mean injection pressure. This peak is often believed to be responsible for the formation of a fracture in the skin and the subsequent average delivery pressure determines the depth at which the medication is delivered (Arora et al. 2007). The magnitude of the peak pressure and average pressure obtained from CFD and experimental measurement also agree well with each other within the experimental limitation. A possible explanation for the discrepancy stems from the degree of accuracy and sensitivity of the force transducer and the correct estimate of the jet area/location for the conversion to stagnation pressure. In fact, for the sensitivity of the probe a variation of 2 MPa represents approximately a force variation of 0.0264 N (2.693 g). The transducers range varies from 0 - 1500 g. Hence, a difference of 2 MPa would correspond to 0.18% of the transducers range, as a result the slight difference between CFD and experiments can be attributed to the inaccuracies of the force transducer. It is worth noting that if the computed stagnation pressure at the centerline is used for comparison instead of the space-averaged value from CFD data, a much better result can be obtained as shown in Fig. 3.9. Furthermore, the rise time to peak pressure and subsequent stabilization to the average pressure occur very rapidly. On the modeling side, the limitation of the O-ring friction model is another possible source for discrepancy relating to the greater divergence from the CFD solution of peak pressure, as O-ring friction is difficult to model because of its variability with pressure.

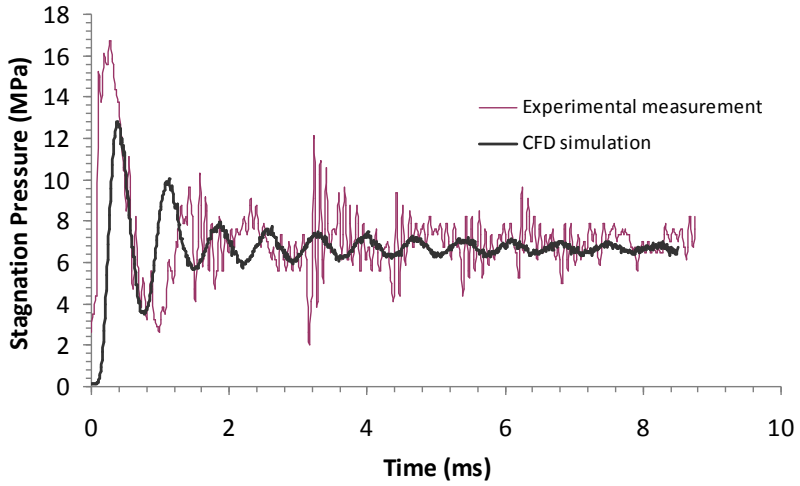

Figure 3.8. The time evolution of stagnation pressure from the CFD simulation (space averaged value) and experimental measurement for 200 μm nozzle at 413 kPa driver pressure.

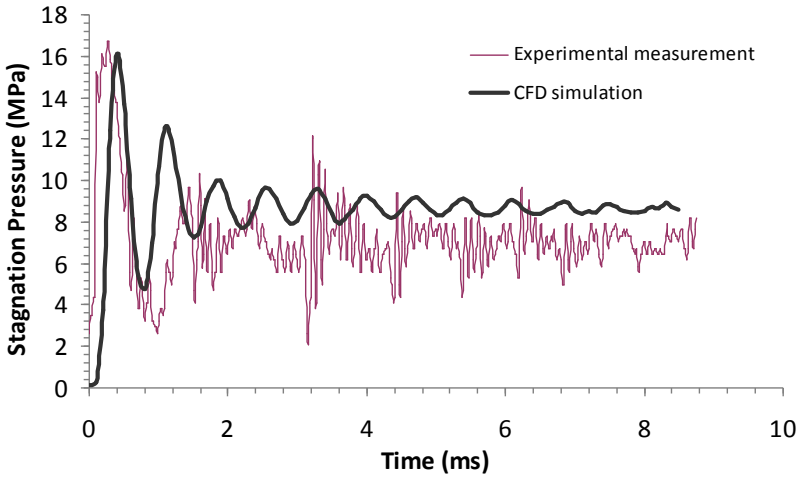

Figure 3.9. The time evolution of stagnation pressure from the CFD simulation (centerline value) and experimental measurement for 200 μm nozzle at 413 kPa driver pressure.

However to verify the difference is not due to the numerical grid resolution, a mesh dependency test is performed and the results are shown in Fig. 3.10. It confirms that the (base) mesh size used in Fig. 3.8 and Fig. 3.9 is sufficient for convergence of both the computed peak and average stagnation pressures. Taking all these influences into account, the numerical CFD model is valid in predicting performance of the injector in

terms of the peak and average stagnation pressures, given the injector geometry and driver pressure.

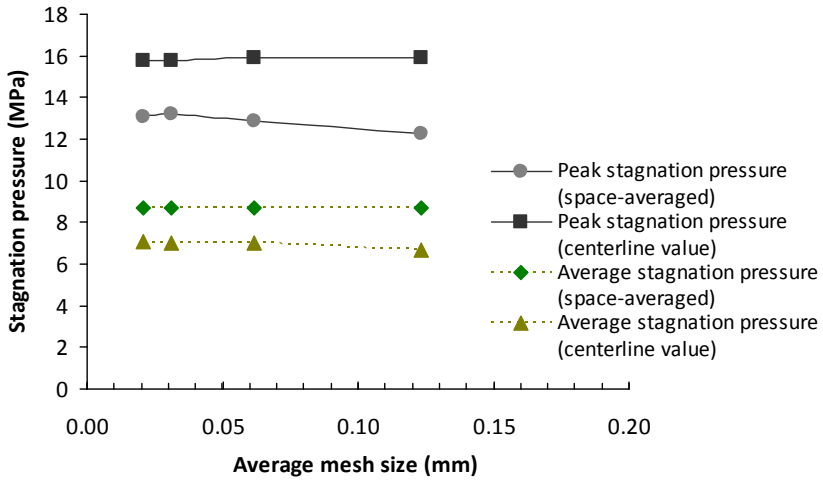

Figure 3.10. Resolution test showing the mesh dependency of the computed stagnation pressures

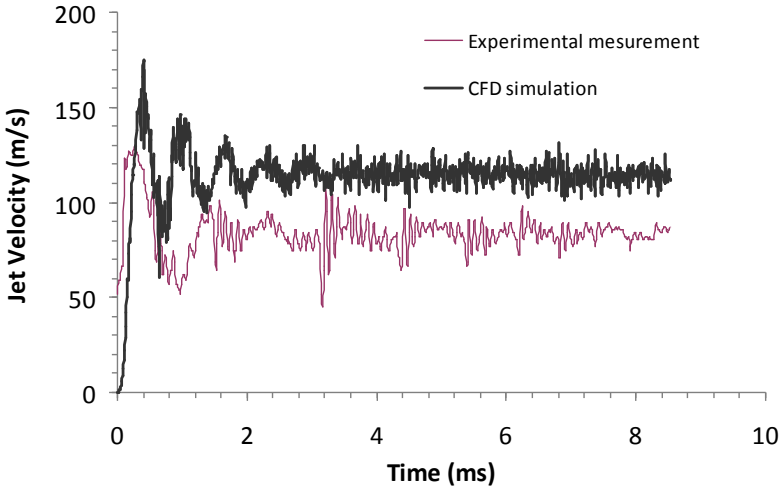

Figure 3.11. The time evolution of jet velocity from the CFD simulation (space averaged value) and experimental measurement for 200 µm nozzle at 413 kPa driver pressure.

The numerical result of space-averaged velocity from CFD is also shown in Fig. 3.11. It can be observed that the peak velocity obtained from the CFD simulation also corresponds well with the 150 - 200 m/s range described in literature. For comparison,

the jet velocity as the jet exits the orifices, converted from the experimentally measured stagnation pressure using the Bernoulli equation, is also shown in the plot and a good agreement can also be seen.

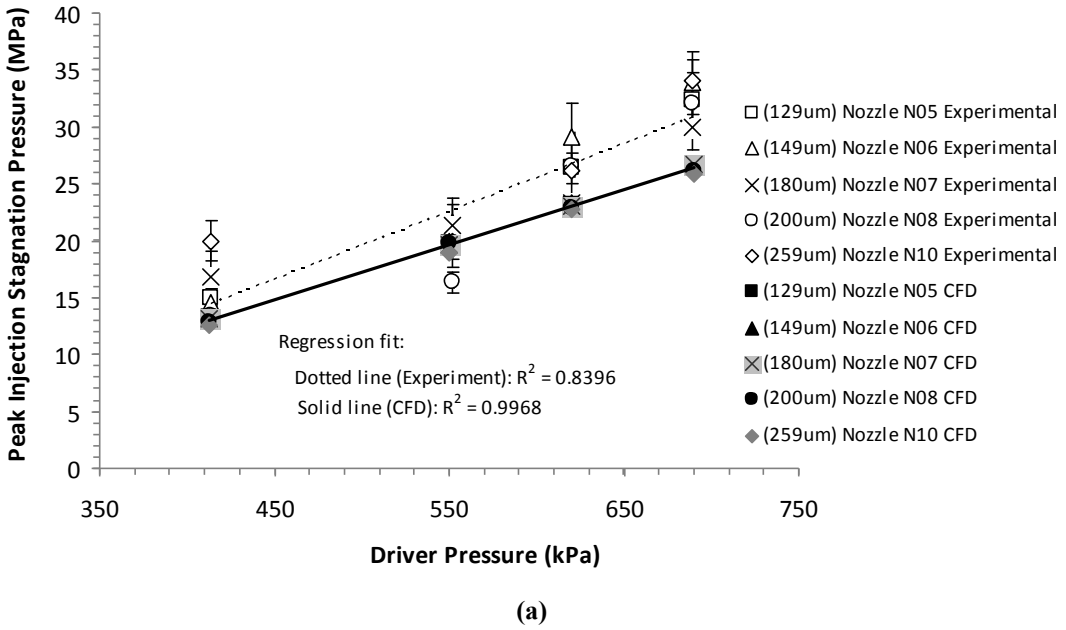

(a)

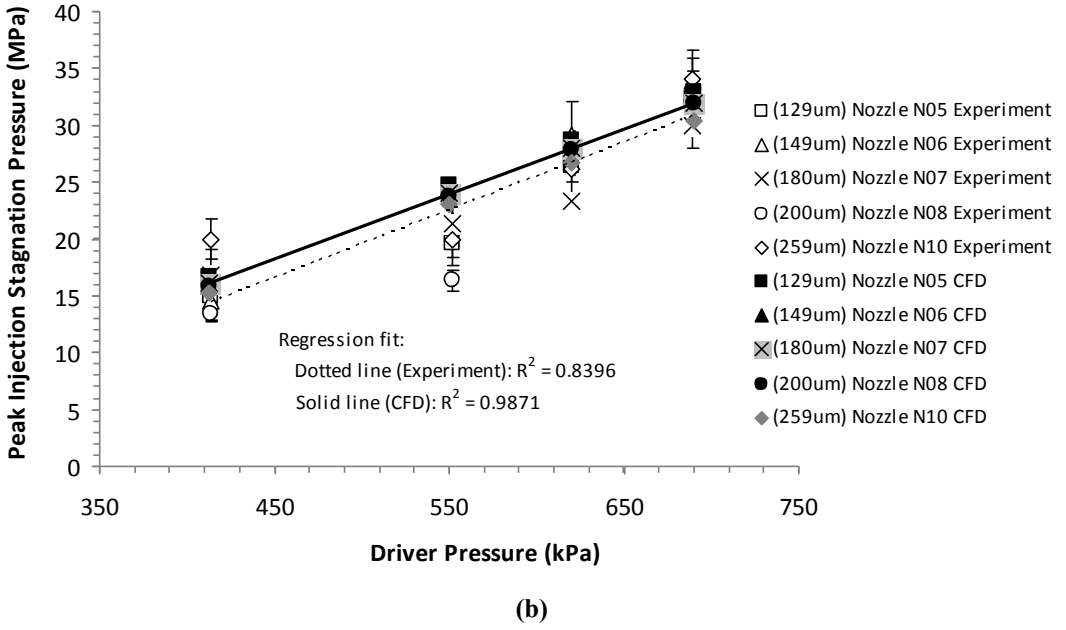

(b)

Figure 3.12. Peak stagnation pressure as a function driver pressure. a) space-averaged CFD value; and b) centerline CFD value.

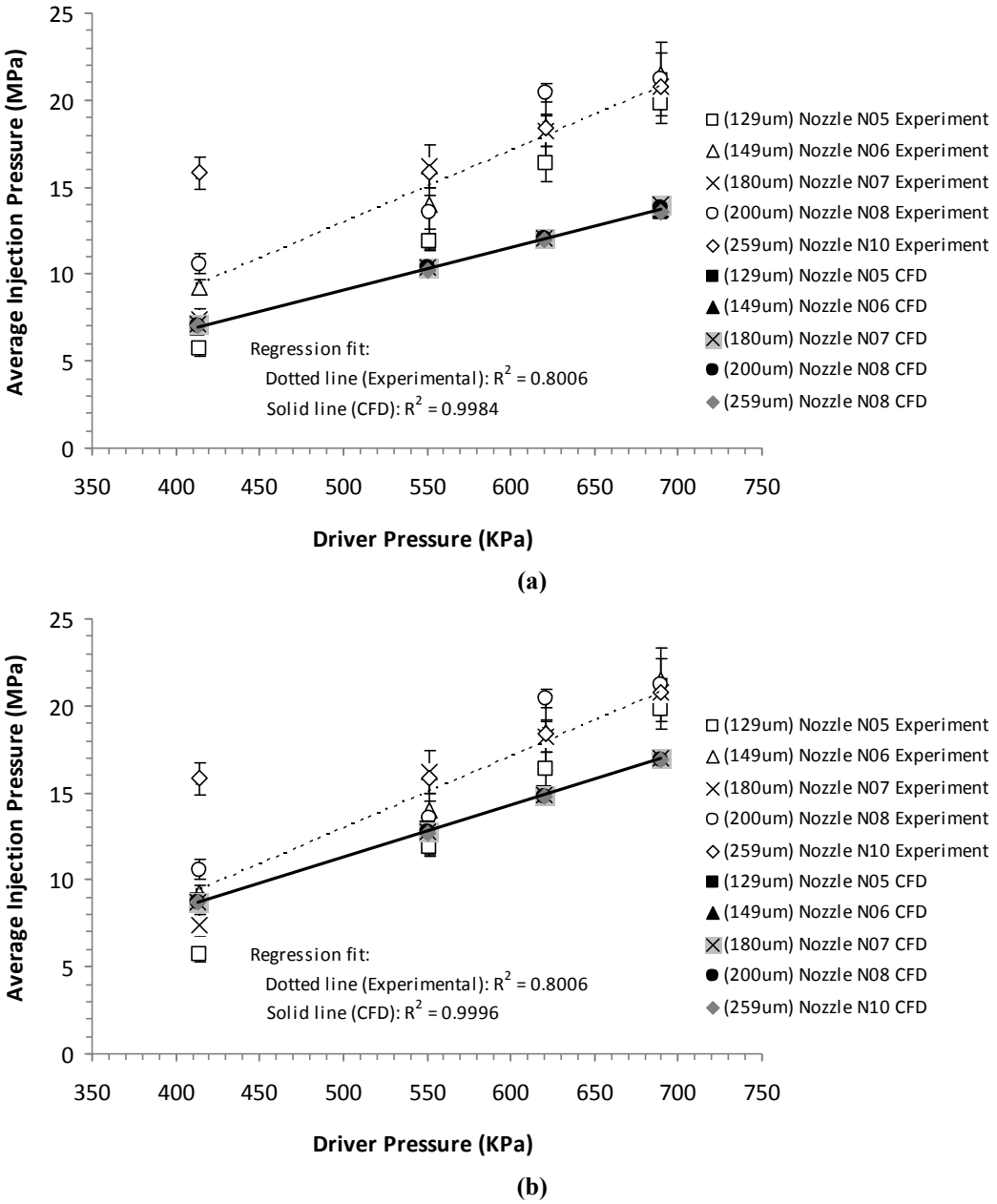

Figure 3.13. Average stagnation pressure as a function driver pressure. a) space-averaged CFD value; and b) centerline CFD value.

A parametric study of two main injector characteristics, i.e., driver pressure and nozzle size, is performed and summarized in Fig. 3.12 and Fig. 3.13. Simulations were performed for five different nozzles operating at four different driver pressures of 413,

550, 620 and 690 kPa. Also shown in these figures are the experimental data with 95% confidence interval error bars for comparison.

Figure 3.12 illustrates the peak stagnation pressure variation as a function of driver pressure for different nozzle sizes. A visual examination of both CFD and experimental data suggests a linear increase in the peak pressure as the driver pressure is increased from 413 to 690 kPa. Indeed, the least square linear regressions obtained for both results have the coefficient of determination R^2 values above 0.80 (0.9968 for CFD space-averaged, 0.9871 for CFD center-line and 0.8396 for the experiments). In addition, the numerical results from the CFD model agree very well with the experimental data again by taking into account different experimental limitations as previously discussed.

Similarly, the average stagnation pressure after the pressure peak was also analyzed. Figure 3.13 demonstrates the variation of average injection pressure after the pressure peak, as a function of driver pressure for varying nozzle diameters. The CFD solutions show a linear increase in stagnation pressure as the driver pressure increases within the operating range, and this agrees with the trend from the experimental measurement. The R^2 values from the least-square regression are 0.8006, 0.9984 (space-averaged) and 0.9996 (center-line), respectively, for the experimental and CFD correlations. However, it appears that the experimental data for average pressure is slightly higher than the predicted values obtained using the CFD model. Nevertheless this variation is still acceptable given that the force it represents is only a small fraction of the force transducers range.

From Fig. 3.12 and Fig. 3.13, it can be observed from CFD simulations and equivalently depicted from experimental results that there is no significant variation

between the stagnation pressures values obtained using different nozzle sizes at the same driver pressure. These pressure values with different nozzle sizes (particularly from the CFD simulations) are very close to each other. In this numerical study, the obtained CFD results confirm our previous conjecture that the nozzle diameters do not have a large impact on the resulting stagnation pressures (Portaro & Ng, 2013). The weak dependency between the nozzle size and resulting stagnation pressure can be explained by analyzing the system in terms of energy. Although the area of the nozzle exit is varied, the area of the plunger remains the same which means the total energy imposed on the fluid for a given driver pressure remains the same irrespective of the exit nozzle area. If fluid damping is not present in the system then one would expect much higher velocities for smaller nozzle areas. However, fluid damping in the system causes there to be more energy dissipation for smaller nozzles due to the coupled hydro-mechanical activity through pressure change and the force required to push the fluid through a smaller exit area. Consequently, the CFD model predicts the same stagnation pressure for the tested nozzle sizes from a 250 to 130 μm nozzle diameter, which is in agreement with the experimental observation (Portaro & Ng, 2013).

Simulations are also performed to look at the effect of stand-off distance. The stand-off distance is defined as the gap between the pressure measurement point and the nozzle exit. Although in real practice when the injector is used to administer medication, the nozzle shall come in direct contact with the skin and that the stand-off distance will typically not exist. Nevertheless, it is of interest to analyze if this can represent a source of error in the experimental measurement since it was not possible to have the injector contact the force transducer directly, and to reveal the significance of this effect on the

injection performance parameters. Figure 3.14 illustrates three different gap sizes tested with a 180 μm nozzle and at a driver pressure of 690 kPa and in agreement with the experimental observation (Portaro & Ng, 2013), the numerical results confirms that within the distance from 0 to 15 mm, there is no significant variation in both peak and average stagnation pressure measurement in relation to different gap distances.

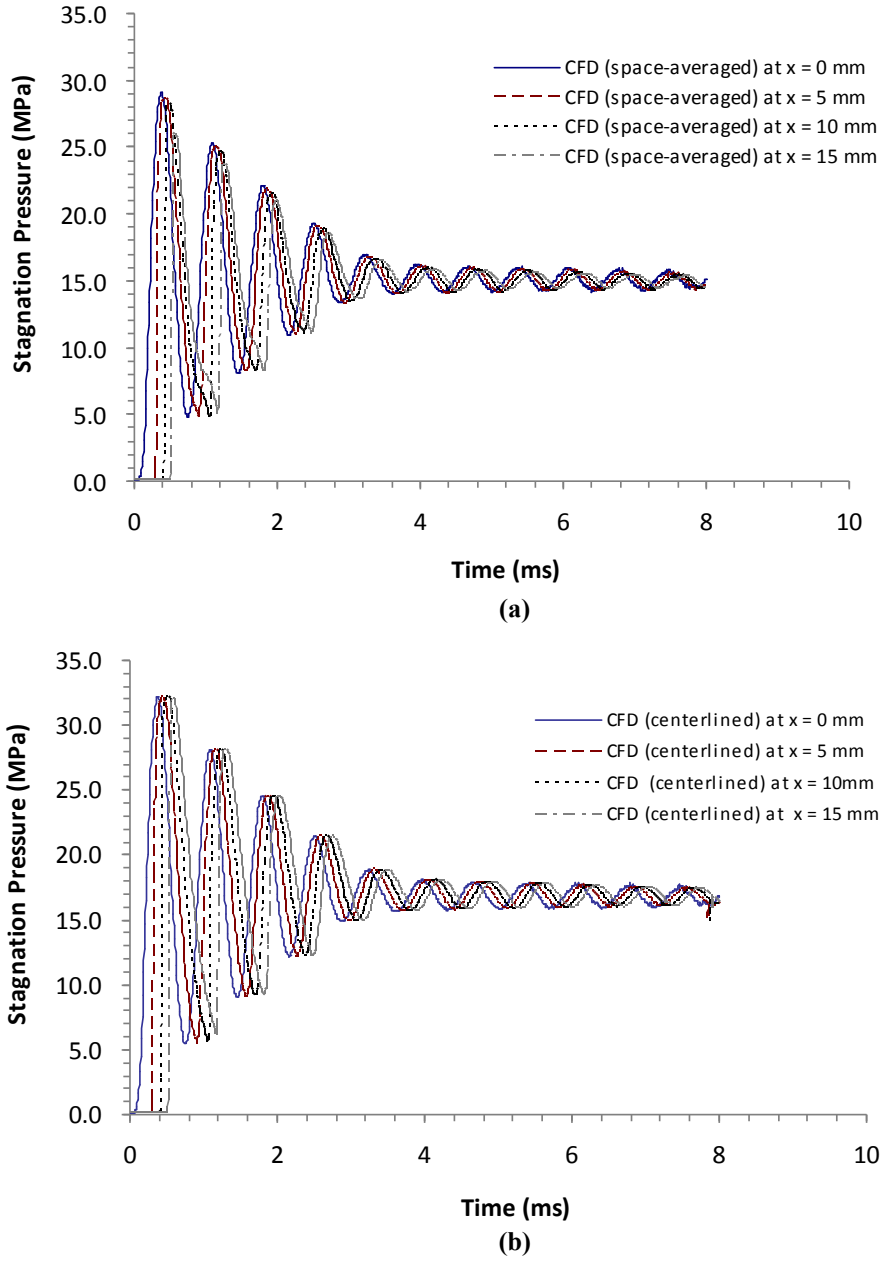

Figure 3.14. Effect of stand-off distance on stagnation pressure. a) space-averaged CFD value; and b) centerline CFD value.

The CFD results also confirm that the injection chamber volume does not play a significant role in impacting the peak or average stagnation pressure. The results show that it affects mostly the period over which the damping occurs. Figure 3.15 illustrates the modeled differences from CFD in the injection time pressure profile for both a 25 mm and 10 mm long chamber length. The CFD results demonstrate an almost identical match in peak pressure and average stagnation pressure; however the shorter column oscillates more frequently about the average stagnation pressure than the longer column. Furthermore, there is also a time shift between the peak stagnation pressures of both column lengths. The longer column requires about 0.2 ms more to reach its peak stagnation pressure than the short column. The time shift can be explained by the fact that the larger volume imparts more damping thereby shifting the peak of the injection pressure slightly.

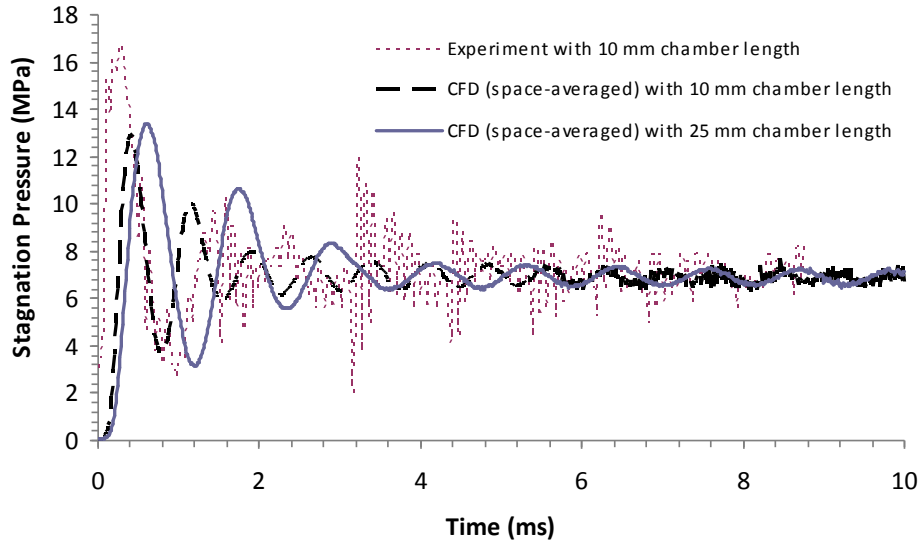

(a)

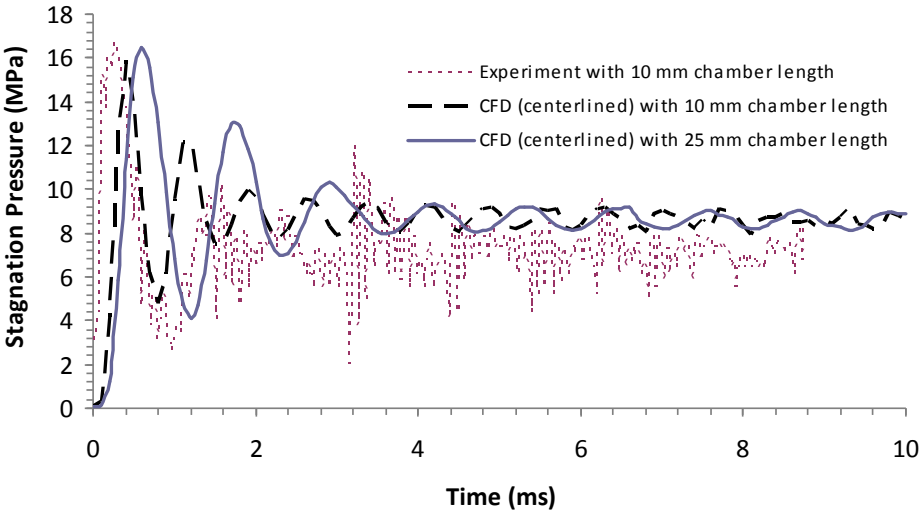

(b)

Figure 3.15. Effect of injection chamber length on stagnation pressure. a) space-averaged CFD value; and b) centerline CFD value.

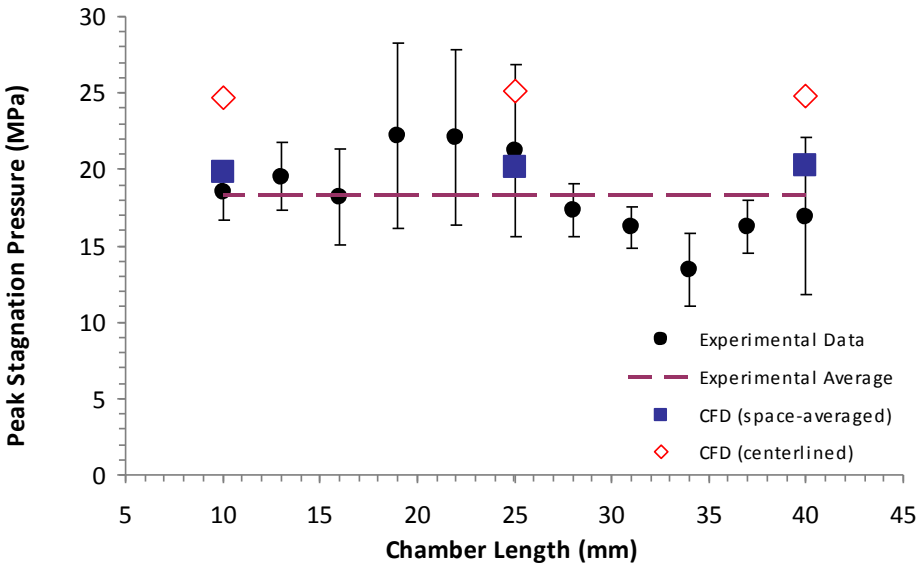

(a)

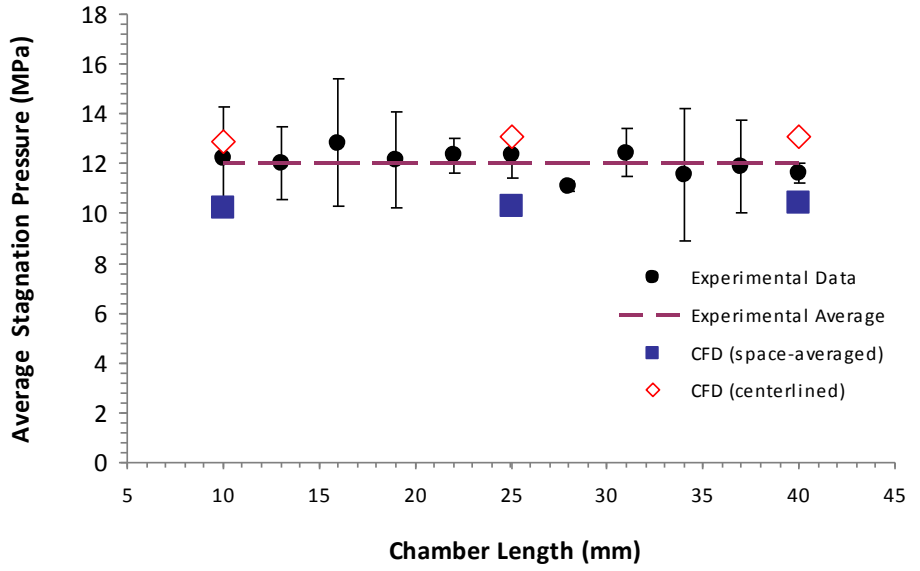

(b)

Figure 3.16. Peak and average stagnation pressures obtained for different chamber lengths of the injector with a 129 µm nozzle and p_D = 550 kPa.

More simulations are also performed in order to further validate the notion that injection chamber length has a minimal effect on peak and average pressure. Simulations were carried out using a 129 µm nozzle in conjunction with a 550 kPa driver pressure,

and the injection peak and average stagnation pressures were tracked for three different chamber lengths of 10, 25 and 40 mm. Figure 3.16 illustrates these numerical results, together with the experimental measurement. It shows that the CFD results remain constant as chamber length is increased from 10 mm to 40 mm. Experimentally, there is no specific trend that emerges and the test points are scattered nearby the a constant value. Hence, both results from simulations and experiments illustrate that the injection chamber length has no effect on average stagnation pressure.

As discussed earlier, the accuracy of the numerical solutions of the peak and average stagnation pressures can depend on the modeling of O-ring friction. In addition, the O-ring friction also has an important influence on the settling time for the oscillatory behavior of the time-pressure profile of a given injection. Figure 3.17 illustrates the modeled behavior of friction; it is possible to see that without friction the model oscillates significantly about an average stagnation pressure, whereas at 50% friction the model settles to an average stagnation pressure more rapidly. Finally, the numerical model behavior with friction settles to an average value within approximately the first 2 ms of the injection. The peak and average stagnation values are slightly lower than those predicted without O-ring friction.

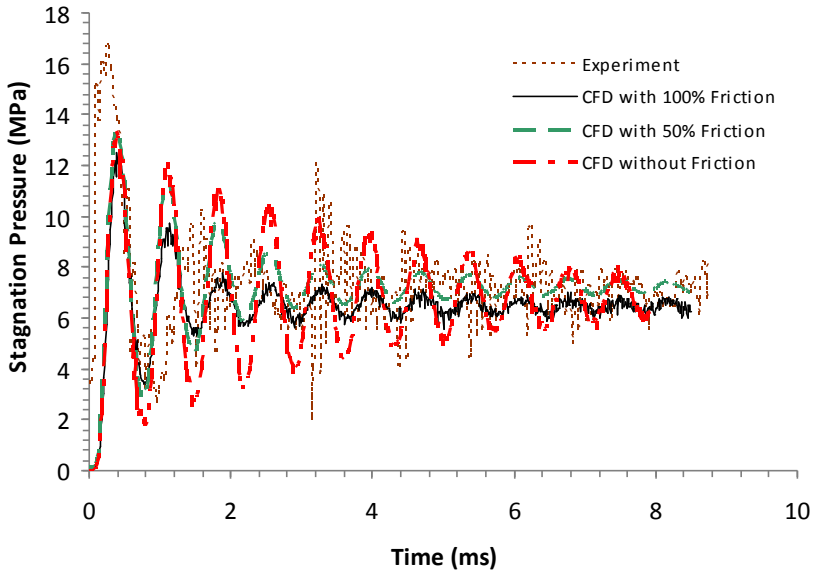

(a)

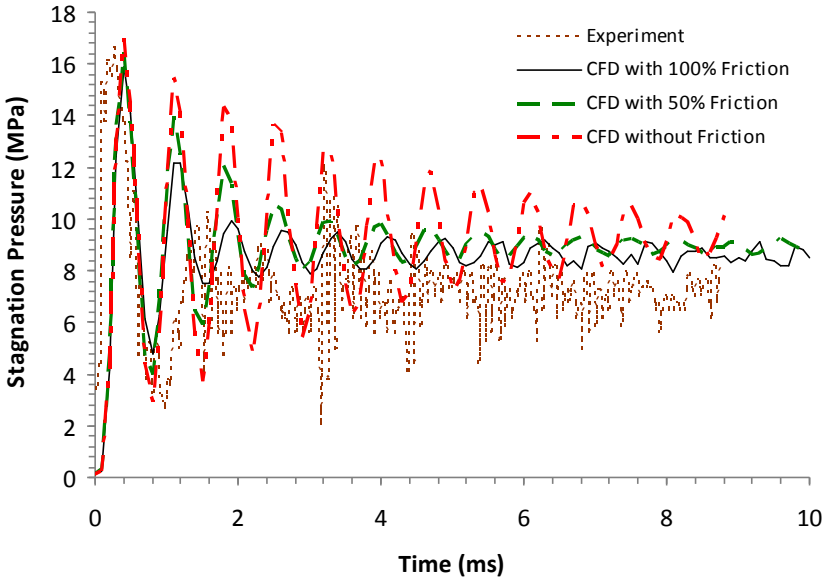

(b)

Figure 3.17. Effect of friction on the stagnation pressure. a) space-averaged CFD value; and b) centerline CFD value.

3.6. Summary

Using a combined LES/VOF technique with dynamic mesh and moving boundary method, made it possible to successfully simulate the behavior and performance

characteristics of an air-powered needle free injector. Numerical results for stagnation pressure, one of the key performance parameters for needle free liquid injectors, are validated with experimental measurements; and the general experimental observations agree very closely with the numerical model developed throughout this study. The CFD model makes it possible to analyze which parameters among driver pressure, nozzle diameter, liquid column length and frictional losses most significantly impact the peak and average stagnation pressures of the jet exiting the air-powered needle free liquid injector and to obtain an optimal design of this biomedical engineering device. The CFD model also agrees very closely with similar experimental studies discussed in Portaro & Ng (2013). CFD results demonstrate that as the driver pressure increased both the peak and average stagnation pressure increased almost linearly within the operating range considered. Varying the injection nozzle diameter, whilst keeping the driver pressure constant does not have any significant impact on the peak or average stagnation pressure. The chamber length and the stand-off distance were varied, and no significant influence is found on peak or average stagnation pressure. The validated numerical results obtained in this work mean this numerical model can be readily used in future research, to further explore the relationships between various injector design parameters and improve the injector's effectiveness in delivering an injection.

Chapter 4

CFD Analysis of a Diaphragm-less Shock Tube

4.1. General overview

Shock tube is a classical research tool to study shock wave dynamics and high-speed compressible flows. It is a facility used in many disciplines such as thermo-aerodynamics, combustion, chemical kinetics or biomedical engineering, etc. A shock tube consists of low and high pressure regions and conventional designs usually use diaphragms to separate the driver and driven section from each other before experiment. A shock wave is generated and propagates into the low pressure region upon the rupture of this diaphragm. A number of mechanisms have been designed to replace diaphragms in shock tubes, resulted in a so-called diaphragmless shock tube. In this Chapter, CFD simulation is carried out to investigate the fluid mechanics and performance characteristics of a diaphragmless shock tube driver based on the design by Downey et al. (2011) using a rapid opening sleeve valve. A combined numerical approach using moving boundary method as introduced in Chapter 2 for the motion of the sleeve and compressible fluid solver is used to simulate the shock formation during the operation of the diaphragmless shock tube.

4.2. Problem description

Shock waves play integral roles in many industrial, medical and scientific environments, consequently it is important to observe the behavior of these waves and how they interact with their surroundings; see the review paper by Takayama & Saito (2004). Traditionally, shock tube is a standard facility to investigate the physics of shock waves and is generally composed of high-pressure driver and low-pressure driven test sections. The classical design is to use a thin diaphragm to separate these two sections and a sudden rupture of the diaphragm leads to the generation of a shock wave traveling into the low-pressure section.

Although the bursting diaphragm is an easy way to realize the near instantaneous removal of the separation between the driver and driven sections, this traditional method has several practical disadvantages as follows. A new diaphragm must be used for each test and the preparation is time consuming and inconvenient to automate. Although it is possible to obtain rupture pressures within 1% reproducability with the use of cross-scratched diaphragms, it can also result in poor repeatability due to the inconsistent rupture of each diaphragm (Bradley, 1962). Moreover, fragments of the burst diaphragm may impact and damage the pressure transducers attached along the driven tube, and require partial disassembling of the shock tube to remove the debris (Tranter et al., 2001).

Alternatively, diaphragm-less shock tubes have been developed by many research groups to provide a quick and effective means of producing shock waves, (e.g., Ikui et al., 1976; Yang et al., 1994; Takano and Akamatsu, 1984; Kosing et al., 1999; Hariharan et al. 2011; Hosseini et al., 2000). The major advantages compared to conventional diaphragms include, minimal downtime between repeated experiments, opening times

comparable to those of conventional diaphragms and infinitely adjustable opening pressure without the use of various diaphragm thicknesses and hence, eliminates fragments that are carried downstream of the shock tube once the conventional diaphragm is ruptured. However, one of the primary challenges with the diaphragm-less approach is to achieve a sufficiently rapid or optimal valve opening time to generate a well-formed shock wave in a reasonable tube length.

In this Chapter, the objective is to analyze a recent design of diaphragm-less shock tube by Downey et al. (2011) particularly to look at the effect of opening times on the shock formation and to study the flow field during the process. Computational Fluid Dynamics (CFD) simulation is carried out to investigate the influence of shock tube driver parameters to the shock formation and to validate numerical results with experimental data for the shock strength as a function of driver pressure.

4.3. Design and functionality

In this work, the performance characteristics of a diaphragm-less shock tube driver based on a design proposed by Downey et al. (2011) is investigated. Such proposed design utilizes a rapid opening sleeve to mimic the rupture of a diaphragm. Portaro & Ng (2012) had constructed the similar diaphragm-less shock tube driver based on the Downey et al. (2011)'s design using a longer sleeve length to achieve increased opening times. The drawing shown in Fig. 4.1 illustrates this design concept. The shock tube's mechanisms function on differential pressures. The trigger chamber is first filled to the same pressure as the driver; this will close the exhaust ports and prevent gas from escaping. Once the trigger chamber is filled, it is then possible to fill the actuating

chamber. This action will force the high speed aluminum sleeve to seal the driven section of the shock tube. It is then possible to fill the driver with the test gas and vacuum the driven tube if necessary. Completing these quick steps will result in a shock tube which is ready to perform an experiment. In order to create the shock wave it is necessary to release the gas in the triggering chamber, thereby opening the exhaust ports allowing the gas from the actuating chamber to escape rapidly. This will result in the high speed aluminum sleeve being driven backwards and creating an opening at speeds close to 100 m/s for the high pressure gas to escape. For instance, Fig. 4.2 shows the resulting opening time of the sleeve as a function of initial pressure ratio based on a force balance and kinematic analysis by Portaro & Ng (2013) from the prototype design and the terminal velocity based on these time scales corresponds roughly to the same order of magnitude (with a max. 1 inch gap). Consequently, the rapid opening combined with the drastic pressure change will generate a shock that will travel in the driven part of the shock tube.

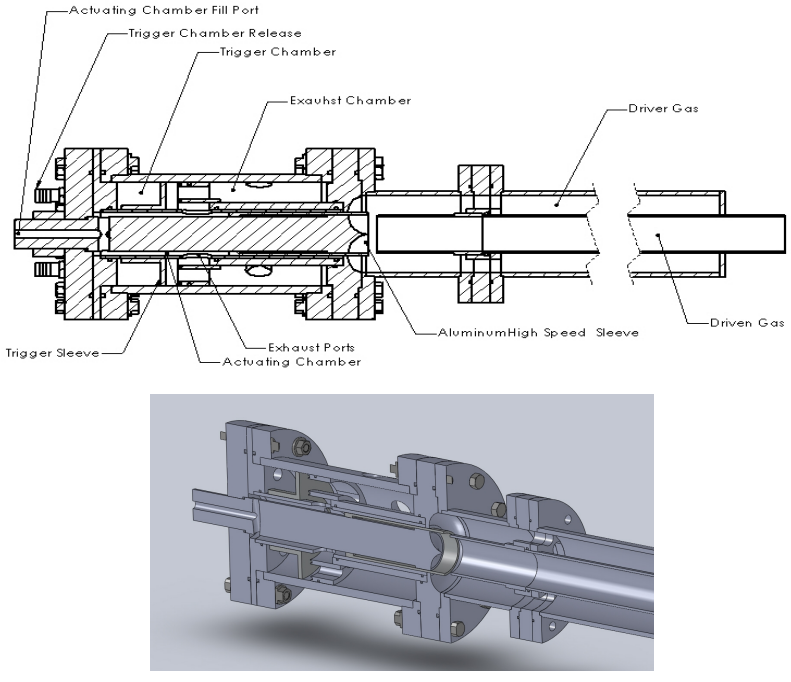

Figure 4.1. Schematic diagram of the diaphragm-less shock tube driver using a rapid opening sleeve originally proposed by Downey et al. (2011).

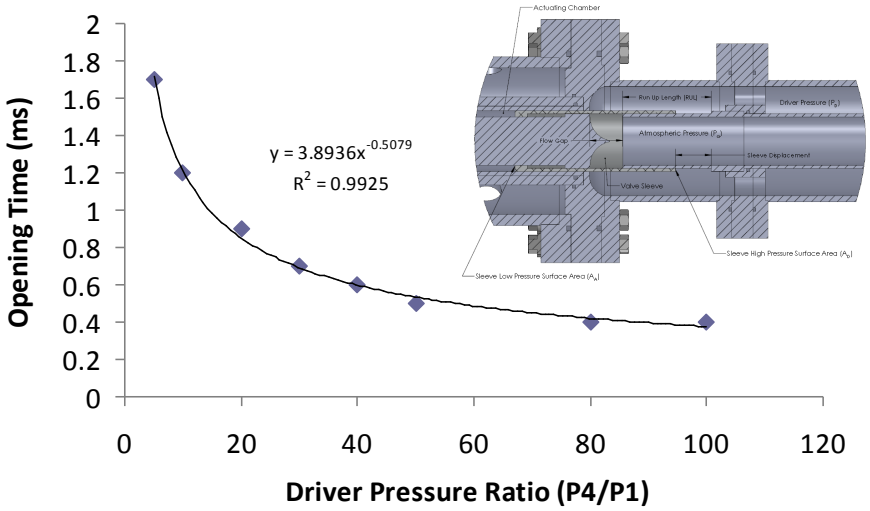

Figure 4.2. Terminal velocity of the sleeve as a function of initial pressure ratio based on a force balance and kinematic analysis (Portaro & Ng, 2013).

4.4. CFD modeling

In this research work, CFD is applied to the equivalent Downey et al.'s diaphragm-less shock tube design to analyze and understand better the process of shock wave generation and propagation inside this device for improvement. All simulations are carried out using the OpenFOAM® CFD software package (OpenCFD, 2013). As a first stage in the analysis, a simple numerical model considered of a axi-symmetric domain and a flat moving boundary is considered as given in Fig. 4.3. The key dimensions of the numerical model such as the sleeve thickness, the tube diameters are equivalent to those of the experimental facility shown in Fig. 4.1. These physical dimensions and average grid size for each domain used in the CFD simulation are summarized in Table 4.1. It is noted that average cell size in Table 4.1 is for base mesh case and the grid is refined in the gap region to capture steep gradient of pressure, velocity and temperature, in other words, discontinuity of physical properties. The most important part is the inner driven tube section since the shock strength is measured in this section.

Domain Name	Radius (y- coordinate)		Length (x-coordinate)	
Model 1	Dimension	Average Cell Size	Dimension	Average Cell Size
Outer Tube	63.5	0.13	101.6~152	2.1
Inner Tube	25.4	0.13	101.6~152	0.53
Expanding gap (variable domain)	63.5	0.12	$2 \times 10^{-2} \sim 25.4$	$5 \times 10^{-4} \sim 0.64$

Table 4.1. Physical Dimensions of Computational Domain (unit: mm)

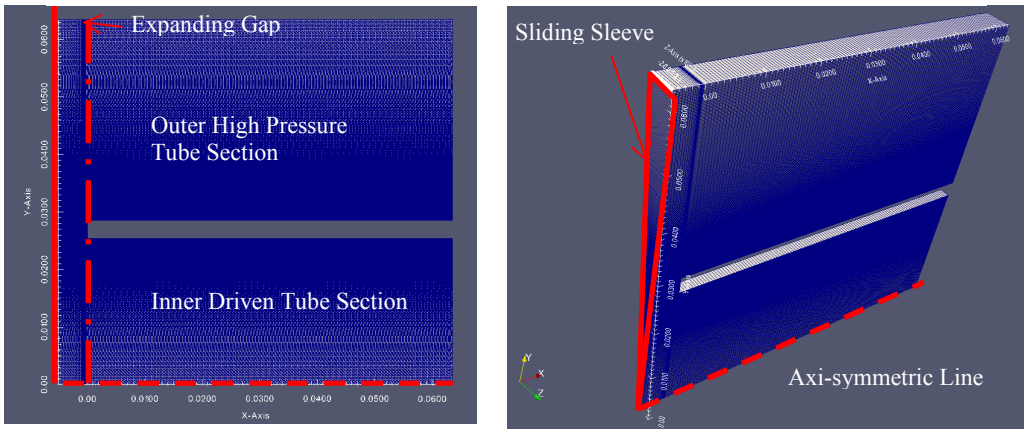

(a) *xy*-plane View (b) Isometric View

Figure 4.3. Computational domain for the diaphragm-less shock tube driver

The sliding sleeve is actuated by the relief of high-pressure gas contained in the actuating chamber and creates the opening gap between the inner and outer tube. To simulate the high-speed motion of the driver sleeve, the dynamic mesh technique is used with the 2-dimensional moving boundary. Constant force is assumed to move the sleeve during operation and the friction force between the sleeve and a housing part is negligible. Therefore, the speed of the sliding sleeve is treated as constant. The moving boundary moves in totally 1 inch during simulation and the initial expanding gap is set as a minimal since the gap is required so as to begin simulation. During the opening motion, the high pressure gas is exposed to the inner tube though the resulting opening gap leading to the shock formation process within this device. The moving boundary position

is obtained by solving Laplace equation for mesh velocity at each computational time step. For the modeling of the sleeve motion, the following assumptions are introduced:

- The sleeve is a solid body, i.e., no-deformation occurs;
- The sleeve-opening speed is constant;
- The mass of the sleeve does not change during the simulation;
- The thickness of the sleeve and mechanical structure are neglected;
- The friction force between the sleeve and the housing part is neglected.

These assumptions are used in OpenFOAM (OpenCFD, 2013) and a built-in *velocityLaplacian* class is selected as a motion solver to move the sleeve model with constant velocity. In this class, the sleeve is treated as a moving boundary with constant velocity U_b. As discussed in Chapter 2, the mesh-point velocity field U_m is determined by setting U_b as a part of boundary condition and solving the Laplace equation for mesh velocity field below.

$$\nabla \cdot \left(\delta \nabla U_m \right) = 0 \tag{4.1}$$

where, δ is constant or variable diffusion field to govern mesh motion. Boundary condition for the motion equation includes other boundaries such as inner surface of the inner/outer tubes, cyclic surfaces, symmetry plane (line) besides the moving sleeve boundary. After solving Eq. (4.1), U_m is used to modify vertices:

$$r_{new} = r_{old} + U_m dt \tag{4.2}$$

Much attention is taken into consideration when diffusivity and non-orthogonal coefficients are chosen in *velocityLaplacian* class (OpenCFD, 2013). Otherwise, internal mesh especially within the generated expanding gap is squeezed and deformed too much so that flux cannot be calculated precisely.

For the shock tube simulation, the inviscid compressible Newtonian fluid flow is governed by the following equations expressing conservation of mass, momentum and energy:

$$\frac{\partial \rho}{\partial t} + \nabla \cdot (\rho \mathrm{U}) = 0 \tag{4.3}$$

$$\frac{\partial (\rho \mathrm{U})}{\partial t} + \nabla \cdot (\rho \mathrm{UU}) = -\nabla p \tag{4.4}$$

$$\frac{\partial (\rho e)}{\partial t} + \nabla \cdot (\rho \mathrm{U} e) - \nabla \cdot \left(\frac{k}{c_v} \right) \nabla e = p \nabla \cdot \mathrm{U} \tag{4.5}$$

where:

$$e = c_v T,\ p = \rho R_s T \tag{4.6}$$

which are dicretized using the Finite Volume Method with 2nd order accuracy and the used computational scheme is the pressure-correction based PISO (Pressure Implicit with Splitting of Operators) algorithm (OpenCFD,2013) to rectify the second pressure correction and correct both velocities and pressure explicitly. Temperature is calculated in Eq. (4.5) after obtaining energy at each time step and density is updated by obtained p and T in the equation of state. In all simulations, air is used as the medium in the simulation and treated as as a perfect gas. Pressure value is set to 4 ~ 25 kPa inside the outer tube and a part of the expanding gap and others to atmospheric pressure (e.g., 101,325 Pa) as initial condition. Temperature is set to 298 K throughout the domain at t = 0 s. Then, the moving-wall boundary moves in negative x-direction with constant speed and expands computational domain during simulation. Thus, the high-pressure gas passes through the gap created by the moving wall. Other boundaries are physical walls except for axi-symmetric conditions such as symmetric line and cyclic surfaces. Physical walls are slip surfaces since Euler-type equation is adopted as governing equation. Details are indicated in Table 4.2.

Physical Quantity	Physical Walls	Moving Wall
Pressure (p)	zeroGradient	zeroGradient
Velocity (U)	Slip	movingWallVelocity, uniform (0 0 0)
Temperature (T)	zeroGradient	zeroGradient

Table 4.2. Boundary and Initial Conditions in OpenFOAM

The time step size Δt of the order of 10^{-9} s is selected to obtain stable solutions and not to deform the mesh dramatically in one time step. In OpenFOAM, the combination of *sonicFoam* and *dynamicFVMesh*, whose name is *sonicDyMFoam*, is selected as a complete solver to simulate the fluid phenomenon inside the diaphragmless shock tube driver (OpenCFD, 2013).

4.5. Results and discussions

4.5.1. Validation

To first validate the numerical method in OpenFOAM, one-dimensional ideal shock tube simulation is also run and initial conditions described in Table 4.1 are selected based on the well-known Sod's shock tube problem (Sod, 1978). The derivation of the exact analytical solution to the shock tube problem can be found in any gasdynamic or CFD textbook (e.g., Hirsch, 2007; Toro, 2009) with simple computer code available to describe the evolution of the fluid in the 1-D shock tube flow. Detailed derivations of the ideal 1-D shock tube flow are provided in Appendix A. One can test any computational fluid code against this analytical solution and get information how good the numerical scheme captures and resolves shocks and contact discontinuities and reproduce the correct flow field profile.

In the present validation, the 1-D shock tube has a length of 254 mm (10 inch) and computational mesh (Δx = 0.01 mm) is generated in OpenFOAM. The diaphragm is placed in the exact middle at x = 127 mm (or 5 inch). Both sections are filled with air, so γ = 1.4, but at different pressures and densities. The tube is closed at both ends. The end walls have slip conditions for velocity and air is treated as a calorically perfect gas. The computation continues until any wave has reached the left or right boundaries.

Region	**Pressure p_4/p_{ref}**	**Density [kg/m^3]**	**Velocity [m/s]**
Driver Part (Region1)	1.0	1.0	0
Driven Part (Region 2)	0.1	0.125	0

Table 4.3. Initial conditions for the Sod's shock tube problem

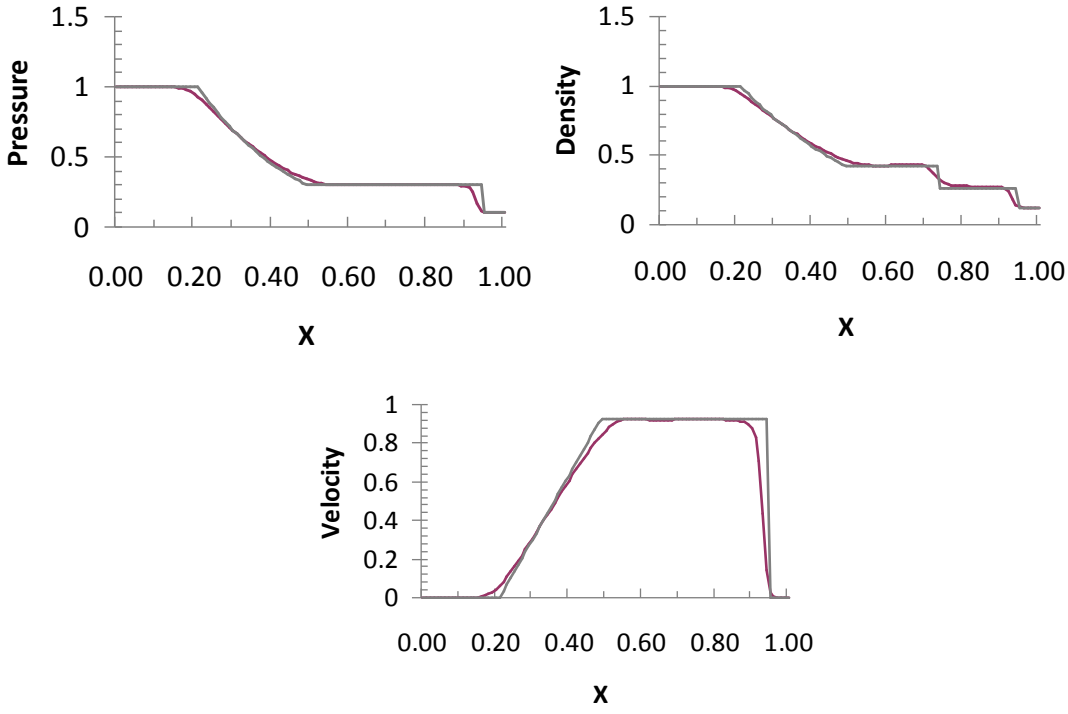

Figure 4.4. Comparison between the CFD results (– red) with the exact solution of the Riemann problem (– gray) using the Sod's shock tube problem.

Figure 4.4 compares the analytical shock tube solutoin with the numerical results obtained from the CFD simulation. It can be seen that both solutions are in good agreement. This classical validation case by Sod (1978) therefore demonstrates the use of the OpenFOAM algorithm in capturing the shock and expansion waves inside a shock tube.

4.5.2. Diaphragmless shock tube results

With the proper validation, the numerical results from the simulation can thus be used to assess the performance of the diaphragm-less shock tube configuration which is multi-dimensional. Figure 4.5 shows exemplarily the pressure contour plots illustrating the shock formation with an initial driver pressure p_4/p_1 ratio of 7.91 and an opening gap velocity of -50 m/s. In addition, the pressure variation within the shock tube recorded at different axial positions is also given in Fig. 4.6. In general, due to the geometry of the shock tube driver, there are a number of different wave interaction and reflection near the opening gap region. In general, a planar shock appears to establish well within 100 mm. The large pressure increase at shorter distances from the opening gap is due to the wave reflection from the centerline axi-symmetry (recorded at y = 0 mm).

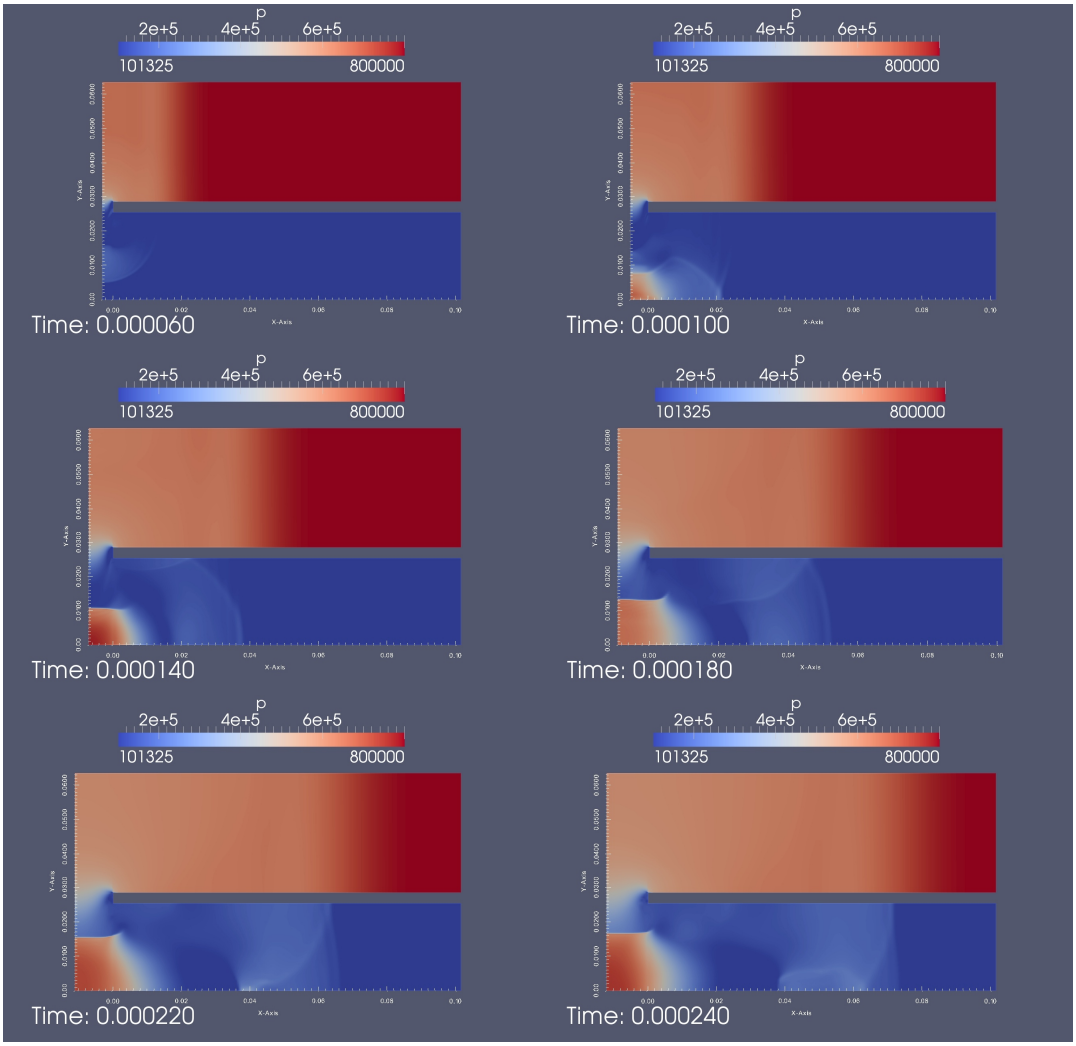

Figure 4.5. Pressure contours showing the shock evolution with an initial driver pressure ratio of p_4/p_1 = 7.91 and a gap opening velocity of -50 m/s

To assess the effect of the numerical resolution, simulations are also performed with different grid size and an example of comparison of the pressure profile at the early transient shock development is given in Fig. 4.7. One can see that there is no significant discrepency between the results using the base grid (Δx = 0.53 mm) and those with higher resolution (Δx = 0.26 mm). Therefore, the base grid results are used in all the subsequent analysis.

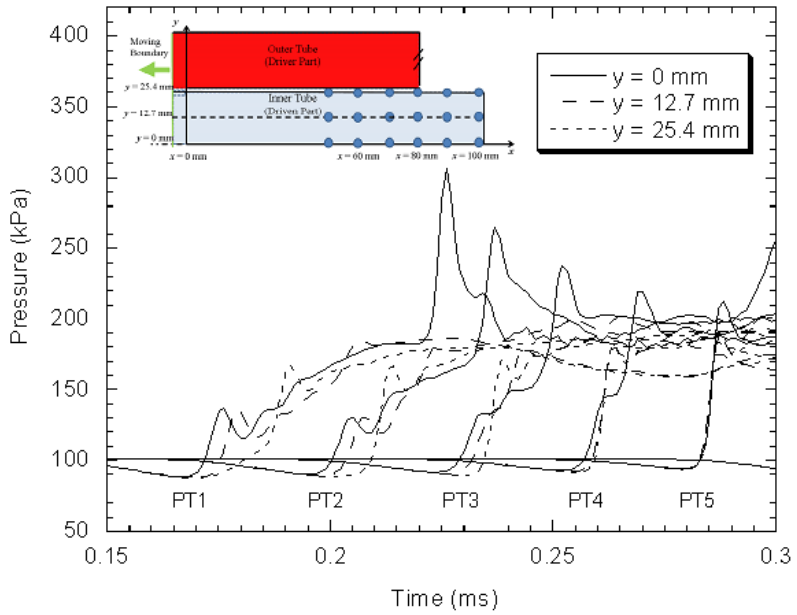

Figure 4.6. Pressure profiles at different axial positions along the driven section (from x = 50 to 100 mm) and three different radii (y = 0, 12.7 and 25.4 mm)

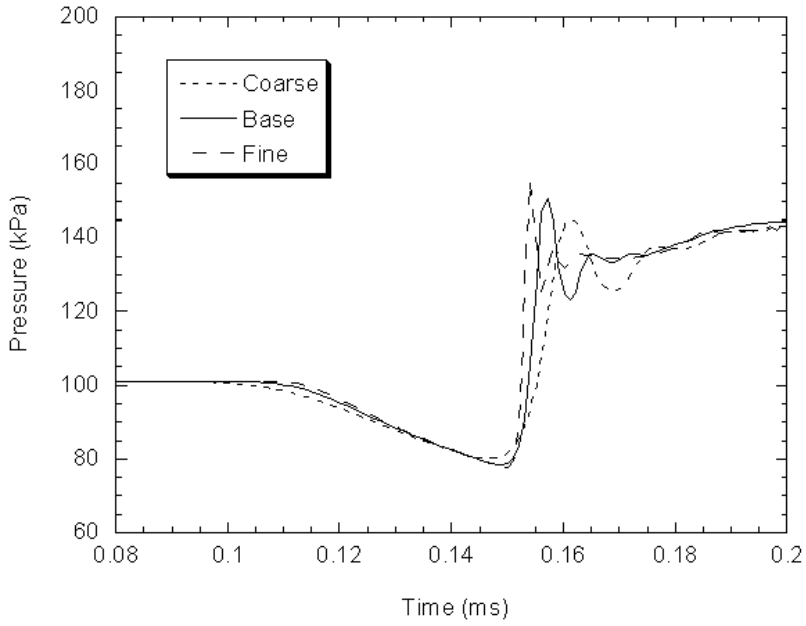

Figure 4.7. Pressure profiles at a position of x = 40 mm and y = 0 mm obtained using different mesh sizes.

The shock strength resulted from different initial driver pressure ratios and gap opening velocities is plotted in Fig. 4.8. The numerical results obtained from an earlier

study (Portaro & Ng 2013) with complete opening of the gap at t = 0 s with non-moving boundary are included. In this plot, the experimental measurement by Portaro & Ng (2013) from the present shock tube driver operated at low pressures ranging from 400 to 750 kPa using PCB pressure transducers are also shown, as well as those from literature (Kosing et al., 1999; Downey et al., 2011). Using the analytical solution of the 1-D ideal shock tube problem as derived in the Appendix A, the incident shock strength p_2/p_1 as an implicit function of the diaphragm pressure ratio p_4/p_1 can be obtained for comparison with the experimental results, i.e.,

$$\frac{p_4}{p_1} = \frac{p_2}{p_1}\left(1 - \frac{(\gamma-1)(a_1/a_4)(p_2/p_1 - 1)}{\sqrt{2\gamma}\sqrt{2\gamma + (\gamma+1)(p_2/p_1 - 1)}}\right)^{\frac{-2\gamma}{\gamma-1}} \tag{4.7}$$

$$\frac{p_2}{p_1} = \frac{2\gamma M_s^{\,2} - (\gamma - 1)}{\gamma + 1} \tag{4.8}$$

The above equations the shock strength should be solved iteratively and the relationship between p_2/p_1 and p_4/p_1 can be expressed on a graph. These results are used for benchmark to validate the simulation of the diaphragm-less shock tube.

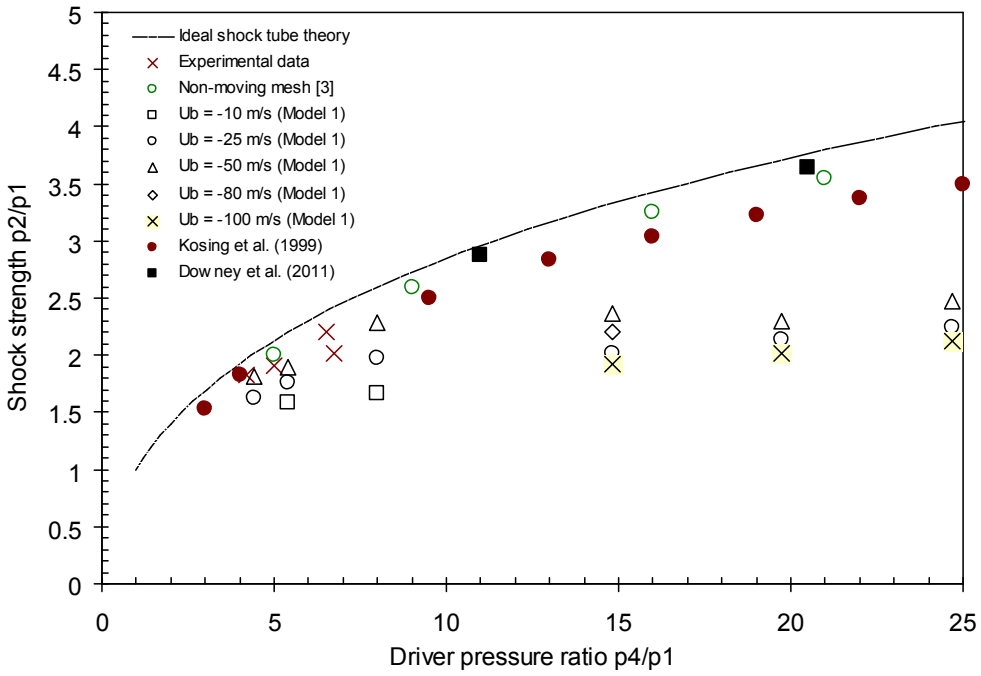

Figure 4.8. The shock pressure from CFD simulations at x = 100 mm and experiments as a function of the initital driver pressure ratio. The solid line indicates the theoretical solution obtained from the 1-D shock tube theory.

From Fig. 4.8, one can see that the numerical results agree very well with data from literature as well as the ideal 1-D shock tube solution at low initial driver pressure ratios. Increasing the gap opening velocity tends to give better results comparable to the 1-D ideal shock tube solution. However, as we increase the driver pressure ratio to higher values using the simplified numerical model as shown in Fig. 4.8, it appears that there is an optimal gap opening velocity and further increase in sleeve velocity (or the left boundary motion) has an adverse effect by lowering down the shock strength away from the ideal 1-D value. In fact from either Fig. 4.6 or Fig. 4.7, one may notice an expansion (or referred to the vaccuum effect) in the driven section due to the movement of the sleeve by the left-hand boundary. The inertial of the left boundary wall is similar to the creation of a vaccuum effect as by a piston extraction (Anderson, 2003). Such effect can

generate expansion waves which can therefore influence the flow field in the driven section and hence in turn decrease the strength of the resulting shock wave created by the expansion of the high pressure gas from the opening gap.

4.5.3. Improved design and numerical model configuration

To resolve the effect of the motion of the boundary which in turn disturbs the flow in the driven section due to the suction effect generated by the inertia of the moving part, a new numerical model is created by including a sleeve on the right moving part as shown in Fig. 4.9. Unlike the original sleeve model 1 which has a flat geometry, this new model 2 has "T-shape" geometry where the opening gap (or the origin of the shock development) is away from the moving boundary to minimize the suction effect. The dimensions and grid sizes for the numerical computation is given in Table 4.4.

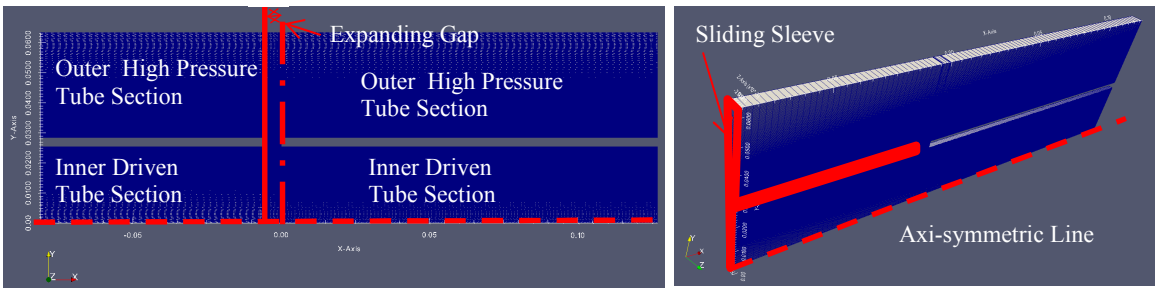

(a) *xy* - plane View (b) Isometric View

Figure 4.9. New geometry model for the diaphragm-less shock tube facility

Domain Name	**Radius (y- coordinate)**		**Length (x-coordinate)**	
Model 2	Dimension	Average Cell Size	Dimension	Average Cell Size
Outer Tube (L, R)	(63.5, 63.5)	(0.13, 0.13)	(76.2, 127~152)	(2.1, 0.53)
Inner Tube (L, R)	(25.4, 25.4)	(0.13, 0.13)	(76.2, 127~152)	(2.1, 0.53)
Expanding gap (variable domain)	63.5	0.12	$2 \times 10^{-2} \sim 25.4$	$5 \times 10^{-4} \sim 0.64$

Table 4.4. Physical Dimensions of Computational Domain (unit: mm)

The new model geometry is used to simulate the performance of the diaphragmless shock tube at higher initial pressure ratios where the vaccuum effect by the moving boundary becomes severe. The results are shown in Fig. 4.10; one can see that there is a significant improvement and increasing the boundary velocity gives the results approaching the typical performance of diaphragmless shock as shown by the experimental value of Kosing et al. (1999).

As observed in Fig. 4.11 showing the pressure contours and Fig. 4.12 the pressure profile at x = 110 mm (and y = 0 mm), where the opening gap is away from the moving boundary in the new geometrical model, the effect of the expansion originated from the boundary or the suction effect on the shock generation in the driven section is therefore minimized.

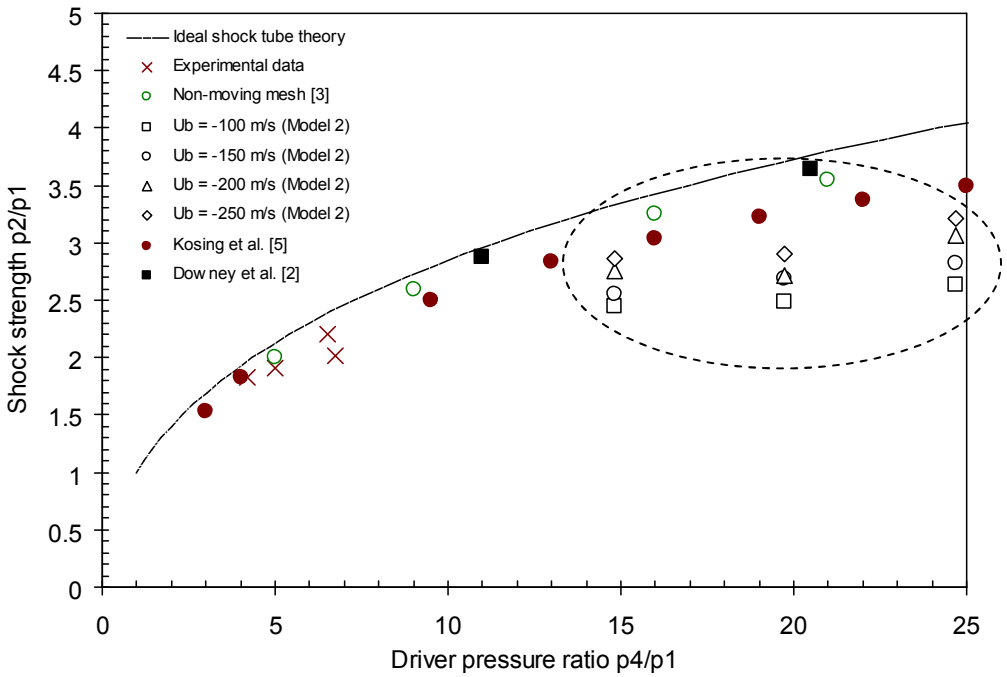

Figure 4.10. The shock pressure from CFD simulations at x = 100 mm using the new geometry and experiments as a function of the initital driver pressure ratio. The solid line indicates the theoretical solution obtained from the 1-D shock tube theory.

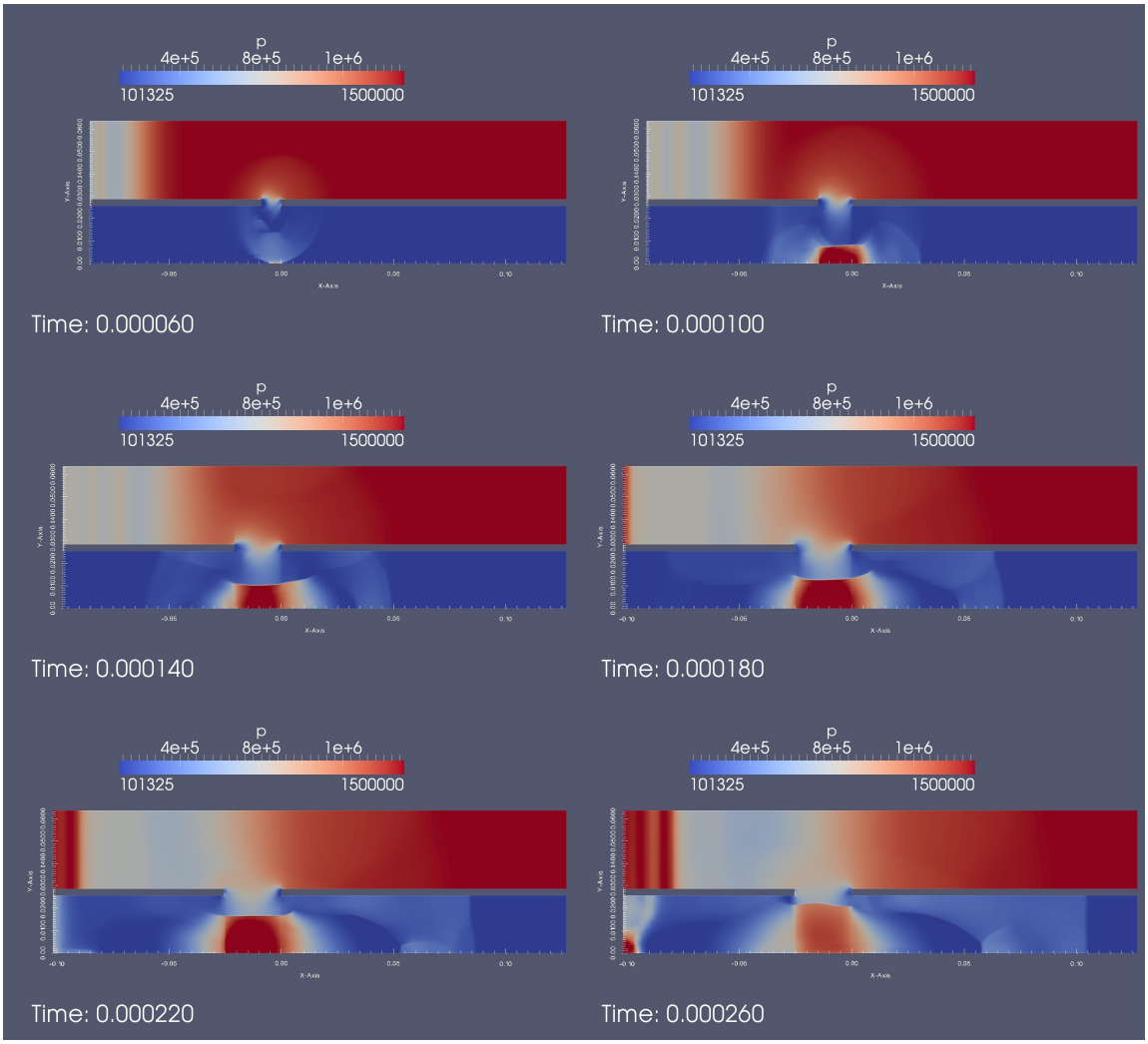

Figure 4.11. Pressure contours showing the shock evolution with an initial driver pressure ratio of p_4/p_1 = 14.8 and a gap opening velocity of -150 m/s using the new geometrical model

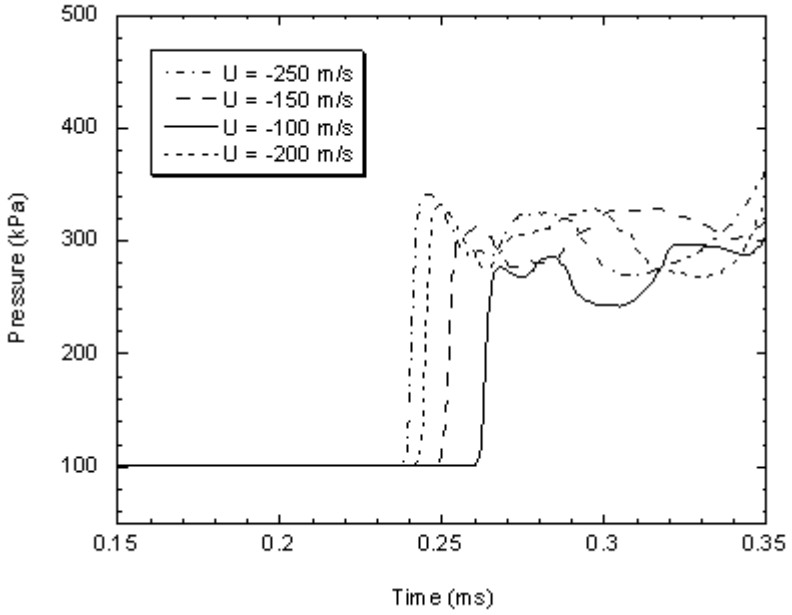

Figure 4.12. Pressure profiles at a position of x = 110 mm and y = 0 mm obtained using the new numerical model and different boundary velocities.

4.6. Summary

Comparing the theoretical results with their numerical and experimental counterparts makes it possible to observe a strong correlation between the driver pressure, sleeve opening time and shock mach number. Although the driver gas follows a more complex geometry into the driven section, it is evident that the behaviour is very close to a conventional shock tube with a controlled sleeve opening time. The present numerical results help to validate the reliability of the present diaphragm-less shock tube originally designed by Downey et al. (2011), which gives an invaluable tool for shock wave testing as experiments can be repeated quickly (less than 1 min) and with more repeatability than conventional shock tubes.

The numerical simulations also help to reveal some potential problems, for instance the effect of the moving part which generates disturbance in the driven section such as

the suction effect. A quick solution is proposed in this work by creating an improved numerical model by extending the the moving part with a T-geometry. It is indeed expected that better results will be obtained by contouring the opening and the left-hand boundary to guide the flow and shock formation.

Chapter 5

Concluding Remarks

5.1. General conclusion

Dynamic mesh method is a useful technique to apply CFD to industrial devices with dynamic components. In this study, the dynamic mesh method is used to the design of two engineering devices and the numerical CFD solutions are validated by comparing with experimental measurements and theoretical analysis to confirm its accuracy and efficiency as well as challenges and limitations.

The numerical methods applied in air-powered needle-free liquid jet injectors are the first of its kind to integrate dynamic mesh method, interaction between a forcing term that relates the air pressure used to drive the injection and fluid force, VOF and LES. The combination with dynamic mesh and state-of–the-art CFD techniques made it possible to verify which parameters most significantly impact the peak and average stagnation pressures for air powered injectors. The CFD model integrated with dynamic mesh proved so useful that it predicts reasonably accurate the stagnation pressure and jet velocity of the liquid stream exiting the injector.

Similarly in the flow simulation of the diaphragm-less shock tube driven by a fast-acting sleeve valve, introducing dynamic mesh into compressible flow simulation made it possible to observe a correlation between the driver pressure, sleeve opening time and

shock Mach number. The numerical model allows one to decide the initial pressure ratio and opening time by changing moving boundary velocity required to develop enough shock strength Furthermore, the results obtained in this study validate the reliability and design potential of the present diaphragm-less shock tube for further improvement.

However, several special treatments were taken into consideration to obtain reliable results in two application cases. Firstly, the correction terms (i.e., flux correction on the moving cell boundaries) to maintain conservation laws in flow physics were introduced into governing equation so as to handle dynamic mesh without any violation of physics in computers. Secondly, mesh diffusion coefficients were adjusted to keep mesh quality and validity. Thirdly, the geometry model in the shock tube simulation was modified not to generate pressure drop inside the tubes due to computational-domain expansion.

5.2. Contribution and future work

This study has made the contributions to the two industrial devices with dynamic components by using dynamic mesh method. The CFD approach with dynamic mesh can be used to predict the key performance parameters such as stagnation pressure in the needle-free injectors and the relationship between shock strength and opening time in the diaphragm-less shock tubes. These are of great importance for determining the design and operating performances in the two devices.

For future work of dynamic mesh applications, there are two indications such as careful consideration of geometry model and combination with other types of solver (e.g., structure analysis). The geometry model selection with dynamic motion affects both the tendency of mesh deformation and flow field itself such as vacuum effect in the shock

tube simulation. In OpenFOAM, a solid body with 6-degree of freedom can be handled coupling flow field (fluid force) with dynamic mesh (boundary mesh method). However, a deformable body cannot be solved in the current platform. Thus, coupling stress analysis solver and flow solver is being discussed and developed using dynamic mesh approach as the interface between two solvers (Jasak & Tukovic, 2010). This can be a powerful tool in the needle-free injector simulation since liquid jet penetration (fracture pattern and depth into human body) can be examined quantitatively.

References

[1] Anderson JD (2003). *Modern Compressible Flow: With Historical Perspective*. 3rd ed., McGraw-Hill, New York.

[2] Arora A, Hakim I, Baxter J, Rathnasingham R, Srinivasan R, Fletcher D and Mitragotri S (2007). Needle free delivery of macromolecules across the skin by nanolitre-volume pulsed microjets. *Proc. Nat. Acad. Sci.* 104(11):4255–4260.

[3] Baker AB and Sanders JE (1999). Fluid mechanics analysis of a spring- loaded jet injector. *IEEE Trans. Biomed. Eng.* 26(2):235-242.

[4] Barton IE (1998). Comparison of SIMPLE- and PISO-type algorithms for transient flows. *Int. J. Numer. Meth. Fluids* 26:459-483.

[5] Batina JT (1991). Unsteady Euler algorithm with unstructured dynamic mesh for complex-aircraft aerodynamic analysis. *AIAA J.* 29 (3): 327-333.

[6] Bos F (2010). *Numerical Simulations of Flapping Foil and Wing Aerodynamics*. PhD thesis, Delft University of Technology, Netherlands.

[7] Boysan HF, Choudhury D and Engelman MS (2009). Commercial CFD in the service of industry: The first 25 years. E. H. Hirschel et al. (Eds.): *100 Vol. of Notes on Num. Fluid Mech.*, pp. 451–46, Springer-Verlag.

[8] Bradley IN (1962). *Shock Waves in Chemistry and Physics*. John Wiley and Sons, New York.

[9] Cebeci T, Shao JP, Kafyeke F and Laurendeau E (2005). *Computational Fluid Dynamics for Engineers: From Panel to Navier-Stokes Methods with Computer Programs.* Springer.

[10] Chen K, Zhou H, Li J and Cheng GJ (2010). A model on liquid penetration into soft material with application to needle-free jet injection. *ASME J. Biomech. Eng.* 132(10):101005.

[11] Chen K, Zhou H, Li J and Cheng GJ (2011). Stagnation pressure in liquid needle-free injection: modeling and experimental validation. *Drug Deliv. Letters* 1:97-104.

[12] Demirdzic I and Peric M (1988). Space conservation law in finite volume calculations of fluid flow. *Int. J. Num. Meth. Fluids* 8: 1037-1050.

[13] Desai SS (2003). Relative roles of computational fluid dynamics and wind tunnel testing in the development of aircraft. *Current Sci.* 84(1): 49-64.

[14] Downey MS, Cloete TJ and Yates ADB (2011). A rapid opening sleeve valve for a diaphragmless shock tube. *Shock Waves* 21(4):315-319.

[15] Elder R, Tourlidakis A and Yates M (2003). *Advances in CFD in Fluid Machinery Design*. John Wiley & Sons.

[16] Ferziger JH and Peric M (2004). *Computational Methods for Fluid Dynamics*. 3rd ed., Springer.

[17] Guang TH and Wang DT (1994). *Operation Manual of Sealing Components*. Mech. Ind. Press, Beijing, China.

[18] Hariharan MS, Janardhanraj S, Saravanan S and Jagadeesh G (2011). Diaphragmless shock wave generators for industrial applications of shock waves. *Shock Waves* 21:301–306.

[19] Hemond BD, Wendell DM, Hogan NC, Taberner AJ and Hunter IW (2006). Lorentz-force actuated autoloading needle-free injector. *Proc. 28th Annual Int. Conf. IEEE EMBS*, Aug. 30-Sept. 3, 2006, New York City, USA, 2318–2321.

[20] Hingson RA, Davis HS and Rosen M (1963). Historical development of jet injection and envisioned uses in mass immunization and mass therapy based upon 2 decades experience. *Mil. Med.* 128:516-524.

[21] Hirsch C (2007). *Numerical Computation of Internal and External Flows : Fundamentals of Computational Fluid Dynamics*. Butterworth-Heinemann, Oxford, UK.

[22] Hosseini HR, Onodera O and Takayama K (2000). Characteristics of an annular vertical diaphragmless shock tube. *Shock Waves* 10:151-158.

[23] Ikui T, Matsuo K and Yamamoto Y (1976). Study of a quick opening valve for shock tube research, Part 1 Structure and characteristics. *Trans JSME B* 42:2127-2132.

[24] Jasak H (1996). *Error Analysis and Estimation for the Finite Volume Method with Applications to Fluid Flows*. PhD thesis, Imperial College of Science, Technology and Medicine, London.

[25] Jasak H (2006). FOAM CFD. (website: http://www.foamcfd.org).

[26] Jasak H and Tukovic Z (2007). Automatic mesh motion for the unstructured finite volume method, *Trans. FAMENA*, 30(2): 1-18.

[27] Jasak H and Tukovic Z (2008). Simulation of free-rising bubble with soluble surfactant using moving mesh finite volume/area method. *6th Int. Conf. on CFD in Oil & Gas, Metallurgical and Process Ind.*. June 10-12, 2008, Trondheim, Norway.

[28] Jasak H and Tukovic Z (2010). Dynamic mesh handling in OpenFOAM applied to fluid-structure interaction simulations. V *Eur. Conf. Comput. Fluid Dyn. ECCOMAS CFD 2010*. June 14-17, 2010, Lisbon, Portugal.

[29] Johnson FT, Tinoco EN and Yu NJ (2005). Thirty years of development and application of CFD at Boeing commercial airplanes, Seattle. *Comput. Fluids* 34(10): 1115-1151.

[30] Kassiotis C (2008). Which strategy to move the mesh in the Computational Fluid Dynamic code OpenFOAM. Chalmers TH technical report for OpenFOAM, Gothenburg, Sweden.

[31] Kendall MA (2010). Needle free vaccine injection. *Handbook of Experimental Pharmacology,* Springer-Verlag Berlin Heidelberg, 194-215.

[32] Kosing OE, Barbosa FJ and Skews BW (1999) A new, friction controlled, piston actuated diaphragm-less shock tube driver. Shock Waves 9:69–72.

[33] Lai YG and Prezekwas AJ (1994). A finite-volume method for fluid flow simulations with moving boundaries. *Int. J. Comput. Fluid Dyn.* 2: 19-40.

[34] OpenCFD (2013). *OpenFOAM, The Open Source CFD Toolbox: User Guide*. OpenCFD Ltd.

[35] Mohanty C, Mannavathy CD, Srikanth D and Tabassum R (2011). Needle free drug delivery systems: A review. *Int. J. Pharmaceutical Research Development (IJPRD)* 3(7):7-15.

[36] Mitragotri S (2005). Immunization without needles. *Nature Rev. Immunology* 5:905-917.

[37] Mitragotri S (2006). Current status and future prospects of needle free liquid jet injectors. *Nature Reviews. Drug Discovery* 5:543-548.

[38] Portaro R and Ng HD (2011). Analysis and development of a quick acting diaphragm-less shock tube driver. *Bulletin of the American Physical Society* Vol. 56, Number 18.

[39] Portaro R and Ng HD (2013). Experimental analysis of the performance of an air-powered needle-free liquid jet injector. *Proc. 35th Int. Conf. IEEE Eng. Medicine & Biology Soc.,* July 3-7, 2013, Osaka, Japan.

[40] Portaro R and Ng HD (2013). Experimental analysis of the performance of an air-powered needle-free liquid jet injector. Submitted to *Journal of Medical and Biological Engineering*. 1st revision, May 30, 2013.

[41] Rathakrishnan E (2010). *Applied Gas Dynamics.* John Wiley & Sons, Ltd., Singapore.

[42] Salas MD (2006). Digital flight: the last CFD aeronautical grand challenge. *J. Sci. Comput.* 28: 479-505.

[43] Schneider U, Birnbacher R and Schober E (1994). Painfulness of needle and jet injection in childern with diabetes mellitus. *Eur. J. Pediatr.* 153:409-410.\Schramm-Baxter J and Mitragotri S (2004). Investigations of needle-free jet injections. *Proc. 26th Annual Int. Conf. IEEE EMBS,* Sept. 1-5, 2004, San Francisco, USA, 3543-3546.

[44] Schramm-Baxter J and Mitragotri S (2004). Needle-free jet injections: dependence of jet penetration and dispersion in the skin on jet power. *J. Control. Release*, 97:527-535.

[45] Schramm-Baxter J, Katrencik J and Mitragotri S (2004). Jet injection into polyacrylamide gels: investigation of jet injection mechanics. *J. Biomech.* 37:1181-1188.

[46] Schramm JR and Mitragotri S (2002). Transdermal drug delivery by jet injectors: Energetics of jet formation and penetration. *Pharm. Res.* 19:1673-1679.

[47] Shergold OA, Fleck NA and King TS (2006). The penetration of a soft solid by a liquid jet, with application to the administration of a needle-free injection. *J. Biomech.* 39:2593-2602.

[48] Sod GA (1978). A survey of several finite difference methods for systems of nonlinear hyperbolic conservation laws. *J. Comput. Phys.* 27: 1-31.

[49] Stachowiak JC, von Muhlen MG and Li TH (2007). Piezoelectric control of needle free transdermal drug delivery. *J. Control. Release* 124:88-97.

[50] Taberner A, Hogan NC and Hunter IW (2012). Needle-free jet injection using real-time controlled linear Lorentz-force actuators. *Med. Eng. Phys.* 34(9):1228-1235.

[51] Taberner AJ, Ball NB, Hogan NC and Hunter IW (2006). A portable needle-free jet injector based on a custom high power-density voice-coil actuator. *Proc. 28th Annual Int. Conf. IEEE EMBS*, Aug. 30-Sept. 3, 2006, New York City, USA, 2531-2534.

[52] Takayama K and Saito T (2004). Shock wave / Geophysical and medical applications. *Annu. Rev. Fluid Mech.* 36: 347-379.

[53] Takano Y and Akamatsu T (1984). A diaphragmless shock tube. *J Phys E: Sci Instrum* 17:644–646.

[54] Thévenin D and Janiga G (2008). *Optimization and Computational Fluid Dynamics*. Chap. 1, Springer-Verlag.

[55] Tinoco EN, Bogue DR, Kao TJ, Yu NJ, Li P and Ball DN (2005). Progress toward CFD for full flight envelope. *The Aeronautical J.* 109: 451-560.

[56] Toro EF (2009). *Riemann Solvers and Numerical Methods for Fluid Dynamics: A Practical Introduction*. 3rd ed., Springer, Berlin.

[57] Tranter RS, Brezinsky K and Fulle D (2001). Design of a high-pressure single pulse shock tube for chemical kinetic investigations. *Rev. Sci. Instr.* 72: 3046–3054.

[58] Tu J, Yeoh GH and Liu C (2008). *Computational Fluid Dynamics: A Practical Approach.* Elsevier Science.

[59] Weller HG, Tabor G, Jasak H and Fureby C (1998). A tensorial approach to computational continuum mechanics using object orientated techniques. *Comput. Phys.* 12: 620-63.

[60] Wijsmuller G and Snider Jr DE (1975). Skin testing: A comparison of the jet injector with the mantoux method. *Am Rev Respir Dis.* 112:789-798.

[61] Yang J, Onodera O and Takayama K (1994). Design and performance of quick opening shock tube using rubber membrane for weak shock wave generation. *JSME B* 60(570):473–478.

[62] Zhang H, Reggio M, Trepanier JY and Camarero R (1993). Discrete form of the GCL for moving meshes and its implementation in CFD schemes. *Comput. Fluids* 22(1): 9-23.

Appendix

One-dimensional Shock Tube Theory

The ideal 1-D shock tube problem consists of a tube of fluid that is initially at rest. A central diaphragm in the tube separates two sections of ideal gases with different pressures and densities (see Fig. A.1). The fluid to the left has a higher pressure as compared with the fluid on the right. The exact analytical solution to this problem is known, which is essentially a special case of a Riemann problem. When the diaphragm is ruptured instantaneously, a shock wave and contact discontinuity propagates into the low pressure region, whilst an expansion fan propagates into the high pressure section as shown in the Fig. A.2.

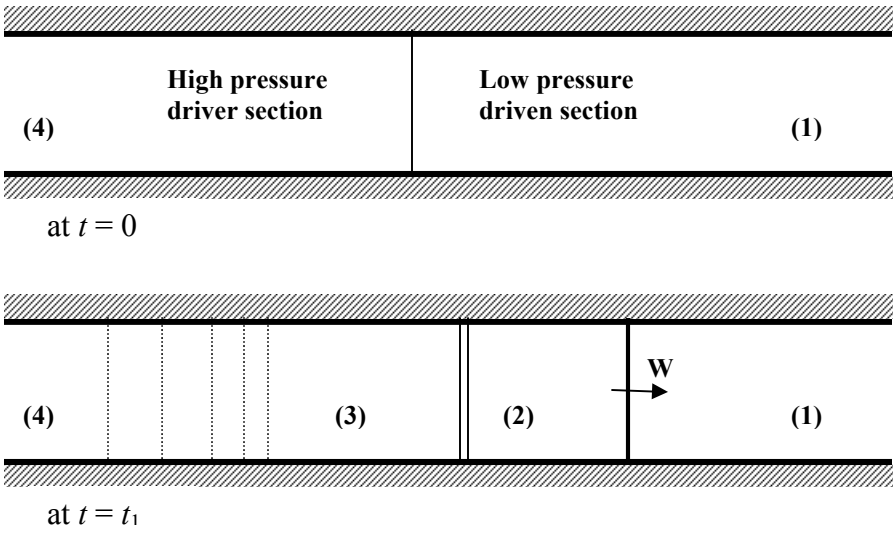

Figure A.1. Flow pattern in a 1-D shock tube

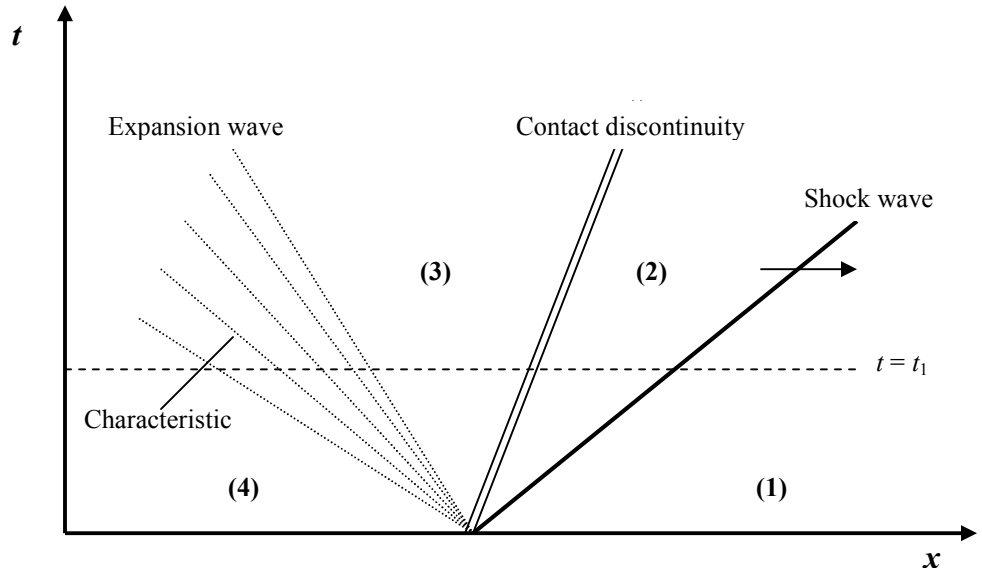

Figure A.2. *x-t* diagram showing the wave configuration of a 1-D shock tube flow

The time evolution of the fluid flow field in a 1-D shock tube is obtained by solving the Euler equations.

$$\begin{bmatrix} \rho \\ \rho u \\ e \end{bmatrix}_t + \begin{bmatrix} \rho u \\ \rho u^2 + p \\ u(e+p) \end{bmatrix}_x = 0 \qquad \text{(A.1)}$$

with

$$e = \frac{p}{\rho(\gamma - 1)} \qquad \text{(A.2)}$$

The Euler system leads to three characteristics, describing the propagation speed of the various regions of the system. Namely the rarefaction wave, the contact discontinuity and the shock discontinuity as shown in Fig. A.2. The analytical approach is basically by solving the state behind the generated normal shock and the tail of the rarefaction and match both states at the contact discontinuity.

Normal shock wave

The states after the shock are connected by the Rankine-Hugoniot (RH) normal shock jump conditions. Written with respect to the shock-fixed frame, the continuity, momentum and energy equations are given by:

$$\rho_1 W = \rho_2 \left(W - u_p\right) \tag{A.3}$$

$$p_1 + \rho_1 W^2 = p_2 + \rho_2 \left(W - u_p\right)^2 \tag{A.4}$$

$$h_1 + \frac{W^2}{2} = h_2 + \frac{\left(W - u_p\right)^2}{2} \tag{A.5}$$

Here enthalpy is defined as $h = e + pv$. The subscripts 1 and 2 refer to the gas upstream and downstream of the stationary wave, respectively. $U_p = u_1 - u_2$ thus denotes the particle velocity behind the moving shock and $u_1 = W$ and $u_2 = W$ - u_p are velocities relative to the wave. Considering a perfect gas where e = $c_v \cdot T$ and $p = \rho \cdot R \cdot T$, the above equations can be re-arranged and link the temperature and density ratios across the shock wave as functions of the pressure ratio:

$$\frac{T_2}{T_1} = \frac{p_2}{p_1}\left(\frac{\frac{\gamma+1}{\gamma-1} + \frac{p_2}{p_1}}{1 + \frac{\gamma+1}{\gamma-1}\frac{p_2}{p_1}}\right) \tag{A.6}$$

$$\frac{\rho_2}{\rho_1} = \frac{1 + \frac{\gamma+1}{\gamma-1}\frac{p_2}{p_1}}{\frac{\gamma+1}{\gamma-1} + \frac{p_2}{p_1}} \tag{A.7}$$

By defining the moving Mach number of the normal shock as:

$$M_s = \frac{W}{a_1} \tag{A.8}$$

The equations can be further combined to thus obtain the well-known Rankine–Hugoniot relations or normal shock relationship (see, for example, Hirsch, 1988):

$$\frac{p_2}{p_1} = 1 + \frac{2\gamma}{\gamma+1}\left(M_s^2 - 1\right) \tag{A.9}$$

$$\frac{T_2}{T_1} = \frac{\left[2\gamma M_s^2 - (\gamma-1)\right]\left[2 + (\gamma-1)M_s^2\right]}{(\gamma+1)^2 M_s^2} \tag{A.10}$$

$$\frac{\rho_2}{\rho_1} = \frac{(\gamma+1)M_s^2}{2 + (\gamma-1)M_s^2} \tag{A.11}$$

Alternately, Equation can be re-arranged to give:

$$W = a_1\sqrt{\frac{\gamma+1}{2\gamma}\left(\frac{p_2}{p_1} - 1\right) + 1} \tag{A.12}$$

Here the fluid velocity behind the shock wave u_p can be expressed with W, i.e.,

$$u_p = u_1 - u_2 = W\left(1 - \frac{u_2}{u_1}\right) \tag{A.13}$$

Incorporating the continuity Eq. (A.3) and Eqs. (A.12) into (A.13) yields

$$u_p = \frac{a_1}{\gamma}\left(\frac{p_2}{p_1} - 1\right)\left(\frac{\frac{2\gamma}{\gamma+1}}{\frac{p_2}{p_1} + \frac{\gamma-1}{\gamma+1}}\right)^{\frac{1}{2}} \tag{A.14}$$

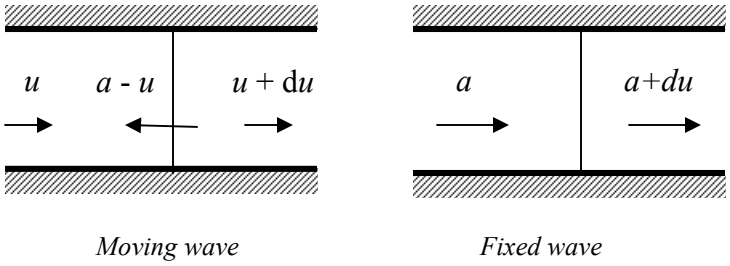

Figure A.3. Left propagating infinitesimal wave at the velocity of sound

Rarefraction wave

To determine the variation of properties across the expansion waves, consider an infinitesimal wave propagating leftward at the velocity of sound with respect to the gas moving at u, see Fig. A.3. Thus the absolute velocity of the wave relative to a fixed frame of reference is a - u. By fixing the wave, the equation of continuity for the gas is:

$$\begin{aligned} \rho a &= (\rho + d\rho)(a + du) \\ \frac{d\rho}{\rho} &= \frac{-du}{a} \end{aligned} \tag{A.14}$$

For an isentropic flow and perfect gas $p = \rho \cdot R \cdot T$, the isentropic relationship is given as:

$$\begin{aligned} pV^{\gamma} &= \text{constant} \\ p^{\frac{\gamma-1}{\gamma}} T &= \text{constant} \\ \frac{\gamma-1}{\gamma}\frac{dp}{p} &= \frac{dT}{T} \\ \frac{dp}{p} &= \frac{\gamma}{\gamma-1}\frac{dT}{T} \end{aligned} \tag{A.15}$$

Introduce the following relationship:

$$a^2 = \gamma RT \quad \text{or} \quad \frac{da}{a} = \frac{1}{2}\frac{dT}{T} \tag{A.16}$$

$$p = \rho RT \quad \text{or} \quad \frac{d\rho}{\rho} = \frac{dp}{p} - \frac{dT}{T} \tag{A.17}$$

Combining the above equation yields:

$$\frac{d\rho}{\rho} = \frac{dp}{p} - \frac{dT}{T} = \frac{\gamma}{\gamma - 1}\frac{dT}{T} - \frac{dT}{T} = \frac{2}{\gamma - 1}\frac{da}{a} \tag{A.18}$$

Therefore, one can obtain the following:

$$\begin{aligned} &\frac{2}{\gamma - 1}\frac{da}{a} = \frac{-du}{a} \\ &du + \frac{2}{\gamma - 1}da = 0 \end{aligned} \tag{A.19}$$

Finally the above equation can be integrated analytically to yield:

$$u + \frac{2}{\gamma - 1}a = \text{constant} \tag{A.20}$$

If a right-moving wave is considered instead, similar expression can be obtained, that is:

$$-u + \frac{2}{\gamma - 1}a = \text{constant} \tag{A.21}$$

These expressions are referred to as Riemann Invariant (Rathakrishnan 2010). For the flow between region (3) and (4) as described in Fig. A.2, the gas velocity $u = u_4$ is equal to zero. Thus, equation can be expressed as:

$$\frac{2}{\gamma - 1}a_4 = \frac{2}{\gamma - 1}a + \text{u} \tag{A.22}$$

and hence:

$$\frac{a}{a_4} = 1 - \frac{\gamma - 1}{2}\left(\frac{u}{a_4}\right) \tag{A.23}$$

which relates a and u within the expansion wave. With $a^2 = \gamma RT$, we can readily get:

$$\left(\frac{T}{T_4}\right) = \left(1 - \frac{\gamma - 1}{2}\left(\frac{u}{a_4}\right)\right)^2 \tag{A.24}$$

Applying the isentropic relation for region 3 and 4:

$$\left(\frac{p}{p_4}\right)=\left(\frac{T}{T_4}\right)^{\frac{\gamma}{\gamma-1}}=\left(\frac{a}{T_4}\right)^{\frac{2\gamma}{\gamma-1}} \tag{A.25}$$

to obtain:

$$\frac{p}{p_4}=\left(1-\frac{\gamma-1}{2}\left(\frac{u}{a_4}\right)\right)^{\frac{2\gamma}{\gamma-1}} \tag{A.26}$$

and

$$\frac{\rho}{\rho_4}=\left(1-\frac{\gamma-1}{2}\left(\frac{u}{a_4}\right)\right)^{\frac{2}{\gamma-1}} \tag{A.27}$$

These equations give all the properties within the simple rarefaction wave as a function of the local gas velocity u. For the simple wave, any finite information moves with local velocity $dx/dt = u - a$ along the straight characteristic. Hence, the front of the expansion wave travels with speed a_4 and the tail of the wave moves at velocity $dx/dt = u_3 - a_3$. Because the wave is centred, the characteristics are straight lines through the origin with $x = (u - a)\cdot t$. Using the Riemann invariant:

$$x=\left(u-a_4+\frac{\gamma-1}{2}u\right)t \tag{A.28}$$

or

$$u=\frac{2}{\gamma+1}\left(a_4+\frac{x}{t}\right) \tag{A.29}$$

With this, the properties within the expansion wave are determined.

Incident shock strength

Applying Eq. (A.26) to the tail of the expansion wave (interface between region (3) and (4)),

$$\frac{p_3}{p_4} = \left(1 - \frac{\gamma - 1}{2}\left(\frac{u_3}{a_4}\right)\right)^{\frac{2\gamma}{\gamma-1}} \tag{A.30}$$

Solving the above equation for u_3 yields

$$u_3 = \frac{2a_4}{\gamma - 1}\left(1 - \left(\frac{p_3}{p_4}\right)^{\frac{\gamma-1}{2\gamma}}\right) \tag{A.31}$$

Across the contact surface, the pressure and fluid velocity should be same, i.e., $p_3 = p_2$ and $u_3 = u_p$. Applying these relationships to equation (A.14) and (A.31) gives:

$$u3 = u_p = \frac{a_1}{\gamma}\left(\frac{p_2}{p_1} - 1\right)\left(\frac{\frac{2\gamma}{\gamma+1}}{\frac{p_2}{p_1} + \frac{\gamma-1}{\gamma+1}}\right)^{\frac{1}{2}} \tag{A.32}$$

$$u_3 = \frac{2a_4}{\gamma - 1}\left(1 - \left(\frac{p_2}{p_4}\right)^{\frac{\gamma-1}{2\gamma}}\right) \tag{A.33}$$

Hence, combining both to yield:

$$\frac{p_4}{p_1} = \frac{p_2}{p_1}\left(1 - \frac{(\gamma - 1)\left(\frac{a_1}{a_4}\right)\left(\frac{p_2}{p_1} - 1\right)}{\sqrt{2\gamma\left\{2\gamma + (\gamma + 1)\left(\frac{p_2}{p_1} - 1\right)\right\}}}\right)^{-\frac{2\gamma}{\gamma-1}} \tag{A.34}$$

The above equation gives the incident shock strength p_2/p_1 as an implicit function of the diaphragm pressure ratio p_4/p_1. Thus the shock strength can be solved iteratively and the

relationship between p_2/p_1 and p_4/p_1 can be expressed on a graph. These results are used for benchmark to validate the simulation of the diaphragm-less shock tube.

Using all the derived relationship, the profile at any time t can also be obtained using the following approach:

- Calculate the incident shock strength using Eq. (A.34)
- Obtain all the state properties cross the incident normal shock
- Calculate the strength of the expansion wave:

$$\frac{p_3}{p_4} = \frac{p_3}{p_1}\frac{p_1}{p_4} = \frac{p_2}{p_1}\frac{p_1}{p_4} \tag{A.35}$$

  and all the properties behind the expansion wave:

$$\frac{p_3}{p_4} = \left(\frac{\rho_3}{\rho_4}\right)^{\gamma} = \left(\frac{T_3}{T_4}\right)^{\frac{\gamma}{\gamma-1}} \tag{A.36}$$

- Once the boundaries of the regions are determined using the knowledge about the velocities of head and tail of the expansion wave, particle velocity behind the shock wave and the normal shock speed, all the state properties at different characteristic regions of the shock tube flow including those inside the expansion wave given by Eqs (A.24 – A.27) can be computed